Search for the Production of Quark-Gluon Plasma in e^+e^- Collisions at $\sqrt{s} = 91.2$ GeV with Archived ALEPH LEP1 Data

by

Anthony Shane Nicolae Badea

Submitted to the Department of Physics
in partial fulfillment of the requirements for the degree of

Bachelor of Science in Physics

at the

MASSACHUSETTS INSTITUTE OF TECHNOLOGY

June 2019

Author . . . .
Department of Physics
May 17, 2019

Certified by. . . . .
Yen-Jie Lee
Associate Professor
Thesis Supervisor

Certified by. . . . .
Jesse Thaler
Associate Professor
Thesis Supervisor

Accepted by . . . .
Nergis Mavalvala
Associate Department Head, Department of Physics

Search for the Production of Quark-Gluon Plasma in e^+e^- Collisions at $\sqrt{s} = 91.2$ GeV with Archived ALEPH LEP1 Data

by

Anthony Shane Nicolae Badea

Abstract

Measurements of two-particle angular correlations for charged particles emitted in e^+e^- collisions at a center-of-mass energy of 91 GeV are presented. The archived data are collected with the ALEPH detector at LEP. The correlation functions are measured over a broad range of pseudorapidity and full azimuth as a function of charged particle multiplicity. No significant long-range correlation is observed in both the lab coordinate analysis and in the thrust coordinate analysis, where the later is sensitive to a medium expanding around the color string between the outgoing $q\bar{q}$ pair from the Z boson decay. The associated yield distributions in both analyses are in better agreement with predictions from the PYTHIA event generator than those from HERWIG, providing new insights into the hadronization modeling. These results serve as an important reference to the observed long-range correlation in proton-proton, proton-nucleus and nucleus-nucleus collisions.

Thesis Supervisor: Yen-Jie Lee
Title: Associate Professor

Thesis Supervisor: Jesse Thaler
Title: Associate Professor

Acknowledgments

To Mom, thank you for showing me how to never give up and instilling in me a desire to leave the world better than I found it. To Dad, thank you for showing me how to live the dream only few can imagine. To Anissa, thank you for being my sister and friend, I'm lucky to have you. To Cody, Tal, Tommy, and Michael, thank you for being there every day of this journey. To George, thank you for keeping me afloat when it felt like I was drowning and sharing every laugh, failure, and success with me. To Faisal and Joey, thank you for seeing the bright side of every challenge, laughing through every setback, and refusing to give up. To my coaches, thank you for always believing in me, even when I wasn't thankful, it is you who created in me a relentless and unwavering drive to improve. To Gian, thank you for seeing the funny side of every situation. To Jesse, thank you for inspiring me to imagine the impossible and, for whatever reason, having the belief to push me ever since the moment we met. To Austin, thank you for being my friend, I would not have made it through without you. To Chris, thank you for being my big brother, I needed you more than you will ever know and the world needs more people like you. Lastly to Yen-Jie, thank you for giving me a home when I didn't have one and a family when I needed one the most.

Contents

List of Figures

List of Tables

Chapter 1

Introduction

Heavy ion physics is primarily devoted to studying the quark-gluon plasma (QGP), which is believed to have existed microseconds after the big bang, when the universe was roughly 10 billion degrees Fahrenheit (5.5 billion degrees Celsius). A full description of the properties of the QGP would elucidate a wealth of information about the origins of the universe and the basic building blocks of nature. Without question, many exciting discoveries have already been made in heavy ion physics and many more are still to come.

Historically, QGP has been studied at the Alternating Gradient Synchrotron (AGS), Super Proton Synchrotron (SPS), Large Hadron Collider (LHC) and the Relativistic Heavy Ion Collider (RHIC) using a variety of collision systems. Currently at the LHC, proton-proton (pp), proton-lead (pPb), lead-lead (PbPb), and xenon-xenon (XeXe) collisions are studied [1]. On the other hand at RHIC, more exotic combinations of heavy particles such as deuteron-gold (dAu), helium-gold (HeAu), and gold-gold (AuAu) are studied [2]. In combination, these colliders enable physicists to compare data from numerous energies and sizes, enabling detailed studies of the properties of the QGP.

Only a few years ago, results from the LHC surprisingly showed that pp collisions exhibit similar properties as heavy ion collisions [3]. Though there is yet to be a definitive theoretical interpretation of these results, some believe that they demonstrate that QGP can be produced in small systems, and thus that "heavy ion

physics" is not unique to heavy ion collisions. Because of this, understanding better the physics of pp collisions is one of the major goals for the coming decades of high energy physics. There is one missing piece in the spectrum, however, that from the viewpoint of heavy ion physics is not obvious; there has never been a study of the smallest collision system, e^+e^-, in this context.

This is not surprising, though, because until now there was no need to study e^+e^- collisions in the context of heavy ion collisions. Traditionally, heavy ion physics is interested in studying the phase transitions of quantum chromodynamics (QCD), a theory of the Standard Model of particle physics, which was believed to only be accessible at the temperatures reached in heavy ions collisions, the QGP. The pp results, which are usually used as reference for heavy ion collisions, challenged this assumption and left many wondering what the minimum conditions to produce QGP are. To answer this question it is absolutely necessary to study e^+e^- collisions. Moreover, the results from small systems have shown that the division between elementary particle physics and heavy ion physics is less defined than it was once believed to be. The goal of this thesis is to use the study of e^+e^- in the context of heavy ion physics to help bridge the gap between these fields.

The remainder of this chapter will be focused on introducing two of the basic components of the Standard Model (SM) of particle physics [4], the electroweak theory and quantum chromodynamics. A combination of equations, figures known as Feynman diagrams, and plots are used to explain the operational characteristics of them. Discussions of the Higgs mechanism are omitted so that this chapter remains focused on the interactions most relevant to heavy ion physics and the measurement shown in this thesis. An excellent description of it can be found in [5, 6].

1.1 The Electroweak Interaction

At everyday temperatures the electromagnetic and weak forces behave distinctly and can be probed independently. At higher energy scales, however, a striking phenomenon occurs – they merge into a single force known as the electroweak interaction [7].

The electroweak interaction was proposed in 1968 by Glashow, Salam, and Weinberg as a resolution of the problems known to exist with Fermi's original weak interaction [8, 9]. They hypothesized that above a critical energy scale, roughly 246 GeV, the weak and electromagnetic interactions would become indistinguishable from each other. To enable unification, they formulated the weak interaction around force carrying gauge bosons similar to quantum electrodynamics (QED). Unlike QED, however, the weak interaction was short ranged, meaning that those force mediators needed to be massive unlike the massless photon (γ). They called these particles the W^+, W^-, and Z bosons.

Nearly fifteen years later in 1983, physicists at the Super Proton Synchroton measured the masses of the W and Z bosons and found that they agreed with the predicted masses of 80.4 GeV/c^2 and 91.2 GeV/c^2, respectively [10, 11]. Using the same data, experimentalists verified that the weak and electromagnetic coupling constants were reflective of a unified theory, thus confirming the electroweak unification. In the following decade physicists were devoted to understanding the phenomenology of this theory and its relationship to quantum chromodynamics (discussed later), culminating in the construction of the Large Electron Positron (LEP) Collider at CERN.

1.1.1 The Electromagnetic Force

The first piece of the electroweak interaction is QED, the theory that describes how electrically charged particles interact with each other. It is formulated as abelian gauge theory with the symmetry group U(1) leading to the Lagrangian

$$\mathcal{L}_{\text{QED}} = i\bar{\psi}\gamma^{\mu}\partial_{\mu}\psi - e\bar{\psi}\gamma_{\mu}(A^{\mu})\psi - m\bar{\psi}\psi - \frac{1}{4}F_{\mu\nu}F^{\mu\nu}. \tag{1.1}$$

This equation encodes the way in which bispinor fields ψ and $\bar{\psi}$ describe spin-1/2 fermions and interact with the effective electromagnetic gauge field A_{μ}. Within it, the Dirac matrices γ^{μ} describe the chirality of the spinors, the coupling constant e quantifies the interaction between the fermions and the gauge field, and the classical electromagnetic field tensor $F_{\mu\nu}$ enables the presence of an emergent massless spin-1 photon.

QED allows for three basic interactions involving electrons and photons: an electron moving from one location and time to another, a photon moving from one location and time to another, and an electron emitting or absorbing a photon at a certain location and time. Rarely, however, does one need to think of the details of $\mathcal{L}_{\text{QED}}$ to describe these actions. Instead the physics of this theory can be understood using pictorial descriptions known as Feynman diagrams [1]. The diagrams below, for example, show what happens when electrons repulse each other, known as Moller scattering. The time axis is in the vertical direction and the spacial axis is in the horizontal direction.
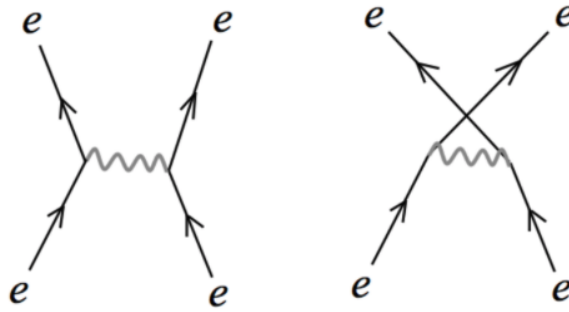
Figure 1-1: Moller Scattering

Each of the basic actions can be seen in this diagram: two electrons moving in space-time, a photon moving in space, and an electron absorbing or emitting a photon. Similar diagrams can be drawn for all types of $e^{+}e^{-}$ interactions, with QED playing

[1] An introduction to Feynman diagrams can be found here [12]

a fundamental role in each of them.

1.1.2 The Weak Interaction

The weak interaction, often called the weak nuclear force, is most commonly known as the mechanism through which radioactive decays occur. In this picture, fermions interact through the exchange of W^+, W^-, and Z bosons. Since the mediating particles each have mass much greater than those of the proton or neutron, the weak force is a short range interaction (roughly 10^{-18} meters). One commonly known weak force process is the beta decay shown below. The W bosons enable an up quark to be converted to a down quark (discussed later), and vise versa, which allows bound neutrons and protons to decay into each other.
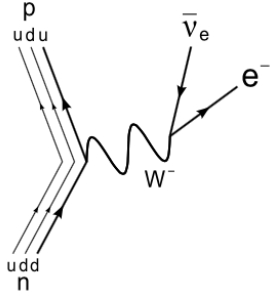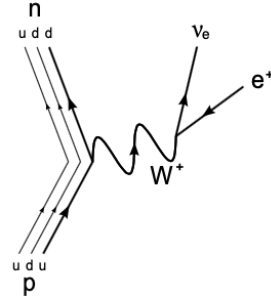
Figure 1-2: β^- decay: $n \rightarrow p + e^- + \bar{\nu}_e$.   Figure 1-3: β^+ decay: $p \rightarrow n + e^+ + \nu_e$.

The W and Z bosons also serve an important role in e^+e^- collisions, in which they can mediate their annihilation by replacing the photon. This process is similar to the original Moller Scattering process shown earlier, but is greatly enhanced at a center of mass energy energy near 91.2 GeV, corresponding to the mass of the Z boson. As will be discussed later, this makes high energy e^+e^- collisions appealing for probing physics beyond the electroweak interaction.

1.2 Quantum Chromodynamics

The strong interaction as described by quantum chromodynamics is perhaps the most fascinating and certainly the least understood of the fundamental forces included in the Standard Model. At its basic level, it describes the dynamics of the fundamental particles that make up composite hadrons such as protons and neutrons [13].

Just as in electrodynamics, QCD is build upon two basic ingredients – the quark and gluon. The quark is a spin-1/2 particle that comes in three types known as "colors", red, green, and blue, and has an electric charge of either $+\frac{2}{3}$ or $-\frac{1}{3}$. The gluon is a force carrying gauge boson with no electric charge that comes in eight color superpositions. Both particles also have an additional property known as color charge. Consequently, QCD gives rise to three basic interactions: a quark emits or absorbs a gluon, a gluon emits or absorbs a gluon, and two gluons directly interact; see Figure 1-4 below. In comparison, QED only permits that an electron can emit or absorb a photon because the photon is charge-less so it does not radiate as it moves.
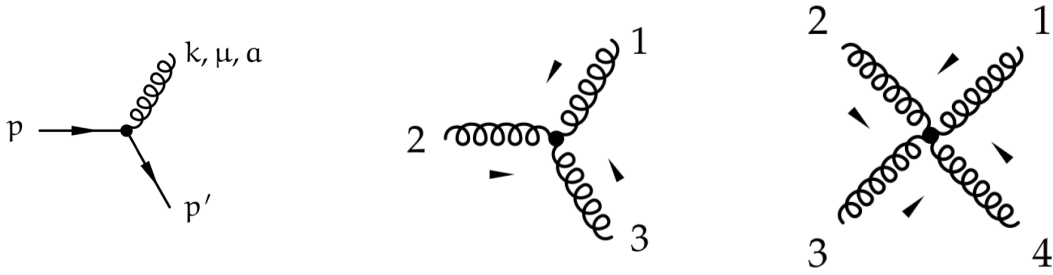
Figure 1-4: Fundamental QCD processes from left to right: a quark absorbs or emits a gluon, a gluon absorbs or emits a gluon, and gluon-gluon interaction [14].

Without going into the details, which can be found in [13], the mathematics of QCD is described by a non-abelian gauge theory with symmetry group SU(3) through the Lagrangian

$$\mathcal{L}_{\mathrm{QCD}} = \sum_q \bar{\psi}_{q,a} \left(i(\gamma^\mu \partial_\mu \delta_{ab} - \alpha_s \gamma^\mu t^C_{ab} \mathcal{A}^C_\mu - m_q \, \delta_{ab}) \, \psi_{q,b} - \frac{1}{4} F^A_{\mu\nu} F^{\mu\nu}_A. \qquad (1.2)$$

Similar to $\mathcal{L}_{\mathrm{QED}}$, this equation describes how the Dirac quark-field spinors $\psi_{q,a}$ in-

teract with the gluon gauge fields $\mathcal{A}_\mu^C$. The script q runs from one to six for the six experimentally observed generations, known as flavors. The color charge subscript a runs from one to three for the three colors. The gluon field subscript C runs from one to eight for the eight gluon colors. Within the Lagrangian, quark masses are given by m_q, the coupling between the quark and gluon fields is quantified by g_s and enabled by the SU(3) generator matrices t_{ab}^C, the gauge boson emerges from the gluonic field tensor $F_{\mu\nu}^A$, and the gamma matrices γ^μ encode the chirality of the spinors.
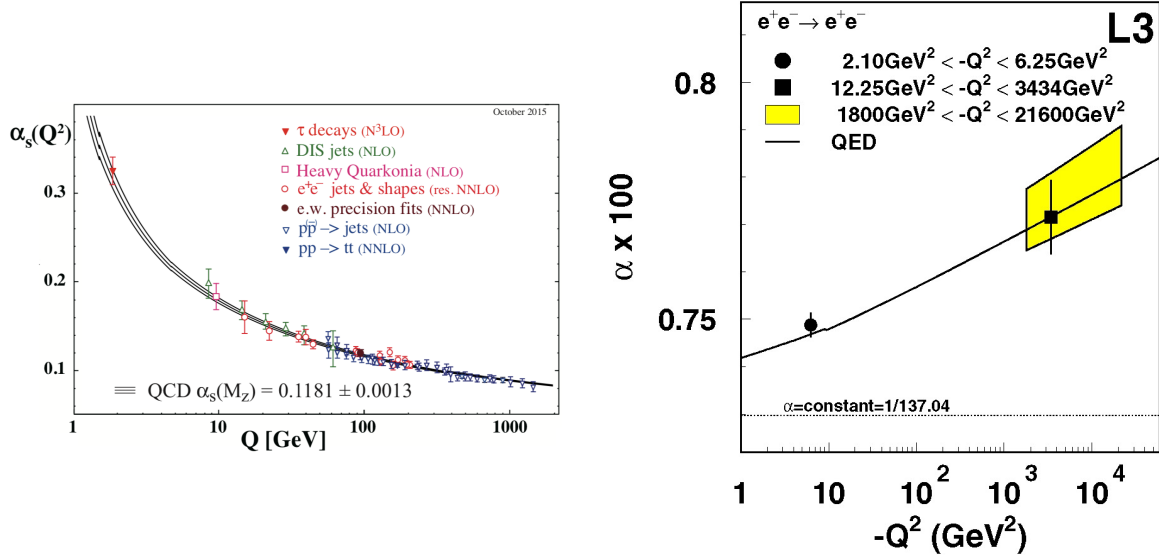
Figure 1-5: (Left) The QCD coupling constant α_S measured for a range of energies Q [15]. While the coupling constant becomes asymptotically small at high energies, at low energies it becomes large, rendering perturbative calculations at low energies impossible. (Right) Evolution of the electromagnetic coupling constant α from measurements of Bhabha scattering $e^+e^- \to e^+e^-$. In this case, the coupling becomes asymptotically large at higher energies [16].

Several key properties unique to quantum chromodynamics emerge from this equation, including asymptotic freedom which says that quarks interact more strongly the further they are apart [17]. Because of this, quarks and gluons have never been experimentally observed as free particles and their presence is only inferred by measuring the hadrons in which they are confined. Consequently, the coupling constant α_S is said to "run" which means that it becomes weaker as a function of energy, rather than stronger as is the case for the electromagnetic coupling constant; see Figure 1-5. For this reason, perturbative calculations of QCD are not possible in the low energy

regime because the coupling constant is too large.

A qualitative interpretation is often described by the Lund String model [18], in which a "color" string connects the quarks and grows in tension as the quarks move away from each other; see Figure 1-6. When the tension becomes too large, it is energetically favorable for the color field to break the string and form a new $q\bar{q}$ pair while the outgoing quarks or gluons become confined within hadrons.
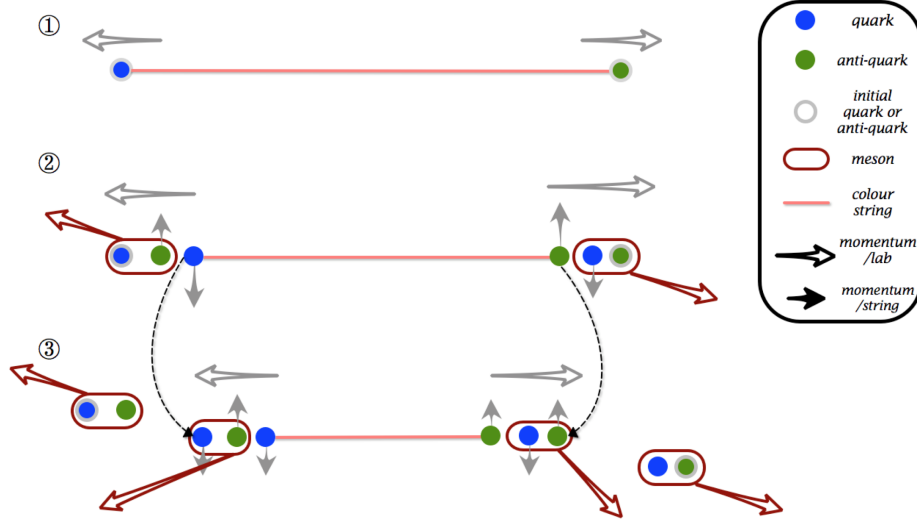
Figure 1-6: The Lund string model of hadronization [19] in which the breaking of a color string creates a new $q\bar{q}$ pair while the outgoing quarks hadronize.

As the quarks continue to move away from each other, a spray of hadrons and other particles, known as a jet, is produced via subsequent fragmentation. Jets are powerful tools when defined by clustering algorithms because they can be calculated theoretically and measured experimentally [20], unlike many other QCD physics objects. Since the lifetime of QGP is too short to inject additional probes into a collision, jets serve an important role in heavy ion physics as they are one of the only tools available to study the QGP with.

Taking a step back, QCD and lattice QCD (LQCD) are fascinating from the viewpoint of heavy ion physics because they gives rise to several unique phases of matter. The current understanding of the QCD phase diagram is shown in Figure 1-7 as a function of temperature and baryon doping, the excess of quarks over antiquarks, parameterized by the chemical potential for baryon number μ_B [21]. It shows that
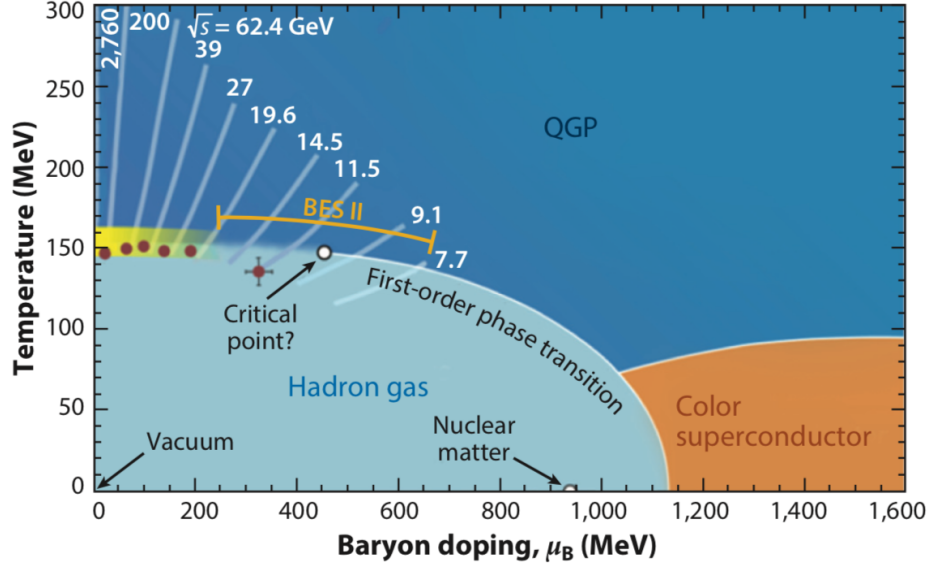
Figure 1-7: A sketch of the current understanding of the QCD phase diagram as a function of temperature and baryon doping, the excess of quarks over antiquarks, parameterized by the chemical potential for baryon number μ_B. [21]

QCD matter can transition between three distinct phases: a hadron gas (bottom left) where normal nuclear matter such as protons and pions live, a quark-gluon plasma predicted by LQCD (upper portion), and a theoretically predicted but not yet observed color superconductor phase (bottom right) [22]. Efforts of the current international heavy ion program are devoted to further mapping this diagram. Areas of primary interest at the moment are: probing the inner properties of the QGP, elucidating physics near the phase transition boundary, determining the lattice QCD equation of state, and searching for the hypothetical critical point.

1.3 Putting the Pieces Together: $e^+e^- \to Z \to q\bar{q}(g)$

The analysis presented in this thesis studies hadrons produced in electron-positron annihilations at a center of mass energy of $\sqrt{s} = 91.2$ GeV, i.e. on the Z pole. At this center of mass energy the rate of Z boson production dominates over other branching ratios; see Figure 1-8.
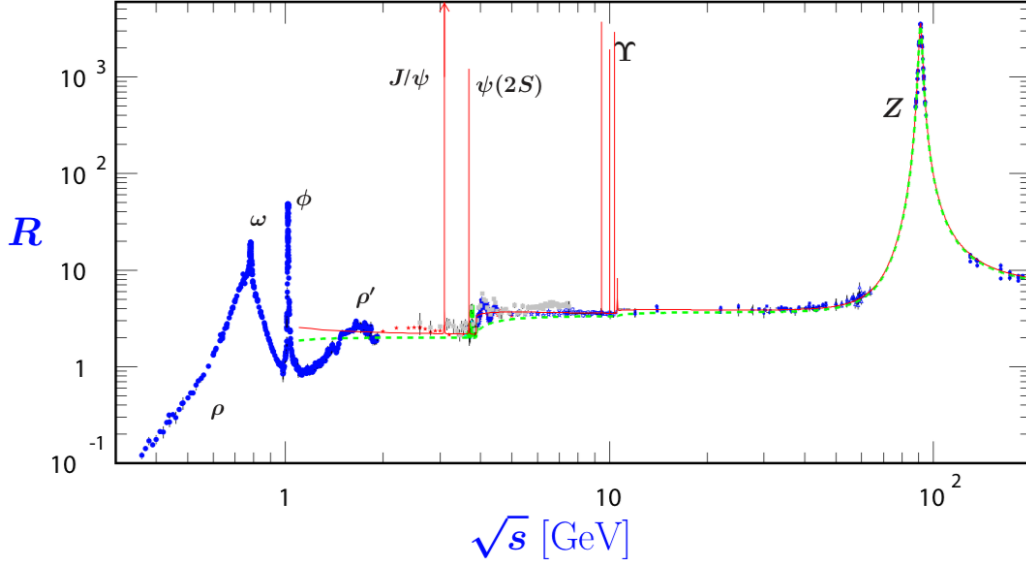
Figure 1-8: The ratio $R(s) = \sigma\left(e^+e^- \to \text{hadrons}, s\right) / \sigma\left(e^+e^- \to \mu^+\mu^-, s\right)$ from world data provided to the particle data group. The green dashed line is a naive quark parton model while the red solid line is a three loop perturbative QCD prediction. At $\sqrt{s} = 91$ GeV, the production of Z bosons is significantly enhanced [15].

This process is relevant to heavy ion physics for a number of reasons. First, it allows the study of a $q\bar{q}$ pair with fixed momenta since all of the final state energy comes from the Z boson's mass. Whereas in collisions of composite particles, one has to be concerned with the exact characteristics of the inner structure of the incoming particles, in e^+e^- the initial state is fully known. Second, at this center of mass energy there is enough hadron production through fragmentation of the outgoing quarks and gluons that high multiplicity events can be studied in analogy to pp or pPb collisions.

1.4 Particle Production Universality

In 1969, Benecke, Chou, Yang, and Yen hypothesized that the fragmentation functions of high-energy collisions would approach a limiting value, implying that particle yields would be independent of the collision energy [23]. It was only expected, however, to be seen in narrow regions of pseudorapidity specific to the fragmentation of the outgoing particles. Instead, it was found in a broad range of pseudorapidity, dependent only on the impact parameter of the collision.
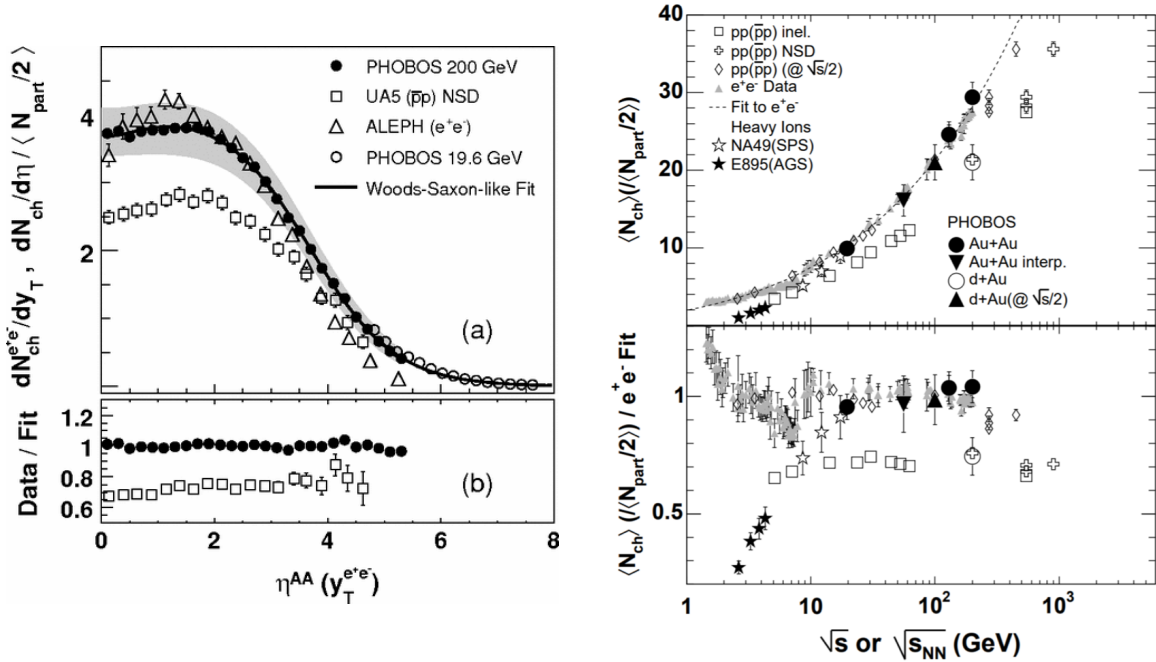
Figure 1-9: (Left) $dN_{\mathrm{ch}}/d\eta/\langle N_{\mathrm{part}}/2\rangle$ of charged particles produced in centarl Au+Au collisions at $\sqrt{s_{NN}}$ = 200 and 19.6 GeV (shifted by $\Delta\eta$ = 2.32, compared with elementary systems. The e^+e^- data are plotted as a function of y_T the rapidity relative to the thrust axis. (Right Top) Total charged multiplicity $\langle N_{ch}\rangle$ for $pp, p\bar{p}, e^+e^-$, d+Au, and central Au+Au events as a function of $\sqrt{s}$. Au+Au data are normalized by $N_{\mathrm{part}}/2$. Diamonds are the $pp/\bar{p}p$ data with $\sqrt{s_{\mathrm{eff}}} = \sqrt{s}/2$. (Right Bottom) Data in above divide by the QCD e^+e^- fit (dashed line), to allow direct comparison of different data at the same $\sqrt{s}$. Plots and captions are taken from [24].

For a still unknown reason, the corrected fragmentation functions of e^+e^-, pp, and AuAu are constrained in nearly identical ways. The e^+e^- reference axis needed to be changed so that rapidity was measured with respect to the thrust axis in order to "follow" the QCD of the system aligned with the string connecting the original $q\bar{q}$

pair. An effective pp center of mass equal to half of the actual center of mass was used to account for the momentum carried away by the incoming particle, known as the leading particle effect [25], which leaves less energy available for particle production. The AuAu fragmentation function was divided by the half of the average number of participants so that it could be compared to systems with only a single participant pair. After these corrections were applied the differential particle yields (left) and total charged multiplicity spectra (right) were nearly identical; see Figure 1-9.

The presence of extended longitudinal scaling in collisions of different particles suggests the appears of some kind of global saturation [26]. The Color Glass Condensate (CGC) mechanism [27], which has been used as a possible explanation, exhibits such a saturation but cannot be used for e^+e^- collisions. Should there be some type of universal physics governing this saturation then perhaps it is possible that heavy ion physics are also present in e^+e^- as they appear to be in pp [28].

Chapter 2

The Quark-Gluon Plasma

Early in the study of quantum chromodynamics (QCD) it was hypothesized that a state of matter made up of color charged particles (i.e., quarks and gluons) akin to the electromagnetic plasma could exist at extremely high temperatures and baryon density, in which hadrons were "melted" [29, 30, 31, 32]. This state of matter was termed the quark-gluon plasma (QGP). In the QGP, as a result of reaching the asymptotic freedom regime, the partons (generic term for quarks and gluons) were expected to roam freely, as in a partonic plasma [33]. The first measurements at RHIC, however, showed this to be incorrect [34, 35, 36]. Instead of a weakly interacting collection of quarks and gluons, a strongly interacting "soup" was found. In the past decades ultrarelativistic proton and nuclei beams have gradually become more widely available, enabling a study of the phenomenology of QCD and giving birth to the field of heavy ion physics. In this chapter three questions will be addressed:

1. Production (Section 2.1): How is QGP made?

2. The Toolkit (Section 2.2): What can be used to study QGP?

3. Observations (Section 2.3): What is known about QGP?

2.1 Production

The production of QGP is a multistage process that begins with accelerated beams of particles moving at roughly 99.9999991% the speed of light [37]. From the point of view of the detector, the particles are Lorentz-contracted discs. Large nuclei such as lead or gold have a diameter of around 14 femtometers and a thickness of $14/\gamma$ femtometers, with the Lorentz factor (γ) at the RHIC and LHC between 100 and 2500 [21].

Within these discs, quarks, antiquarks, and gluons live together bounded by color confinement. To complicate the picture, there is an additional degree of uncertainty in the spatial distribution of the partons, which is described by parton distribution functions (PDFs) [38]. The variations that occur in these distributions give rise to complicated longitudinal momentum distributions at the moment of the collision [39].

Upon colliding, most partons interact softly, meaning that their transverse momentum remains close to zero and are only slightly scattered. In the language of QCD, transverse color fields and charges collide to make longitudinal color fields, which fill the space between the receding discs. The produced color fields decay into $q\bar{q}$ pairs and gluons. Meanwhile, a small fraction of partons have hard interactions and leave with high transverse momentum. Those partons then produce other high energy parton pairs and electroweak bosons, which decay, radiate, and produce jets of hadrons, photons, and leptons.

Immediately after the collision, the energy density of this system is high enough to generate remarkable amounts of entropy in the form of new partons. As a result, at this point a "plasma of quarks and gluons" (with everything that plasma implies, in particular the "free" motion of partons) was expected. However, the RHIC experiment found that matter created to behave as a fluid, hence it was called "sQGP" – strongly interacting QGP; see Figure 2-1 for a depiction of the time-evolution of a QGP.

The initial fluid is only present for roughly 1 fm/c in its rest frame. During this time, it reaches a temperature of nearly 6 trillion degrees Fahrenheit (3 trillion degrees Celsius) and a density of roughly 10^{19} kg/m^3 (roughly 50 times the density of
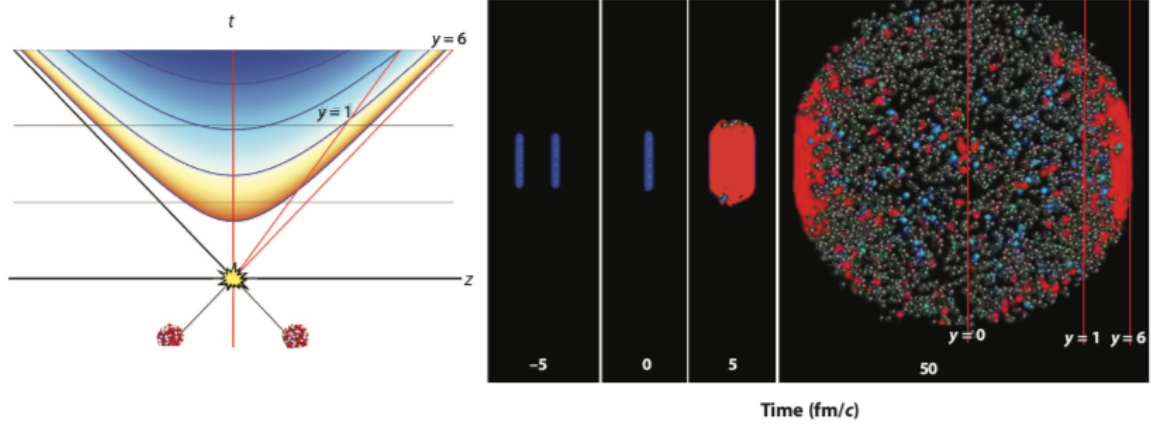
Figure 2-1: (left) Space-time picture of a heavy-ion collision. The colors indicate the temperature of the plasma with red the hottest and blue the coolest. The phases of the collision are shown as a function of the proper time (blue curves), leading to plasma forming at higher rapidities. (right) Snapshots of a central 2.76 TeV PbPb collision at different times. The panels correspond to different horizontal slices of the left-hand side image. The hottest regions are found at the highest rapidities where the beam remnants are. The red lines indicate the approximate longitudinal location of particles with rapidity $y = 0$, $y = 1$, $y = 6$ ($\sinh y = \beta\gamma$). Both images are borrowed from [21].

a nucleus). For reference, if one were to fill a standard 240mL coffee cup with QGP, it would weigh about 10^{12} (trillion) lbs. Within moments, the medium begins to expand as its anisotropic pressure gradients evolve. As a result, the liquid's transverse velocity rapidly increases. After this short time period, most of the liquid cools to low enough temperatures where hadronization can occur.

In the same time, remnants of the colliding nuclei that were not largely scattered by the collision, continue to move down the beam pipe. They are now highly excited from and compressed by the fields of energy around them. Soon after the initial collision, these remnants expand and hydrodynamize to form a QGP, which subsequently falls apart into hadrons. This physics, unfortunately, happens too close to the beam pipe (around pseudorapidity of 6.5) for the current LHC detectors to measure. Hopefully, in the future detectors will be capable of measuring the outer reaches of psuedorapidity.

2.2 The Toolkit

The QGP itself cannot be detected because it's lifetime is ultra short (roughly 10^{-22} seconds) as a result of the temperature and baryon density rapidly decreasing in the moments following the collision.. Instead, its presence is inferred through detailed analysis of the tracks and energy deposits in the calorimeter left in the detector by the remnants of the original partons (hadrons, photons, leptons, etc). Thankfully, the toolkit available to physicists is ever increasing and at present is as plentiful as ever.

The QGP probes fall into two broad categories: hard and soft. Hard probes are high mass or high p_T objects, capable of large momentum transfers, including jets, high p_T particles, quarkonium states, and electroweak gauge bosons. The properties of these probes can be calculated theoretically using perturbative QCD (pQCD). The soft scale, on the other hand, is the physics of low p_T particles. Though soft probes make up roughly 99% of the processes at the LHC, they cannot be calculated perturbatively because the coupling constant α_s is asymptotically large in this regime. Common soft probe observables include charged-particle distributions, strangeness enhancement, and particle correlations.

2.3 Observations: The Strongly Coupled Liquid

Early on, the equilibrium properties of the QGP were believed to be computable from first principles using LQCD. These calculations showed that the QGP would undergo a smooth but rapid phase transition into a hadron gas at the critical temperature of $T_c \sim 150$ MeV, corresponding to a critical energy density of $e_c \sim 0.7$ GeV/fm^3. In combination with QCD's asymptotic freedom, this lead many to believe that the QGP would be weakly interacting. Early measurements at the RHIC, however, showed this to be incorrect. Modern calculations of hot QCD matter now show that in the phase space of QGP that the pressure p, energy density ϵ, and entropy density s are roughly $15 - 20\%$ below their corresponding values for a non-interacting massless parton gas, which is consistent with estimates for a strongly coupled plasma; see Figure 2-2 for a depiction of the phase transition using LQCD calculations.
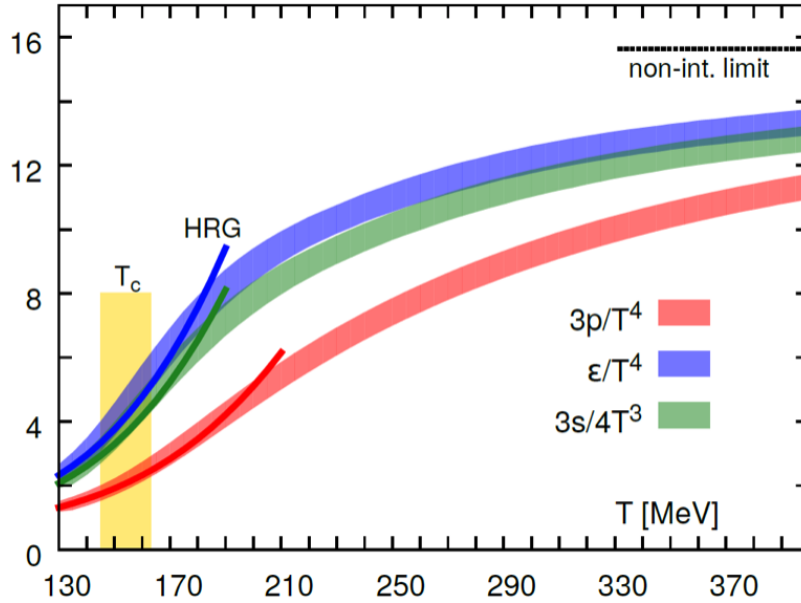
Figure 2-2: Lattice QCD of the pressure p, energy density ϵ, and entropy density s of QCD matter in equilibrium at temperature T. A continuous crossover is observed at roughly $T \sim 150$ MeV from a hadron resonance gas (colored lines) at low temperatures to a QGP at high temperatures (LQCD calculated colored bands). In the range shown, thermodynamic quantities are around 20% below their Stefan-Boltzmann values, which is consistent with estimates for a strongly coupled plasma [21].

Using experimental data to constrain the thermodynamic properties of the QGP remains an overarching goal of the field. In particular, current methods to calculate T

33

are not precise enough to comprehensively study these properties. The vast amounts of data collected in the 2018 Run 3 at the LHC, increasing luminosity in future runs, and commissioning of the sPHENIX detector will enable a new era of novel measurements, which will aid in this effort. Some of this work is already underway using the Run 3 data to re-evaluate existing measurements and develop new observables with unprecedented precision. Below are listed the QGP signatures on which the claim of a strongly interacting QGP was formed at BNL and that continue to be developed today:

1. Jet Quenching: high momentum partons moving through the dense QGP fireball lose large amounts of energy, leading to a strong suppression of the particles and jets resulting in the fragmentation of these partons. As a result, experimentalists are able to study individual fragments (charged hadrons) and in some cases reconstruct the full spray of particles from the fragmentation of one of the particles. If the energy loss is large enough, some of the jets will not make it out of the medium at all (and from here you will see an asymmetry).

2. Collective Flow: non-central collisions exhibit a spatial anisotropy, which combined with large pressure gradients cause a nonuniform 'explosion' of the QGP. Consequently, particles located in different areas of the droplet move with different speeds, which creates an additional momentum anisotropy. The particles distributions (p_T, ϕ, η) are decomposed into a Fourier series, and the harmonic coefficient v_2 (called the "flow" coefficient) along with the other coefficients are measured. Nonzero v_2 values are indicative of some kind of hydrodynamical behavior.

3. Quarkonia Production: modified quarkonia production (J/ψ and Υ) in AA collisions as compared with pp collisions, providing an analogy for Debye screening in QGP. Larger and less strongly bound excited states "melt" and progressively disappear until no bound states exist. To study this effect, the temperature dependence of the screening radius is computed using LQCD and compared with

quarkonia radii from simple models and experimental data [40, 41, 42, 43, 44, 45, 46].

4. Strangeness: an enhanced production of strange hadrons is observed in pp, pA, and AA. The enhancement is more pronounced for multi-strange baryons. The results from high-multiplicity pp collisions are in remarkable agreement with those from pA and AA collisions, indicating that enhancement is related to the final state system rather than the initial state [47, 48, 49, 50].

To understand the context for the measurement shown in Chapter 7, it is worthwhile to further discuss the physics of collective flow and jet quenching, as together they form the backbone of the picture of heavy ion physics in small systems and highlight the major questions set forward in Chapter 1.

2.3.1 Jet Quenching

Evidence that the medium is strongly interacting.

One of the byproducts of QGP production is quenching, the suppression of high p_T charged particles and jets. This effect arises because partons lose energy via emission of gluons and medium interactions, as they traverse the QGP [51, 52, 53].If, however, the QGP droplet is too small partons may not interact long enough for this effect to be noticeable.

One tool used to quantify quenching is the nuclear modification factor (R_{AA}), the ratio of the particle production in AA to geometrically-scaled pp collisions [54]. Generically for AA collisions, this ratio is less than one. This sign of suppression was observed from SPS to RHIC to LHC (Figure 2-3 (left)). Different theoretical models incorporating different energy loss mechanisms do describe the general features of the R_{AA}. In pA collisions, where no QGP is expected to be formed, the ratio is expected to be equal to one, which is what was observed most recently at the LHC in pPb collisions at 5.02 TeV (Figure 2-3 (right)).
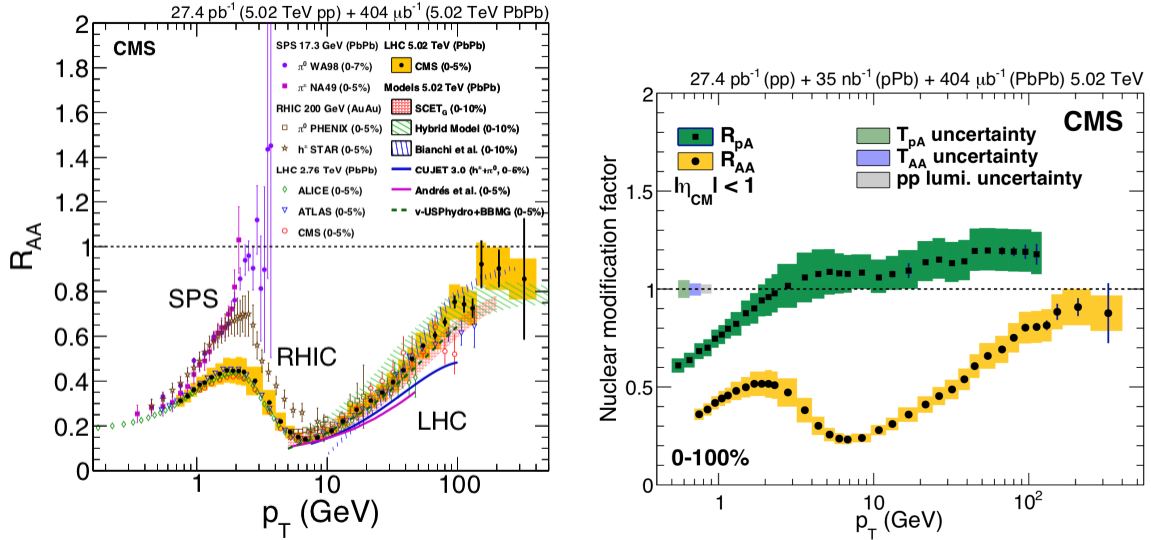
Figure 2-3: (left) Measurements of R_{AA} for PbPb (yellow) and pPb (green) collisions. The boxes show the systematic uncertainties. (right) Measurements of the R_{AA} in central heavy-ion collisions at four different center-of-mass energies (points) compared to six theoretical models (solid curves) [55].
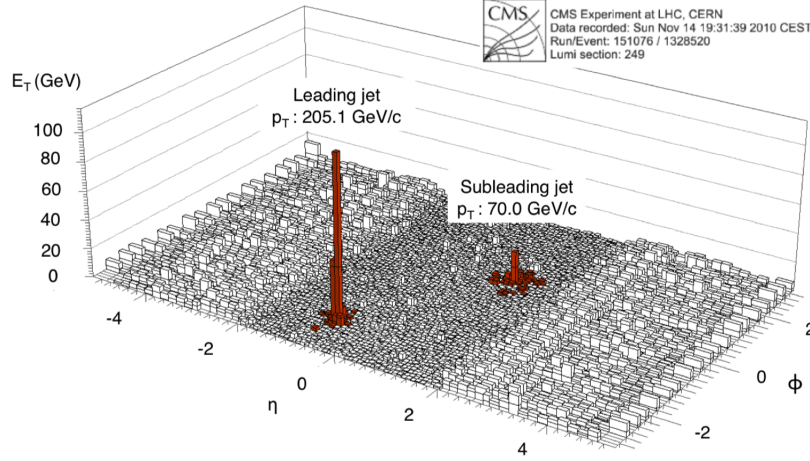
Figure 2-4: An unbalanced dijet in PbPb collisions at $\sqrt{s_{NN}} = 2.76$ TeV from the CMS experiment. The summed tranverse energy is plotted against η and ϕ with the identified jets highlighted in red and labeled with the corrected jet transverse momentum [56].

Another tool used to study quenching is dijet asymmetry [57, 58, 59]. Since high p_T particles are suppressed by the QGP, in some events the reconstructed leading and subleading jets do not have the same p_T as is expected by momentum conservation; see Figure 2-4. Following from the earlier discussion, this effect has only been observed in heavy ion collisions and not in pPb.

If QGP were a weakly interacting then particles would move through it, primarily interacting via random collisions. Models of such a system have shown that the degree of energy loss would be much less than is observed. Therefore, quenching provides direct evidence that the QGP is a strongly interacting medium.

2.3.2 Collective Flow

Proof that the medium is strongly coupled and acts as a fluid.

Multiparticle correlations have shown that particles produced in AA, pA, and pp collisions behave collectively as nearly a perfect liquid [3]. By causality, it is impossible for these correlations to have arisen in the later stages of the collision. They must, therefore, reflect dynamics of the early stages of the initial collision. Differential azimuthal correlations, in particular, have been widely used to study this effect because of their pronounced and rich structure.
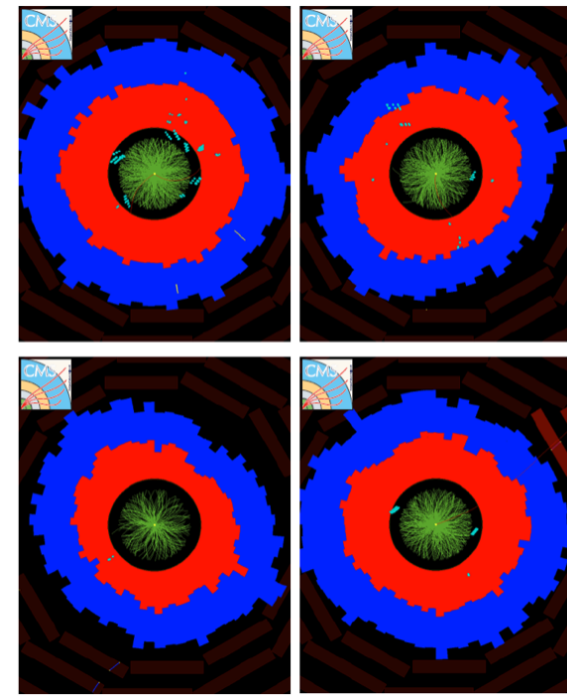
Figure 2-5: CMS event displays showing azimuthal distribution of charged tracks (green), energy deposits in the electromagnetic calorimeter (red), and energy deposits in the hadronic calorimeter (blue) for four PbPb collisions. The upper right and lower left displays showing clear ellipticity and the bottom right shows a large azimuthal anisotropy in a higher order harmonic [21].

In the initial stages of the collision, azimuthal asymmetries in the geometry of the incoming ions can cause the color fields to produce sharp pressure gradients, leading to asymmetric particle distributions that are easily visible; see Figure 2-5. As the QGP expands, these gradients become more pronounced, which causes outgoing particles to

become engrossed in its dynamics. This behavior has been modeled using relativistic hydrodynamics[1] by assuming that prior to particle production, a liquid of quarks and gluons forms, expands, and radially flows with a very low viscosity-to-entropy ratio[2] and a persistent pressure-driven anisotropy in its flow velocity. This liquid has been interpreted as the QGP.

Because of the accuracy of the hydrodynamic models used for describing the azimuthal correlations of soft particles, QGP is believed to be a strongly coupled liquid-like plasma rather than a gas-like plasma. If it were gas-like then the initial spacial anisotropies of the collision would be smeared out by the random motion of the gaseous particles. Similarly, if it had a high viscosity then the anisotropic pressure gradients would smooth out over its expansion. Instead, final state particles have substantial azimuthal anisotropies, reflective of the anisotropies in the initial geometry of the overlapping region of the colliding nuclei.

The presence of long range angular correlations also in small systems like pp and pA were not expected and are still not understood [3]. It is not clear whether the observed correlations arise because of QGP production or cold matter effects from the initial states of the protons/ions or some other effect. Moreover, it is not obvious what can be done with current data to resolve this puzzle.

---

[1]In other fields, such as condensed matter, effective field theories also describe bulk system behaviors in much the same as hydrodynamics does in heavy ion physics. The remarkable similarities between these fields should not go unnoticed.

[2]In fact its viscosity-to-entropy ratio is the lowest every observed for a liquid

2.4 The Current Picture

There are many other results, such as the sequential suppression of quarkonium states (J/ψ and Υ), that were not shown in this chapter because quenching and flow alone are sufficient to highlight the physics targeted in this thesis. Quenching points to the formation of QGP in heavy ion collisions, while flow indicates that it is produced in pp and pPb as well. These measurements do not necessarily contradict each other if the QGP droplet produced in smaller systems is too small for quenching to occur. It is not obvious, especially in the case of pp however, that this is true. Therefore, a primary goal of the field is to develop a unified picture of these effects that includes both small and large collision systems [60] by answering the following questions:

1. Is "heavy ion physics" unique to heavy ion collisions?

2. Is QGP produced in pPb and pp collisions?

3. What conditions are necessary for QGP production?

2.5 Questions To Be Answered By This Thesis

To achieve the goal of developing a unified picture of QGP in small and large systems, it is imperative to establish a small system baseline to compare measurements with. The most clear system for this role is e^+e^- because there is enough hadron production on the Z pole that high multiplicity events can be studied in analogy to pp and pA collisions (discussed in Section 1.3), there is no need to consider initial state parton/nuclear distribution functions, and limiting fragmentation may indicate the presence of a universal saturation across systems of all sizes (discussed in Section 1.4). Therefore, the goal of this thesis is to answer the following questions:

1. Is flow observed in e^+e^- collisions?

2. Should e^+e^- collisions be used as the reference for larger systems?

Chapter 3

The LEP Collider and ALEPH Detector

It was 1983 when the W and Z bosons were discovered. Though a historic achievement, researchers already had one eye on precision measurements of their masses. Years earlier in the 1970's, an idea had been conceived to construct a machine to test the laws of physics beyond anything that had been done previously. The Large Electron Positron Collider at CERN in Geneva, Switzerland would be the largest and most powerful particle accelerator ever build, with detectors positioned at four collision points named ALEPH, DELPHI, OPAL, and L3. In only five years, through the efforts of thousands of workers culminating in the largest civil engineering program in Europe at the time, the collider was fully constructed.

The event rate in Run 1 of LEP, the phase from which the data used in this thesis is from, was expected to be low, and only decrease as the energy scale increased from 91 GeV to 209 GeV into Run 2. It was also expected that particles would be distributed in jets over the entire detector volume rather than focused in just one region. For these reasons, one of the detectors needed to provide coverage for as much of the total solid angle as possible. That detector was the Apparatus for LEP Physics (ALEPH).

The ALEPH detector was designed to accomplish this goal by measuring the momentum of charged particles, the energy deposited in calorimeters from charged and

1. Silicon vertex detector
2. Drift chamber
3. Time projection chamber
4. Electromagnetic calorimeter
5. Superconducting magnet coil
6. Hadron calorimeter
7. Muon chambers
8. Luminosity monitors
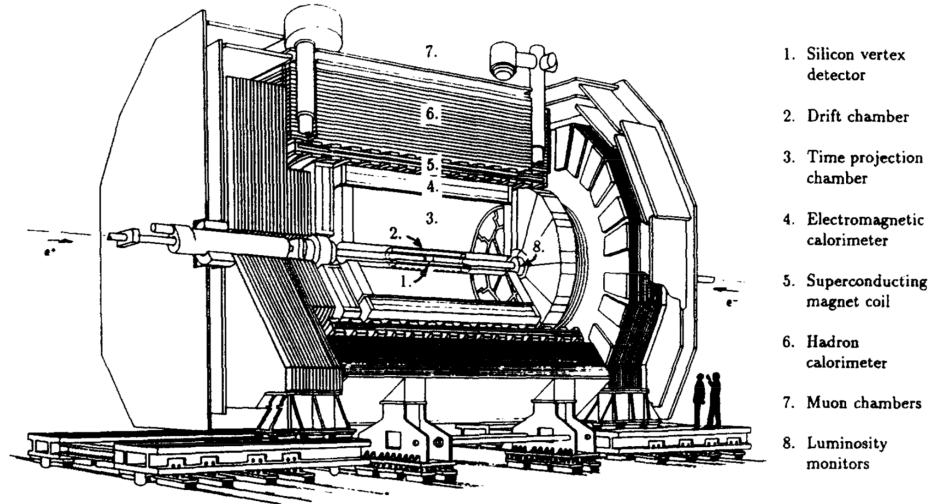
Figure 3-1: A cross sectional view of the ALEPH detector. The detector was designed to cover as much of the 4π solid angle as possible. The eight key components of the detector making up the tracking, calorimeter, and muon identification systems are listed to the right of the diagram. [61]

neutral particles, the flavour of the three leptons, and the flight distance of short lived particles. In designing the eight components shown in Figure 3-1, the ALEPH collaboration prioritized highly accurate momentum resolution, electron identification, and muon identification.

3.1 The Large Electron Positron Collider

The LEP collider was the largest circular lepton collider ever built, composed of eight straight and circular regions forming a ring that was 26.7 km (16.7 miles) in circumference and had evenly spaced contact points in four locations (see Figure 3-2).
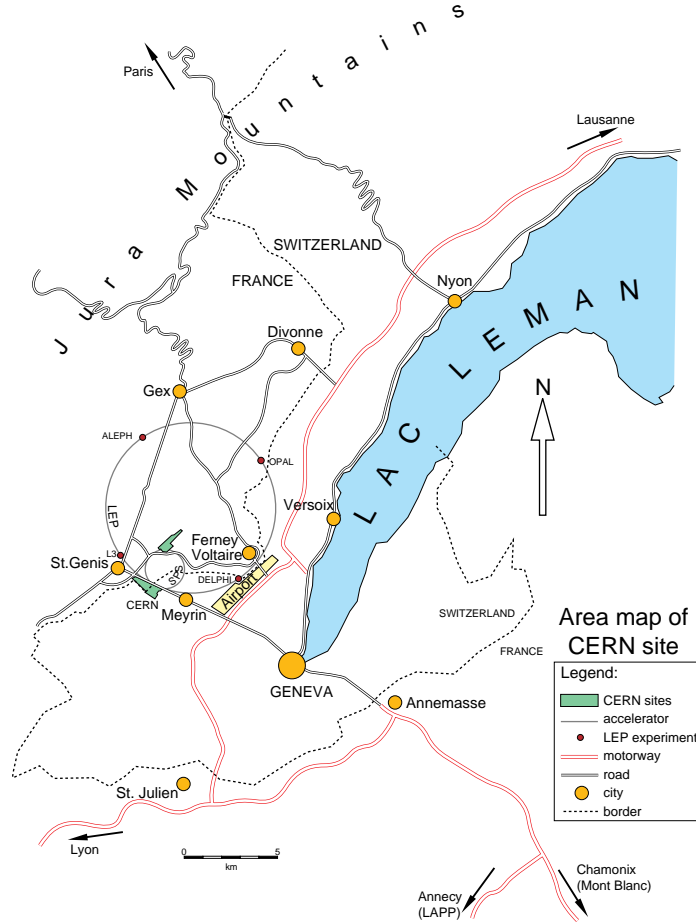
Figure 3-2: The LEP collider and its four detectors were positioned on the border of France and Switzerland. The ALEPH (upper left), L3 (bottom left), DELPHI (bottom right), and OPAL (upper right) detectors were evenly spaced along the ring of the collider. [62]

The accelerator was designed to generate beams up to energies of 209 GeV in order to create W and Z boson rich collisions. It achieved a design luminosity of 2.1×10^{31} cm^{-2} s^{-1} through the injector system shown in Figure 3-3. Electrons and positrons were produced in the LEP Injector Linacs (LIL), separately accelerated to 600 MeV, and stored in the Electron-Positron Accumulator (EPA). Prior to injection
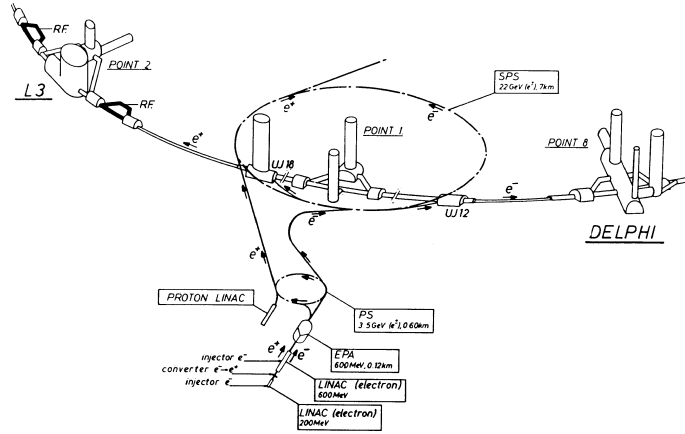
Figure 3-3: The injector system of the collider was composed of 5 main components: the LEP Injector Linacs (LIL), the Electron-Positron Accumulator (EPA), the Proton Synchrotron (PS), the Super Proton Synchrotron (SPS), and the LEP collider. The particles were produced in LIL and accelerated slightly before being stored in EPA. The PS and SPS then further accelerated the beams up to 20 GeV. Finally, LEP accelerated the beams up to the final center of mass energy and focused them into the collision regions. [62]

in LEP, the particles were accelerated up to 20 GeV using the Proton Synchrotron (PS) and the Super Proton Synchrotron (SPS). After injection, the beams were further accelerated to 45 GeV (and higher) by a radio frequency (RF) acceleration system. Simultaneously, the beams were bent into orbit by 3368 dipole magnets and focused with 808 quadrupole and 504 sextupole magnets. Lastly, near the interaction regions the beams were squeezed into a narrow RMS width of approximately (200×5) $\mu\mathrm{m}^2$. A more detailed description of LEP can be found here [63]

3.2 The ALEPH Detector

The ALEPH detector consisted of eight components: the silicon vertex detector, drift chamber, time projection chamber, electromagnetic calorimeter (ECAL), superconducting magnetic coil, hadron calorimeter (HCAL), muon chambers, and luminosity monitors; see Figure 3-4 for a detailed cross section of the detector. For the measurements performed in this thesis, the tracking system, ECAL, and HCAL were particularly import. Only these components are discussed in greater detail below, but a more detailed description of the entire ALEPH detector can be found in [61].
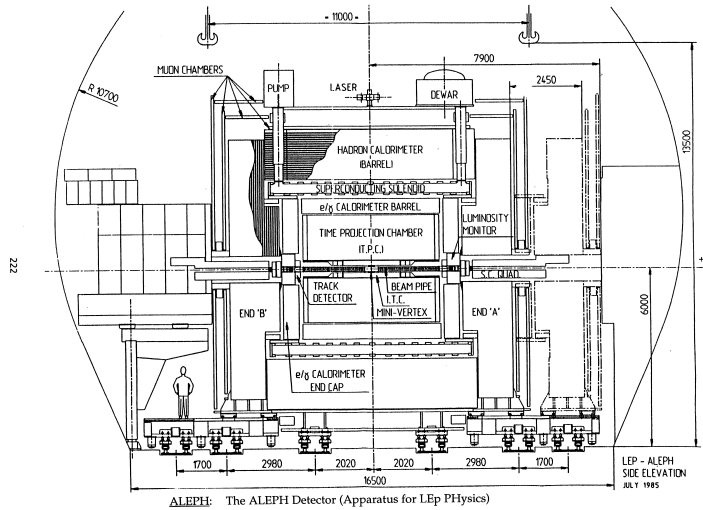
Figure 3-4: Cross section of the ALEPH detector showing the silicon vertex detector, drift chamber, time projection chamber, ECAL, superconducting magnetic coil, HCAL, muon chambers, and the luminosity monitors [61].

The trigger system used four methods to determine signals: energy deposits in the ECAL, coincidence between track segments in the drift chamber and energy deposits in the HCAL, coincidence between track segments in the drift chamber and hits in the hadron calorimeter, and two track segments back-to-back in the drift chamber. Using the total-energy and muon triggers, hadronic Z decays were collected with an efficiency of greater than 99.99% and an uncertainty of less than 0.01%. Muon events were triggered at near 100% using the muon track, electron-track, and back-to-back triggers. Tau events were triggered at near 100% as well using the same chain. Bhabha

events were triggered with 100% efficiency using the total-energy trigger alone.

3.2.1 The Tracking System

Only charged particles were included in the correlation measurement since charged tracks were reconstructed with higher precision and accuracy than neutral tracks by the tracking system. The system was composed of three components: the silicon vertex detector, drift chamber, and time projection chamber (TPC). The silicon vertex detector was located closest to the beam pipe enabling additional precision for tracks that were reconstructed in the outer tracking. Hits were established by averaging the weighted position of adjacent strips that had at least three times the mean noise charge and were associated with tracks by minimizing a track refit χ^2. The vertex detector was surrounded by a cylindrical drift chamber which measured the (r, ϕ) position of a track with a resolution of 150 μm using eight concentric layers of hexagonal drift cells. The positions of tracks along the beam were measured using the difference in arrival time of signals at either end of the wire. The time projection chamber surrounded the drift chamber and provided twenty-one three-dimensional space-point measurements.

3.2.2 The Electromagnetic Calorimeter: ECAL

The ECAL was used in this thesis to reconstruct the event thrust axis and perform event selection. The apparatus was composed of sampling layers to create photon showers and detection pieces to measure them; see Figure 3-5 for a depiction of the modules of the ECAL.

Upon entering the calorimeter, particles interacted with one of 45 lead/wire chamber sampling layers, creating an initial shower of photons which ionized a gas contained in the module[1]. The ionization was further amplified by a 25 μm gold plated tungsten wire in an extruded aluminum profile, which enabled transmission of induced signals to cathode pads. There were 74000 sets of cathode pad towers positioned to

---

[1]Lead is commonly used in ECAL's because it is the stable element with the most protons.
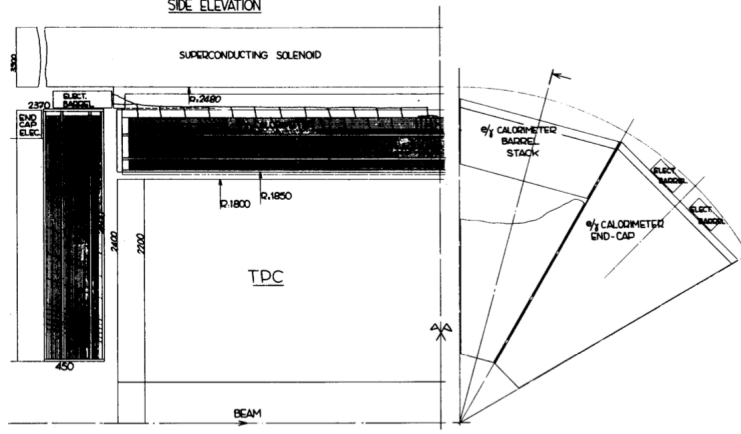
Figure 3-5: The ECAL consisted of sampling layers designed to scintillate photon shower and dedicated detection segments [64]. Its precision and accuracy enabled the event thrust axis reconstruction and selections performed in this thesis.

point towards the interaction point. The energy resolution was determined by comparing the measured energy with the beam energy or track momentum to be

$$\frac{\sigma(E)}{E} = \frac{0.18}{\sqrt{E/\mathrm{GeV}}} + 0.009. \tag{3.1}$$

More details about the ECAL can be found in the [64].

3.2.3 The Hadronic Calorimeter: HCAL

In conjunction with the ECAL, the HCAL was used in this thesis to reconstruct the event thrust axis and perform event selection. It served two purposes in the detector: to help measure hadronic energy deposits and to identify muons; see Figure 3-6 for an overview of the module.

Upon entering the HCAL, a particle entered twenty-three layers of plastic streamer tubes separated by 5 cm thick iron slabs[2] each. Hits were read out by 4788 projective towers with a typical coverage of $(3.7 \times 3.7)°$, corresponding to sixteen of the ECAL towers. Using a similar procedure as the ECAL calibration, the energy resolution of

---

[2]Iron is commonly used in HCAL's because it is a relatively cheap and moderately sized target for particles to create strong interaction showers with.

Figure 3-6: The HCAL was composed of arrays of plastic streamer tubes, iron slabs, and ECALs [65]. In this thesis, the HCAL was used to reconstruct the even thrust axis and perform event selections.

the HCAL for pions at normal incidence was determined to be

$$\frac{\sigma(E)}{E} = \frac{0.85}{\sqrt{E/\text{GeV}}}.$$

(3.2)

More details about the HCAL can be found in [65].

Chapter 4

Data Samples and Monte Carlo

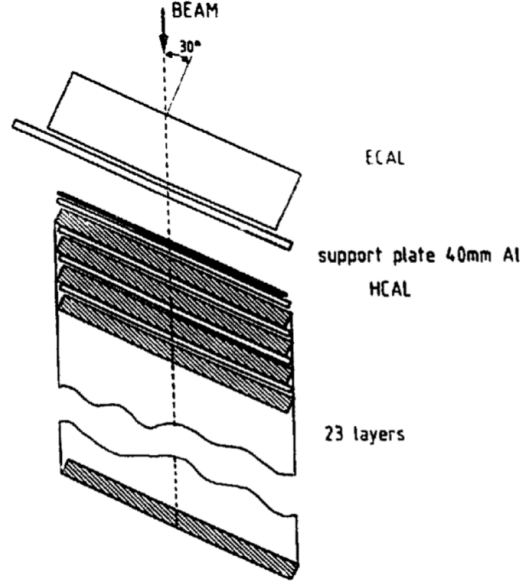Beginning as early as the 1990's, collaborations used the increasing availability of cheap and large hard drives to archive their data [66, 67, 68, 69]. In doing so, they hoped that the data could be used by future generations even when the collaboration no longer existed. Since then, however, much of this data has remained relatively untouched. Perhaps people did not want to expend the time to clean the raw samples, were not aware of analysis worth doing, or were too focused on the next experiments. In any case, this data is just waiting to be used in new ways.

Though some measurements were done using the archived ALEPH data [70, 71, 72], it too was largely used. The samples were stored in raw unprocessed text files and all code was written in Fortran, meaning that significant pre-processing was necessary to utilize modern analysis tools such as ROOT. It took roughly one year for the full data set and accompanying PYTHIA 6.1 to be processed and cleaned. At the end of this time several measurements done by the original collaboration were repeated to verify that the restoration was successful. In particular, excellent agreement was achieved in the thrust distribution (discussed in Section 5.2).

To compliment the archived data, events from (archived) reconstructed PYTHIA 6.1, (archived) generator level PYTHIA 6.1, generator level PYTHIA 8.230, and generator level HERWIG 7.1.5 were also studied. The code used for the detector interactions and the full collision reconstruction were not available, meaning that all reconstruction corrections needed to be derived from the archived PYTHIA 6.1 which had relatively

low statistics[1].

Differences between the generators arise at larger length scales where pQCD can no longer be used. Generally, both versions of PYTHIA use the Lund string model of hadronization [18] (discussed in Section 1.2), while HERWIG uses the cluster model [73, 74]. This distinction is most significant in high multiplicity collisions where the difference is magnified since the generators need to produce more particles. At short distances (below a fermi) where α_s is small, pQCD is used to compute the matrix elements necessary to model hadronization [38, 75, 76, 77, 78, 79]. More details can be found in [80, 81, 82, 73, 74].

---

[1]A lesson that can be learned from this is that all aspects necessary for published analysis should be archived and made publically available.

4.1   The Archived ALEPH Data

The pre-processing of the data from text files to the ROOT data structure, known as an ntuple, was done in two phases: conversion and cleaning. No data was thrown out in the pre-processing phase to allow for greater flexibility at analysis level. Instead, booleans corresponding to track and event selections were simultaneously computed and stored as the data was read. Additionally, a new structure termed TPCNTUPLE, built out of event, jet, and particle data sub-structures, was created to interface with the stored ROOT files at the analysis level. The TPCNTUPLE allowed a subset of data to be loaded rather the full data set, which sped up the analysis procedure and reduced the necessary RAM usage, enabling greater parallelism; see Figure 4-1 for a description of the data processing and usage pipeline.
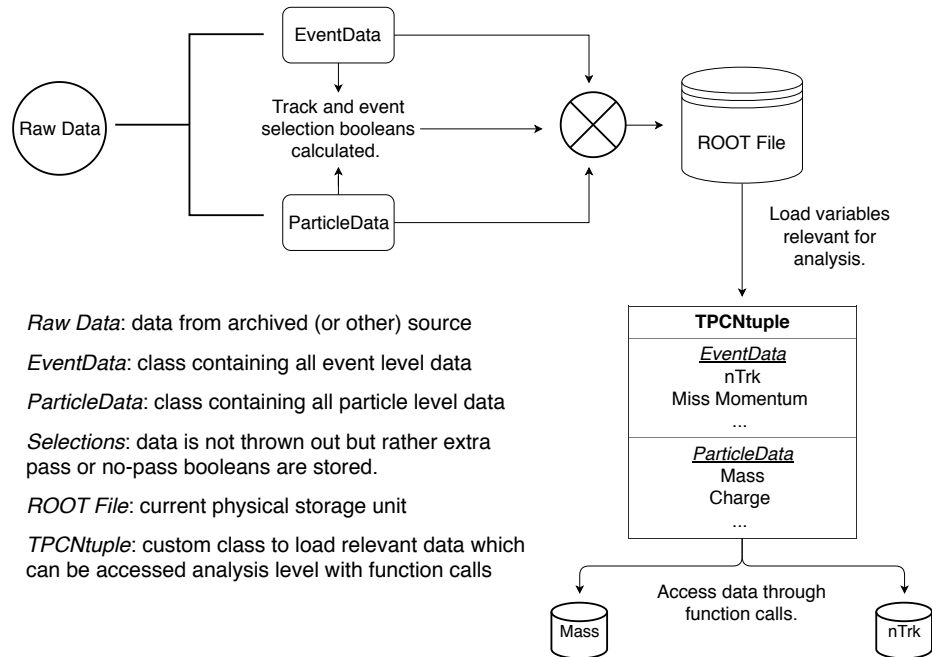
Figure 4-1: Pictorial description of the conversion pipeline and data scheme used to process the raw archived ALEPH data. Data stored in text files were fed into event and particle data sub-structures. Additional track and event selection booleans were simultaneously calculated for use at analysis level. Collectively, this data was stored in a set of ROOT files and interfaced with at the analysis level using the TPCNTUPLE class, which enabled a subset of variables to be loaded and accessed through function calls. This sped up the analysis procedure and reduced the RAM requirements, enabling greater parallelism.

4.2 The Monte Carlo Configurations

Event generators allow users to tune their parameters to study specific collision types. While the settings used for the original PYTHIA 6.1 were not provided, the tunes selected for PYTHIA 8.230 and HERWIG 7.1.5 created consistent particle spectra. The incoming electron and positron beams were set to have a center of mass equal to the mass of the Z boson (91.2 GeV/c^2). The leptonic parton densities were turned off so that the colliding leptons carried the full beam energy rather than radiating some away by photons. Weak single boson decays $f\bar{f} \to \gamma/Z$ were enabled and only hadronic decay modes $Z \to q\bar{q}$ were allowed. The only phase space cut was the requirement that $p_T > 0$ GeV/c. The exact configurations as they are written in code are given below in Table 4.1.

Monte Carlo Tunes		
Feature/Generator	PYTHIA 8.230	HERWIG 7.1.5
Beam Type	idA/B = ± 11	e- e+ -> j j
$\sqrt{s}$	eCM = m0(23)	91.2*GeV
PDF	lepton = off	
EW Production	ffbar2gmZ = on	
Decay Channels	23:onMode = off 23:onIfAny = 1 2 3 4 5	Z0->f-,f+;:OnOff Off
Phase Space Cuts	pTHatMin = 0 pTHatMax = -1	
Other		OIAS 0 OIAEW 2 SC SHatScale DSH:HSP NULL SH:HSP NULL

Table 4.1: Configurations used to produce e^+e^- collisions using PYTHIA 8.230 and HERWIG 7.1.5. In the PYTHIA column the following shortenings are used: in the decay channels row both parameters refer to particle id 23 (Z). In the HERWIG column the following are used: in the decay channels row the label f runs over [e, mu, tau, nu_e, nu_mu, nu_tau], and in the other channel OrderInAlphaS (OIAS), OrderInAlphaEW (OIAEW), ScaleChoice (SC), DipoleShowerHandler (DSH), ShowerHandler (SH), HardScaleProfile (HSP).

4.3 The Track Selections

A reconstructed charged track is accepted if it has at least four hits in the time projection chamber, is at most 2 cm from the beam line at its closest radial distance (d_0), and when at the point of closest radial approach is at most 5 cm away in the z direction (z_0). These requirements are only necessary for reconstructed Monte Carlo and data; the corresponding particle spectra are shown in the top line of Figure 4-2. Additionally, charged tracks are required to have a polar angle satisfying $|\cos\theta| \leq 0.94$ to ensure they are well contained within the detector and a transverse momentum of $p_T \geq 0.2$ GeV/c; see the bottom line of Figure 4-2 for the spectra of all data sets. A neutral track is accepted if it has energy of at least 0.4 GeV and a polar angle satisfying $|\cos\theta| \leq 0.98$. The criteria for neutral tracks are slightly different because of the mechanisms of the tracking system. Though neutral tracks are not included in the two-particle correlation function, they are used in event selections.

4.4 The Event Selections

Hadronic events are selected by requiring that the event sphericity polar angle satisfies $|\cos\theta_{\mathrm{sph}}| \leq 0.82$ as determined by energy-flow objects to ensure that events are well contained within the detector acceptance, the total charged track energy is at least 15 GeV, the total missing momentum is at most 20 GeV/c, the event has at least five accepted charged tracks, and the event has at least thirteen total accepted charged and neutral tracks; see Figure 4-3 for the relevant spectra. The the sphericity cut is only enforced for reconstructed Monte Carlo and data. Additionally, background e^+e^- production from detector material interactions in data and reconstructed PYTHIA 6 were removed. Neutral particles resulting from detector interactions could not be so easily identified, causing the distributions involving neutral particles to deviate significantly from the generator level Monte Carlo spectra. After selections are applied, the electromagnetic interactions are negligible. The selections described yielded a sample of roughly 2.4 million events.
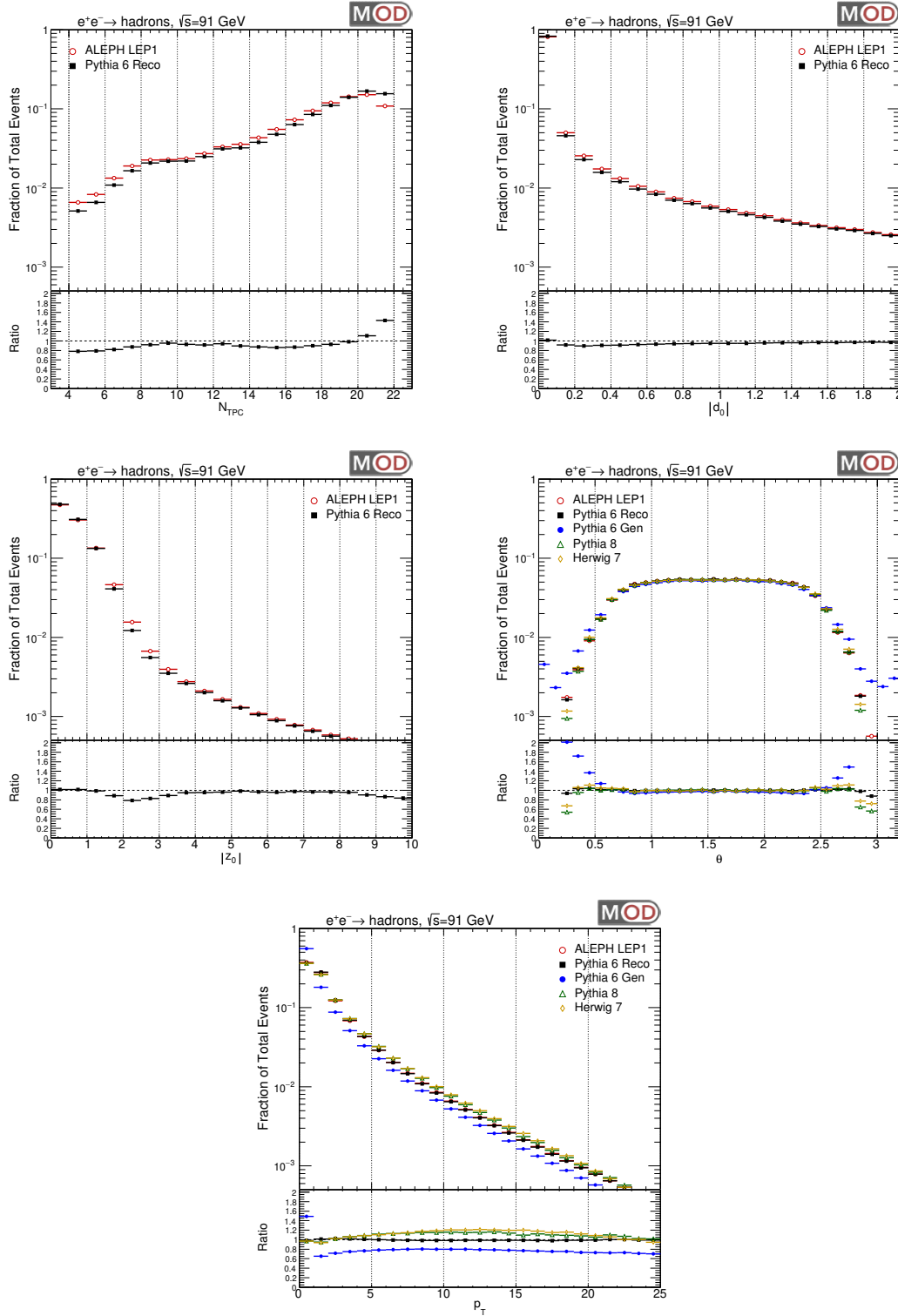
Figure 4-2: The inclusive distribution of the number of hits in the TPC (upper left), closet radial distance ($|d_0|$, upper right), and distance from the interaction point in the z direction ($|z_0|$, middle left) for archived ALEPH and reconstructed PYTHIA 6.1 data. The θ and p_T distributions are also shown for those data sets, generator level PYTHIA 6.1, PYTHIA 8.230 and HERWIG 7.1.5 data.
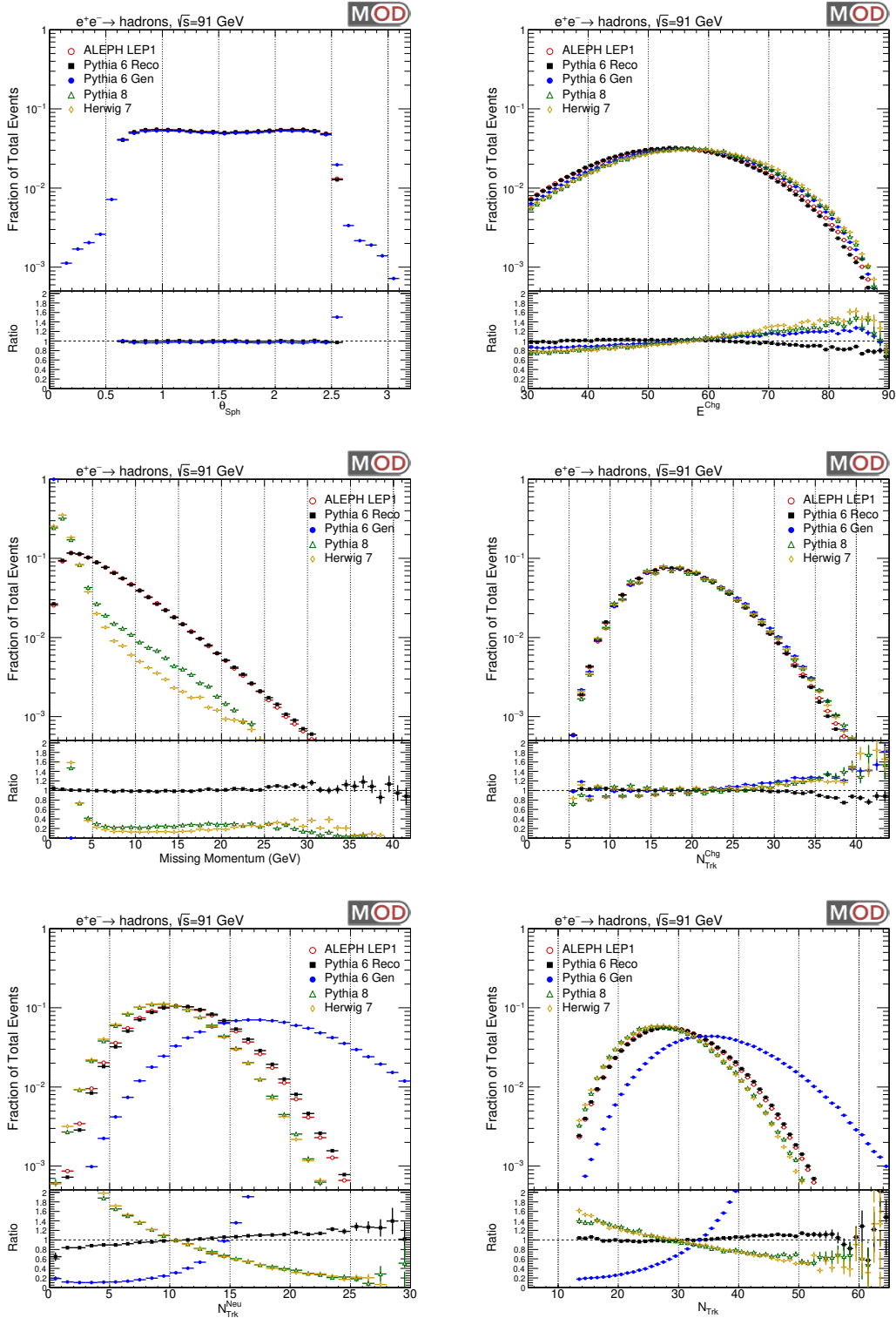
Figure 4-3: Post selection spectra specifically utilized in the selection of hadronic events from archived ALEPH data, reconstructed and generator level PYTHIA 6.1, PYTHIA 8.230, and HERWIG 7.1.5 simulations. The polar angle of the sphericity axis (top left), the total charged energy (GeV, top right), missing momentum (GeV/c, middle left), charged multiplicity (middle right), neutral multiplicity (bottom left), and inclusive multiplicity (bottom right) distributions.

Chapter 5

The Thrust Distribution

Beginning in the early 1970's, event shape measurements were used to better understand gluon bremsstrahlung, ultimately showing that scalar gluon models did not agree with experiment [83, 84, 85, 86, 87, 88]. Since then, event shape variables in e^+e^- collisions have enabled more detailed studies of QCD. Generally, event shapes provide insight into the spatial distribution of the energy-momentum flow and therefore encode how variations in fragmentation lead to final state geometric anisotropies [89, 90, 91, 92, 93, 94, 94, 95]. The thrust distribution, for example, quantifies the transition from pencil-like dijet events, with roughly columnated hadron flow, to multijet events, in which the hadron momenta are more spherically distributed. Thus, event shapes provide more information than jet clustering algorithms, which attempt to reconstruct the initial partons by algorithmically retracing the fragmentation chain [96, 97, 98, 99, 100].

Event shapes are well suited to study QCD primarily because they are collinear and infrared safe observables by construction, meaning that they can be calculated using pQCD. Many studies have been done that use these variables to extract fundamental QCD quantities, such as α_s, the quark and gluon color factors, and the QCD beta function [101, 102, 103, 104]. In addition to testing the basic properties of QCD, event shapes are also a powerful probe of the dynamics of QCD. In the vicinity of small event shape values, all commonly used measurements are primarily sensitive to gluon emission, which is relatively soft compared to the hard scale of the event

and/or is collinear to one of the hard partons. Due to the logarithmic soft-collinear dynamical enhancement of low p_T emissions and their strong coupling to the hard partons, soft emissions have significantly larger probabilities than hard emissions. In this regime, successful predictions for an event shape require either summing pQCD calculations to all orders or using a Monte Carlo event generator that contains the correct dynamics governing particle production. Therefore, comparisons between theory and data provide a benchmark for the current understanding of the dynamics of QCD.

Additionally, event shape variables contain significant non-perturbative effects in the form of varying power corrections [105, 106, 107]. These effects are handled by embedding hadronization models into Monte Carlo event generators and provide another benchmark for the current understanding of the effective theories of hadronization. Therefore, event shape variables also provide a testing ground for studying the properties of confinement.

Over the past decades many new event shape observables have been created to probe different aspects of QCD. The thrust distribution, in particular, is a powerful quantitative summary of the general final state geometry. While events with large thrust values (~ 1) contain pencil-like dijets, events with small thrust values (~ 0.5) are more isotropic sprays of particles. The ALEPH collaboration used the thrust distribution extensively to study the event shapes of collisions at LEP and compare the running of α_s to theoretical predictions. For this reason and since the thrust axis is important for the correlation analysis, the published results are compared with a new measurement to ensure that the archived data set was handled properly and to gain insight into the wide array of final state geometries accessible with e^+e^- collisions.

5.1 Analysis Method

The event thrust axis $\hat{n}$ is defined as the vector that maximizes the sum over all particles of the projected momenta onto the axis

$$T = max_{\hat{n}} \frac{\sum_i |\hat{p}_i . \hat{n}|}{\sum_i |\hat{p}_i|}, \qquad (5.1)$$

where T is the corresponding thrust value and p_i is the momentum of particle i. Experimentally, the thrust is calculated using an iterative procedure. The axis vector $\vec{n}_0$ is initially set equal to the momentum vector of any particle and then updated according to

$$\vec{n}_{i+1} = \vec{n}_i + \sum_{j=1}^{m} \text{sign}(\vec{p}_j \cdot \vec{n}_i)\vec{p}_j. \qquad (5.2)$$

The update step is repeated for N iterations or until the sign of $\vec{p}_j \cdot \vec{n}_i$ does not change for every particle between iterations (whichever comes first), and the resulting vector is stored as a thrust axis candidate. This procedure is repeated once for each possible $\vec{n}_0$, resulting in a collection of thrust axis candidates. The candidate with the largest thrust value is chosen and the corresponding thrust value is stored.

5.2 Results

The thrust spectra was measured for each of the data sets described in Chapter 4. A Bayesian unfolding procedure similar to [] was performed to remove the detector effects using the archived reconstructed and generator level PYTHIA 6. The size of the correction factor is small in the mid-T, but becomes larger in the small and large regions. Fig. 5-1 shows the corrected thrust distribution from ALEPH archived data. The results are compared to ALEPH publications [108, 109]. As shown in the figure, a very good agreement is seen between the archived data and the publications in the low T region. In the $T \sim 1$ region, a small difference at the level of 0-10% is observed between this work and the ALEPH publication in 2004 [109]. This could be due to the difference in unfolding procedure, the data set used, and/or the event selection criteria. For this reason, the figure is labeled preliminary until the discrepancy is better understood in a future analysis.
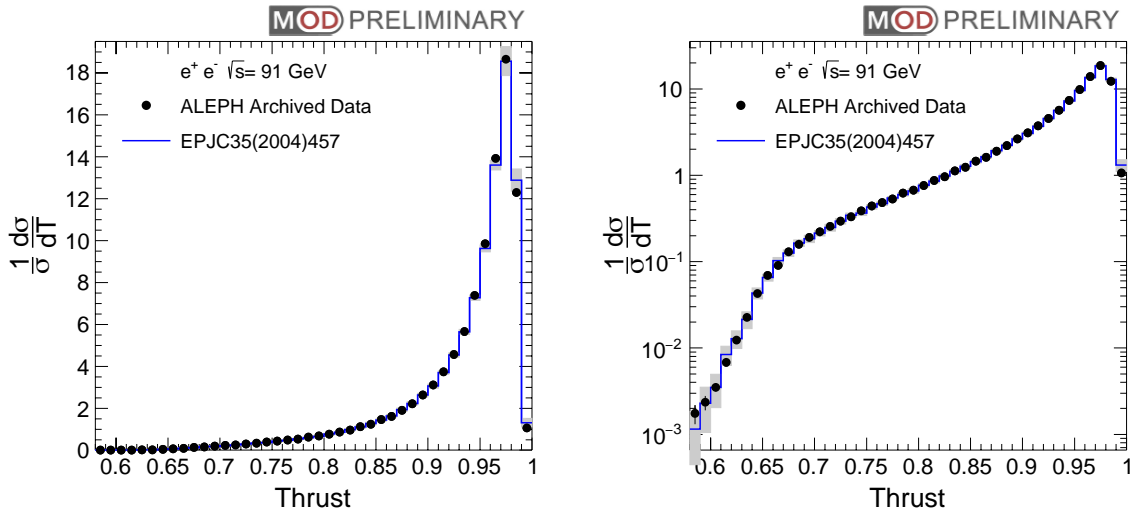
Figure 5-1: The corrected thrust distribution from ALEPH archived data compared to previous publications in linear (left) and log (right) scale.

The uncorrected distribution is also compared other event generators in Fig. 5-2; for a discussion of the different data sets see Chapter 4. Without the full unfolding, though, direct comparisons to generator level simulations is not fair. Nevertheless, the deviations from Monte Carlo are consistent with the results of the ALEPH collab-

oration [109]. The differences between the event generators are magnified in the low thrust region because the generation of spherical event shapes is highly dependent on the model of hadronization. The thrust distribution shows that widely varying event geometries can be created from $q\bar{q}$ pairs of the same energy.
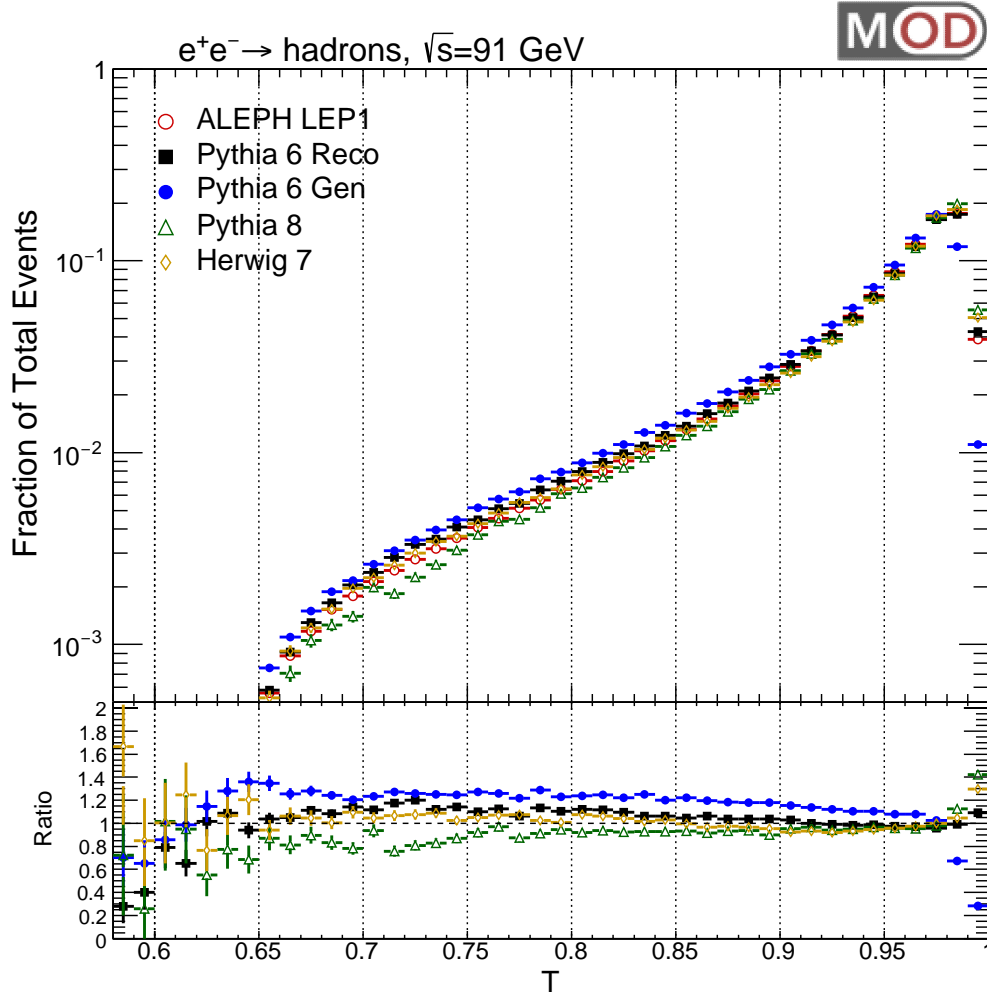

Figure 5-2: The uncorrected thrust distribution from ALEPH archived data compared to Monte Carlo event generators.
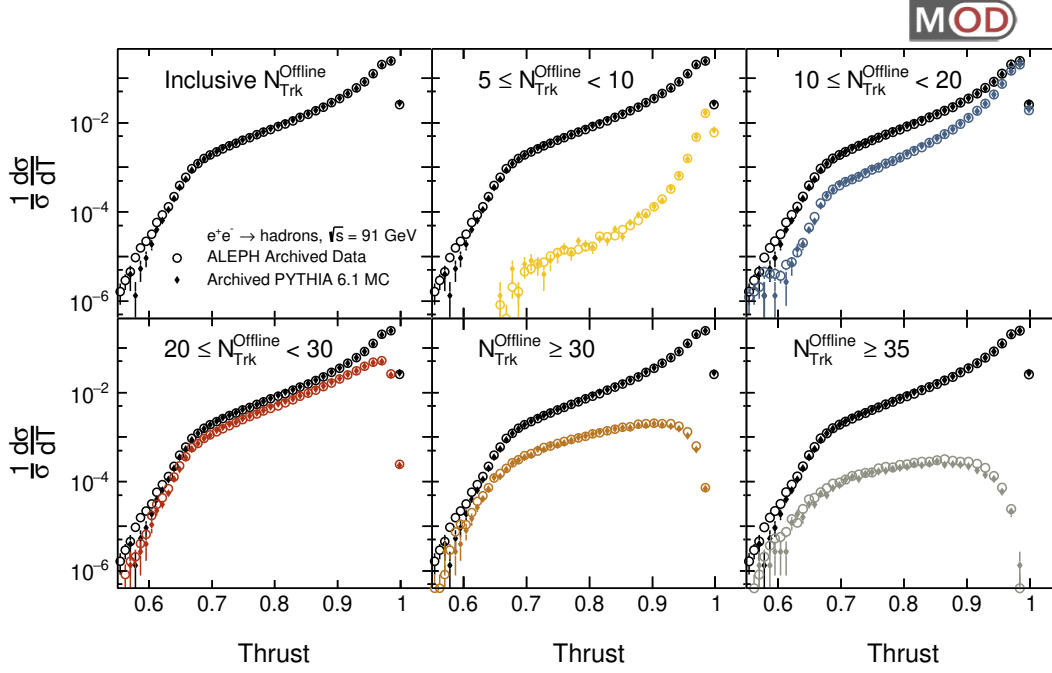
5.3 Event Shapes

Figure 5-3: The contributions to the uncorrected thrust distribution from ALEPH archived data and reconstructed PYTHIA 6.1 from the five multiplicity bins. The black points are the inclusive distribution and the colored points are the contribution from events within the specified multiplicity region.

Though the predominant geometry is a single dijet, there are many multijet events. To understand how the spectra varies by multiplicity class, the uncorrected thrust distribution is studied as a function of multiplicity. Comparisons between the contributions of the multiplicity classes to the thrust distribution for the ALEPH data and reconstructed PYTHIA 6 are shown in Fig. 5-3; for a discussion of the multiplicity classes see Section 6.4.1. The higher multiplicity events are generally more spherical and lower multiplicity events are more pencil-like. There are exceptions to this trend, however, such as the events shown in Fig. 5-4, which have a similar number of tracks (~ 40) but very different thrust values. As a result, the correlation functions within different multiplicity bins are sensitive to different regimes of fragmentation, further motivating the comparison between e^+e^- collisions and larger systems.

Figure 5-4: Event displays from the archived ALEPH data showing collisions with similar multiplicities but different geometries. (top) An event with 44 tracks and a thrust of 0.57. (bottom) An event with 39 tracks and a thrust of 0.98.
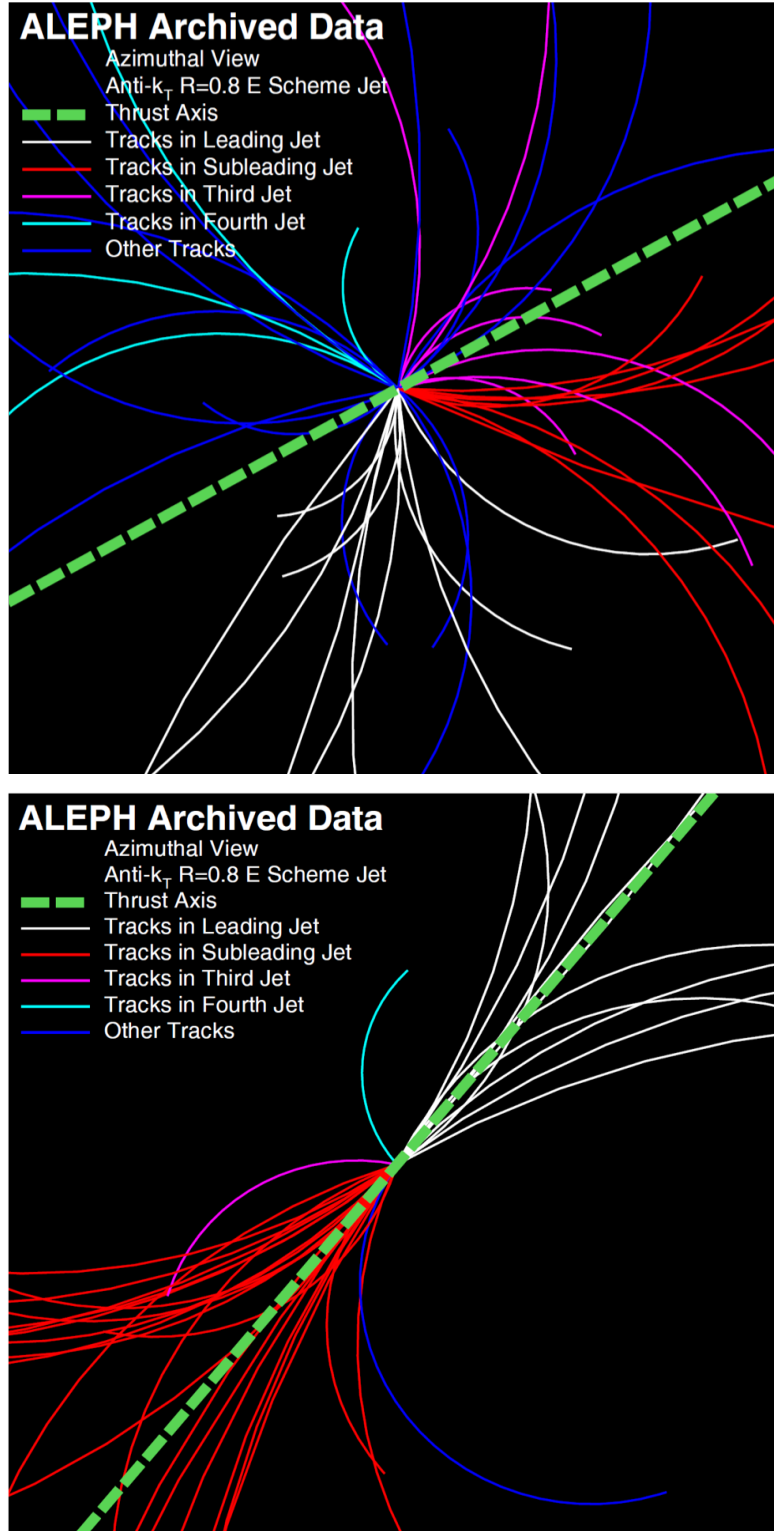
Chapter 6

Two-Particle Correlation Functions: Theory and Analysis Method

Correlation functions are used extensively in heavy-ion physics to understand bulk properties of the QGP by studying relationships between particles that are relativistically required to arise from interactions immediately following the collision. The presence of azimuthal correlations, for example, showed that final state particles had substantial azimuthal anisotropies which could have only arisen from anisotropies in the initial geometry of the QGP droplet. Though interpretations of this measurement are plentiful, the predominant consensus is that the evolution of heavy-ion collisions is governed by relativistic hydrodynamics. This picture relies, however, on there being a nonzero overlap region in which the droplet forms, which does not exist in e^+e^- collisions. Therefore, a detailed study of azimuthal correlations in e^+e^- collisions is an opportunity to test the validity of this requirement by elucidating correlations that may arise independent of the initial state geometry and parton distribution function.

6.1 The Theory of Correlation Functions

The study of two-particle correlation functions often involve experimentally construct-ing azimuthal distribution functions, denoted $f(\phi)$, event by event. Because of their periodicity, such functions can be expressed in a Fourier expansion:

$$f(\phi) = \frac{1}{2\pi} \left(x_0 + 2 \sum_{n=1}^{\infty} [x_n \cos(n\phi) + y_n \sin(n\phi)] \right). \qquad (6.1)$$

The Fourier coefficients x_n and y_n are weighted integrals of $f(\phi)$ which simplify ex-perimentally to sums over particles:

$$x_n = \int_0^{2\pi} f(\phi) \cos(n\phi) d\phi = \sum_i f_i \cos(n\phi_i), \qquad (6.2)$$

$$y_n = \int_0^{2\pi} f(\phi) \sin(n\phi) d\phi = \sum_i f_i \sin(n\phi_i), \qquad (6.3)$$

where i denotes the particle index and ϕ_i is the azimuthal angle of the i-th particle. One may parametrize the n-th Fourier coefficient with a corresponding harmonic, defined as $v_n = \sqrt{x_n^2 + y_n^2}$, and event plane angle Ψ_n.

$$x_n = v_n \cos(n\Psi_n), \qquad (6.4)$$

$$y_n = v_n \sin(n\Psi_n). \qquad (6.5)$$

Inserting this parameterization into Equation 6.1, one gets an equivalent expansion in terms of v_n and Ψ_n:

$$f(\phi) = \frac{1}{2\pi} \left(x_0 + 2 \sum_{n=1}^{\infty} \left[x_n \cos(n\phi) + y_n \sin(n\phi) \right] \right), \tag{6.6}$$

$$= \frac{1}{2\pi} \left(v_0 + 2 \sum_{n=1}^{\infty} \left[v_n \cos(n\Psi_n) \cos(n\phi) + v_n \sin(n\Psi_n) \sin(n\phi) \right] \right), \tag{6.7}$$

$$= \frac{1}{2\pi} \left(v_0 + 2 \sum_{n=1}^{\infty} v_n \cos\left[n \left(\phi - \Psi_n \right) \right] \right). \tag{6.8}$$

In the two-particle correlation analysis, the differential yield of produced particle pairs as a function of $\Delta\phi$ is constructed,

$$\frac{\mathrm{d}N}{\mathrm{d}\Delta\phi} = \frac{1}{2\pi} \left(v_0 + 2 \sum_{n=1}^{\infty} v_n \cos\left[n \left(\phi - \Psi_n \right) \right] \right), \tag{6.9}$$

where the Fourier coefficients are obtained via integration of the two dimensional $(\Delta\phi, \Delta\eta)$ differential yield,

$$v_n = \frac{\int_{\Delta\eta} \mathrm{d}\eta \frac{\mathrm{d}^2 N}{\mathrm{d}\Delta\phi \mathrm{d}\Delta\eta} v_n(\Delta\eta)}{\int_{\Delta\eta} \mathrm{d}\eta \frac{\mathrm{d}^2 N}{\mathrm{d}\Delta\phi \mathrm{d}\Delta\eta}}. \tag{6.10}$$

The coefficients, typically referred to as "integrated flow", are obtained from the two dimensional yield rather than directly from the one dimensional azimuthal yield so that they can be studied in windows of pseudorapidity[1]. The absolute normalization of the harmonics is not important so long as the detector efficiency is constant over the chosen range of psuedorapidity. If this is not true, corrections must be applied.

Physically, the harmonics provide insight into the expansive properties of the medium. A nonzero n-th harmonic arising from a resonance in the Fourier expansion is caused by an enhancement of particle pair production separated in azimuth by $2\pi/n + \Psi_n$. Such resonances indicate the presence of similar azimuthal anisotropies

---

[1] Correlations between particles widely separated in rapidity are particularly fascinating because they are relativistically required to arise from anisotropies of the early collision dynamics
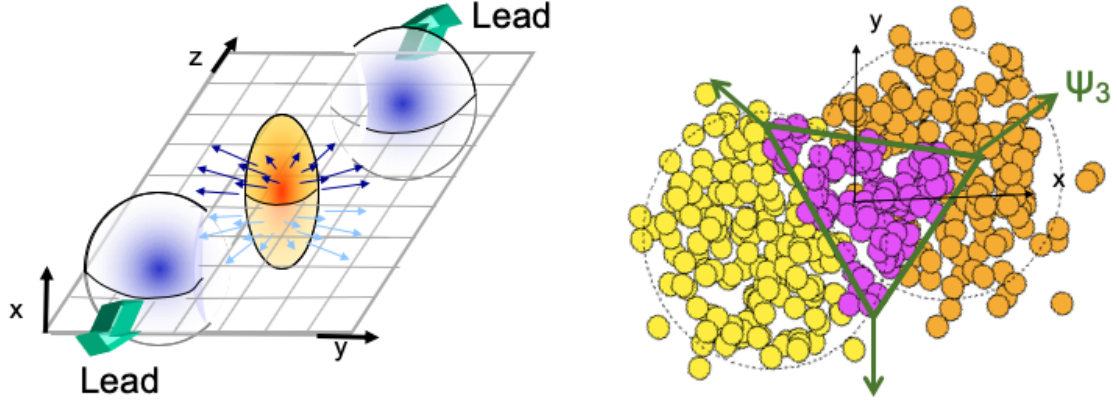
Figure 6-1: (left) Cross section of colliding lead ions at the moment of collision for an event with nonzero v_2 and event angle Ψ_2 aligned with the x-axis. Particles pairs separated in azimuth by π are enhanced because of strong transverse medium pressure gradients along the y-axis. Particles traveling in the x direction interact with the medium and thus fragment more. (right) A similar cross showing an event with a nonzero v_3 and an off axis event angle Ψ_3. An enhancement in particle pairs is seen at $2\pi/3 + \Psi_n$, indicating that the QGP droplet is triangular in shape.

in the pressure gradient of the QGP droplet, caused by variations of the collision geometry. The widely cited "elliptic" flow arising from a non-zero v_2 can be understood as a manifestation of sharp pressure gradients perpendicular to the event plane Ψ_2. Since the medium becomes elongated in the direction of lowest pressure gradients, particles moving in the direction parallel have a greater chance of medium induced fragmentation. Thus, an enhancement is seen in particles production separated by π. Without going into the details which are beyond the scope of this discussion, initial state fluctuations in larger collision systems (not e^+e^-) can give rise to nonzero triangular (v_3) and rectangular (v_4) flow coefficients [110]; see Figure 6-1 for a depiction of the QGP anisotropies that give rise to nonzero flow coefficients.

6.2 The Analysis Procedure

The analysis of two-particle correlations was performed in classes of post selection track multiplicity, $N_{trk}^{offline}$, following a procedure outlined in [111]. For each class, trigger particles are defined as charged tracks passing the selection criteria given in Section 4.3. The total number of trigger particles in an event is denoted by N_{trig}. In this analysis, particle pairs are formed by associating every trigger particle with the remaining trigger particles from a specified event. The acceptance-corrected differential yield of particle pairs is defined as

$$\frac{1}{N_{trig}}\frac{d^2N^{pair}}{d\Delta\eta d\Delta\phi} = B(0,0) \times \frac{S(\Delta\eta, \Delta\phi)B(0,0)}{B(\Delta\eta, \Delta\phi)}, \tag{6.11}$$

where $\Delta\eta$ and $\Delta\phi$ are the differences in the η and ϕ of the pair. The signal distribution, $S(\Delta\eta, \Delta\phi)$, is the yield of particle pairs from the same event,

$$S(\Delta\eta, \Delta\phi) = \frac{1}{N_{trig}}\frac{d^2N^{same}}{d\Delta\eta d\Delta\phi}. \tag{6.12}$$

The background distribution, $B(\Delta\eta, \Delta\phi)$, used to quantify combinatorial background and detector acceptance effects that could only arise by effects not related to the physics of individual collisions,

$$B(\Delta\eta, \Delta\phi) = \frac{1}{N_{trig}}\frac{d^2N^{mix}}{d\Delta\eta d\Delta\phi}, \tag{6.13}$$

is constructed by pairing the trigger particles in each event with every trigger particle in a constructed mixed event. Such events are created from five different random events satisfying the mixing criteria for Monte Carlo and twelve for data. Events are considered viable candidates for mixing if they pass the event selection criteria given in Section 4.4 and are within the same multiplicity class as the current event. The

69

quantity $B(0,0)$ represents the mixed-event associated yield for both particles of the pair going in approximately the same direction and thus having full pair acceptance. Therefore, the ratio $B(\Delta\eta, \Delta\phi)/B(0,0)$ is the normalized pair-acceptance correction factor used to derive the corrected associated yield distribution. The signal and background distributions are first computed for each event and then averaged over within a track multiplicity class.

6.2.1 Understanding the Background Function

The background distribution is described in the literature as a means to remove correlations arising from detector effects. There is not, however, a widely shown example that demonstrates how this happens.

Consider an example where data is taken from a detector with a faulty circuit that causes a ghost particle to be detected at $(\Delta\phi, \Delta\eta) = (\pi, 0.5)$ whenever a particle is detected at $(0, 1)$, and vise versa. The events are reported as lists of particles labeled $p_i = (\phi, \eta)$, where i denotes the unordered particle id. Event A has three particles $[(\pi, 0.5), (0, 1), (\pi/2, 3)]$, while event B has three particles $[(\pi, 0.5), (0, 1), (3\pi/2, 4.5)]$. The values of the signal and background distributions are shown in the tables below.

Signal

Event	$p_{i,j}$	$(\Delta\phi, \Delta\eta)$
A	$p_{1,2}$	$(\pi, -0.5)$
	$p_{1,3}$	$(\pi/2, -2.5)$
	$p_{2,3}$	$(-\pi/2, -2)$
B	$p_{1,2}$	$(\pi, -0.5)$
	$p_{1,3}$	$(-\pi/2, -4)$
	$p_{2,3}$	$(-3\pi/2, -3.5)$

Background

A/B	p_1	p_2	p_3
p_1	$(0, 0)$	$(\pi, -0.5)$	$(-\pi/2, -4)$
p_2	$(-\pi, 0.5)$	$(0, 0)$	$(-3\pi/2, -3.5)$
p_3	$(-\pi/2, 2.5)$	$(\pi/2, 2)$	$(-\pi, -1.5)$

These values are inputted into binned histograms which are shown below as a single matrix where the signal values are red (upper corner) and the background value are blue (lower corner). The values along the sides of the matrix are the lower edges of the cell, i.e. the cell labeled $\Delta\eta = -4$ contains entries with $\Delta\eta \in [-4, -3)$.

The peak at $(0, 0)$ is seen in the background but not in the signal distribution. It is only possible for particles within the same event to be located next to each

$\Delta\phi/\Delta\eta$	-4	-3	-2	-1	0	1	2	3	4
$-3\pi/2$	1	1							
$-\pi$			1		2				
$-\pi/2$	1 1		1 1				1		
0					4				
$\pi/2$		1 1					1		1
π				2 2		1			
$3\pi/2$								1	

other if that configuration is preferred by momentum conservation. This is not the case for this example, so the signal distribution has no entries here. On the other hand, it is likely that independent events will have some particles located in similar locations. That is seen in this example, causing the background distribution to be filled. Therefore, it is generally true that the background distribution will be peaked at $(0,0)$ for independent events.

The non-zero values at $(\pi, -1)$ and $(-\pi, 0)$ can be traced back to the particles $(\pi, -0.5)$ and $(0, 1)$ that were in both events A and B. When the background distribution is normalized by $B(0,0) = 4$ these cells will become $1/2$, while the cells with a single entry will become $1/4$. When the signal distribution is divided by the normalized background distribution, the cells $S(\pi, -1)$ and $S(-\pi, 0)$ are doubled, while all other cells are either quadrupled or unaffected[2].

Consequently, the signal cells with entries from the particle-ghost particle pair are suppressed relative to the other cells, thus removing the inefficiency. It should be noted that this method clearly dependents on the chosen binning of the signal and background distributions and will suppress angular separations seen in both distributions regardless of their origin.

---

[2]If $B(\Delta\phi, \Delta\eta)/B(0,0) = 0$ then no correction is applied.
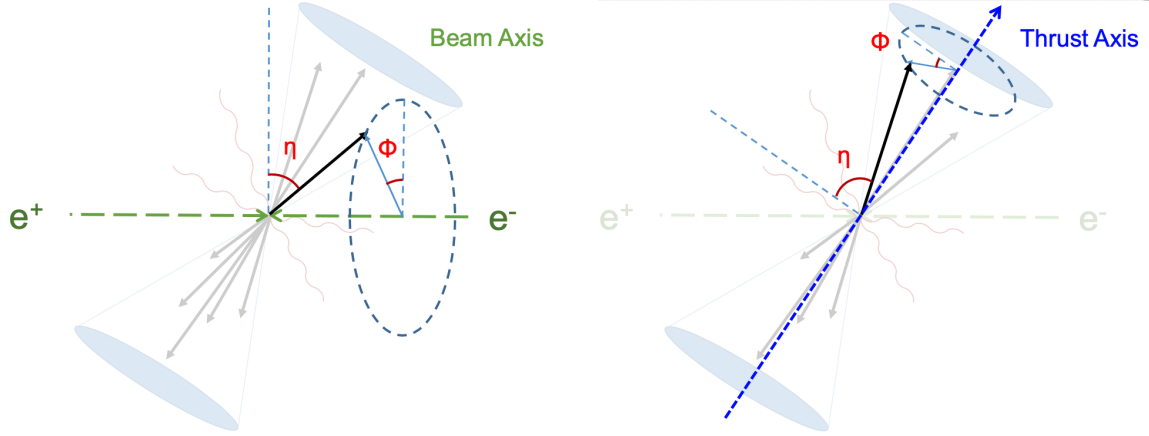
6.3   Coordinate Systems

Figure 6-2: (left) The lab coordinates used in analogy to previous analyses at hadron colliders. Track parameters are measured with respect to the "beam" axis in order to probe correlations arising from initial state (non QCD) effects. (right) Track coordinates defined with respect to the thrust axis as defined by the outgoing $q\bar{q}$ from the Z decay. Analysis in this frame enables a search for signal associated with a QCD medium expanding transverse to the color string connecting the $q\bar{q}$.

The analysis is performed with two coordinate systems: the lab frame which treats the beam pipe as the z-axis and thrust frame which uses the thrust axis instead; see Figure 6-2. The analysis is first performed with lab coordinates using the beam axis, similar to previous analyses at hadron colliders. In the hydrodynamics picture, correlation measurements in the lab frame are most sensitive to those arising from medium induced momentum modulation caused by expansion in the direction transverse to the beam pipe. In this frame any remnants of the collision that continue to travel down the beam pipe will have large psuedorapidity. Thus, by applying a cut on the polar angle of the tracks, these remnants can be removed from the correlation analysis. This is particularly important for studying pp and AA collisions because QCD processes govern dynamics at all stages of the collision, meaning that there will be unrelated correlations arising from non-flow related physics. The optimal coordinate system, therefore, is the lab frame because it removes many of these underlying correlations.

In e^+e^- collisions there are no beam remnants and QCD is only relevant in the final

72

state where particles are produced at random angles with respect to the beam pipe. Therefore, the lab frame is no longer a useful system to use to search for signatures of QCD medium production. The correlation functions in this frame are still presented to enable direct comparisons to previous measurements without re-interpretations of the analysis procedure and demonstrate the observations described.

A more opportune coordinate system is the thrust frame, defined by the outgoing $q\bar{q}$. This frame aligns the z-axis with the QCD of the event, enabling searches for signal arising from QCD induced correlations transverse to the color string. For the correlation study, all physical parameters of the tracks are recalculated in this frame but event and track selections are made in the lab frame. Maintaining this consistency in selections between the two frames ensures that the results are comparable with minimal corrections.

6.4   Corrections

6.4.1   Track-Level Efficiency Correction

To study the event multiplicity dependence of the correlation function, the analysis is performed within five multiplicity intervals classified by $N_{trk}^{offline}$. At analysis level, tracks must be re-weighted to account for detector acceptance inefficiencies which can cause tracks to be lost or gained. Without this correction the background normalization $B(0,0)$ would be computed for uncorrected particle pairs. Therefore, a multiplicity-dependent track level correction is derived from the (p_T, θ) differential yield found in the archived PYTHIA 6,

$$\epsilon\left(p_T, \theta, N_{trk}\right) = \left[\frac{d^2 N^{reco}}{dp_T d\theta} \bigg/ \frac{d^2 N^{gen}}{dp_T d\theta}\right]_{N_{trk}}. \tag{6.14}$$

Using this correction, a particle pair between p_i and p_j is weighted by $1/\epsilon_i \epsilon_j$ as it enters the correlation function. Uncorrected event multiplicities were used to classify events rather than corrected ones because of precedence established by the CMS collaboration to avoid unnecessary unfolding. Instead, a table showing the mapping from the average $\langle N_{trk} \rangle$ to corrected $\langle N_{trk}^{corr} \rangle$ multiplicities is provided in Table 6.1.

N_{trk} range	Fraction of data (%)	$\langle N_{trk} \rangle$	$\langle N_{trk}^{corr} \rangle$
$[5, 10)$	3.1	8.2	8.18
$[10, 20)$	59.4	15.2	15.24
$[20, 30)$	34.5	23.1	23.07
$[30, 999)$	3.0	32.4	32.35
$[35, 999)$	0.5	36.9	36.94

Table 6.1: N_{trk} ranges used as well as their percentage of the full sample used. Track-level corrections are derived from PYTHIA 6 to account for detector inefficiencies (Eq. 6.14). The before and after correction average multiplicities are given in the right two columns.

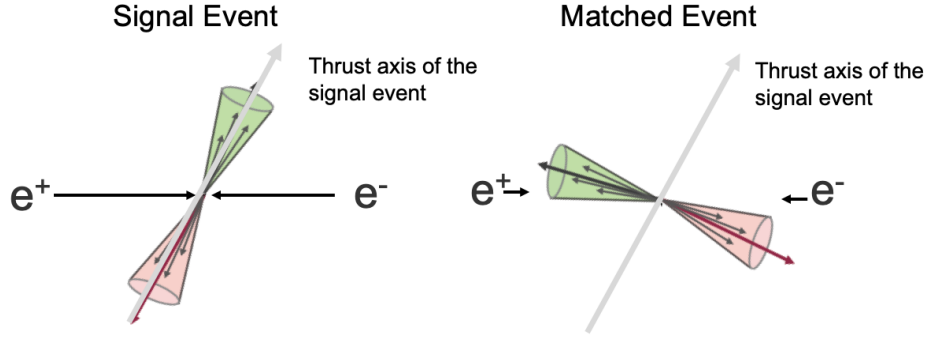## 6.4.2   Correction for Shifted Thrust Axis of Mixed Event

Figure 6-3: The (η, ϕ) distributions of the mixed events do not match with the spectra in the signal events within the multiplicity bin. A correction is applied to the mixed events by reweighting their distributions to match the average (η, ϕ) distribution in the multiplicity bin.

Mixed events are used in the background distribution to remove correlations that arise between independently created tracks. To achieve this in the thrust axis analysis, it is important that the chosen mixed event has the same thrust axis so that the derived correlations are from events in the same frame. The event-by-event variation of the thrust axis, however, causes the ALEPH detector acceptance in the thrust coordinates to vary on an event-by-event basis; see Figure 6-3. This is resolved in two steps. First the kinematics of particles in the mixed event are recalculated with respect to the thrust axis of the corresponding signal event. Then, the η and ϕ distributions of the mixed event's charged tracks are re-weighted to match that of signal events. This process is repeated for each signal-mix pair and ensures that the kinematics of particles in both events are calculated with respect to the same thrust axis while leaving the particle production uncorrelated.

6.4.3   Correction for the Residual Reconstruction Effect

An additional correction is derived from reconstructed PYTHIA 6 to account for detector induced correlations. The correlation functions for data, generator level, and reconstructed PYTHIA 6 are evaluated. The ratio of the dN/dϕ projected correlation functions for generator level over reconstructed PYTHIA 6.1 are constructed and fit

for each multiplicity bin. Three different functional forms are used to fit the ratio, with one applied to data by multiplying each bin by the fit evaluated at the bin center and half of the maximum deviation between that fit and the other two included as an uncorrelated systematic uncertainty. This uncertainty arises because only a finite sample of archived reconstructed and generator level PYTHIA 6.1 was available, meaning that any derived corrections are inherently imperfect. Therefore, the residual uncertainty is included as a systematic uncertainty rather than a statistical one.

6.5 Uncertainties

6.5.1 Systematic Uncertainties

The systematic uncertainty in the measurements of the azimuthal differential yield is evaluated following a procedure similar to previous ALEPH studies [108]. Its components are evaluated as relative uncertainties and are reported in Table 6.2 as percentages relative to the total yield. The required number of hits a track leaves in the ALEPH time projection chamber was varied from 4 to 7. From this variation, the tracking uncertainty is estimated to be 0.7% in the lab coordinate analysis and 0.3% in the thrust coordinate analysis. The hadronic event selection was studied by changing the required charged energy in an event to be 10 GeV instead of 15 GeV. The required number of charged and neutral tracks after track selections was also varied from 13 to 10. This only affects the lowest multiplicity bin, where an uncertainty of 0.6% and 3.4% is quoted for the lab and thrust coordinate analysis, respectively. A small correlated uncertainty on the value of B(0,0) arising from statistical fluctuations is also included as a component of the systematic uncertainties, but it is small compared to the other sources of uncertainty. An additional systematic is included to quantify the residual uncertainty in the reconstruction correction factor derived from the limited statistics PYTHIA 6.1 data (discussed in Section 6.4.3).

Relative Systematic Uncertainties from Selection Variations (%)

N_{Trk}	TPC Hits		Event Energy and Track Cuts		B(0,0)		Residuals	
	Beam	Thrust	Beam	Thrust	Beam	Thrust	Beam	Thrust
$[5, 10)$	0.7	0.3	0.6	3.4	0.11	0.88	10.3	0.5
$[10, 20)$	0.7	0.3	0.0	0	0.015	0.09	2.3	0.21
$[20, 30)$	0.7	0.3	0.0	0	0.013	0.05	0.2	0.06
$[30, \infty)$	0.7	0.3	0.0	0	0.027	0.06	1.2	0.21
$[35, \infty)$	0.7	0.3	0.0	0	0.057	0.13	4.4	0.21

Table 6.2: Relative systematic uncertainties based on track and event selection variations reported as percentages of the total associated yield.

6.5.2   Statistical Uncertainties

The statistical uncertainty in the results were derived using a bootstrapping procedure similar to previous studies [112]. After the associated yield from data was calculated and fit, 100K pseudo-data sets were constructed; the largest constructed set was used but increasing this number had negligible effects on the final result. Each resulting distribution was fit using the ZYAM method [113] to three functional forms and their associated yields were extracted. The three forms used included a third order polynomial, a second order polynomial plus a cosine term, and a third order Fourier series:

$$
f(\Delta\phi) = \begin{cases} \sum_{n=0}^{4} a_n \left(\Delta\phi\right)^n, \\ \sum_{n=0}^{3} a_n \left(\Delta\phi\right)^n + a_4 \cos(2\Delta\phi), \\ v_0 + 2 \sum_{n=1}^{3} v_n \cos(n\Delta\phi). \end{cases} \tag{6.15}
$$

The differences that arose from the choice of fit form are reported as a systematic error. A distribution of extracted yields for each multiplicity interval was formed and from them 95% confidence intervals were extracted; see Figures 6-4 and 6-5 for the associated yield distributions extracted from the bootstrapped pseudo-data sets in the lab and thrust frames, respectively.

A pseudo-data set was constructed bin-by-bin through a four step process. An initial estimate of the bin value was first drawn from a normal distribution centered at the fit value of the bin center with standard deviation equal to the bin error scaled by the ratio of the fit to data value. Corrections to this estimate arising from systematic errors were then computed by multiplying the relative error by the fit value of the bin center. The final bin content was set to the sum of the initial estimate plus the corrections. The bin error was set to the bin content scaled by the quadrature sum of the relative data bin error and the systematic errors.

Figure 6-4: Associated yield found with pseudo-data sets in the lab frame. Multiplicity classes are positioned along the columns and the fit functional forms, as described in Sec. 6.5.2, along the rows: (top) third order polynomial, (middle) second order polynomial plus a second degree cosine term, (bottom) third order Fourier series.
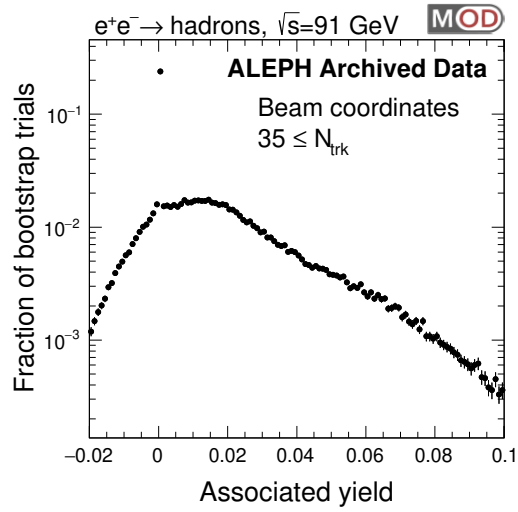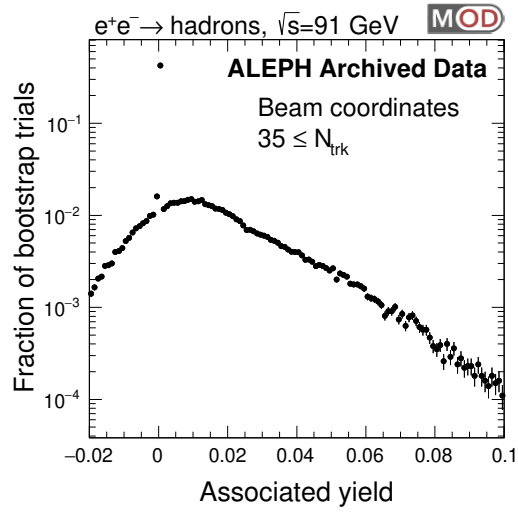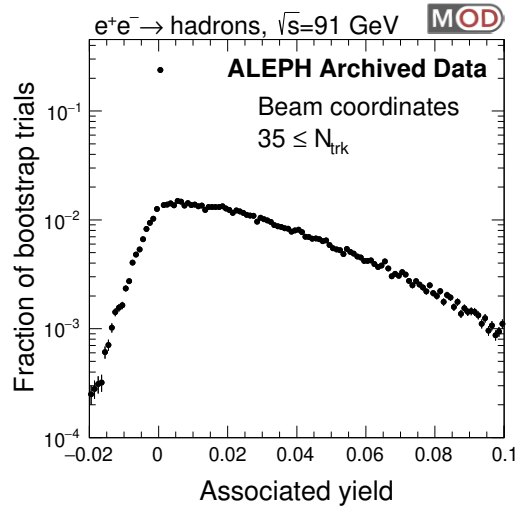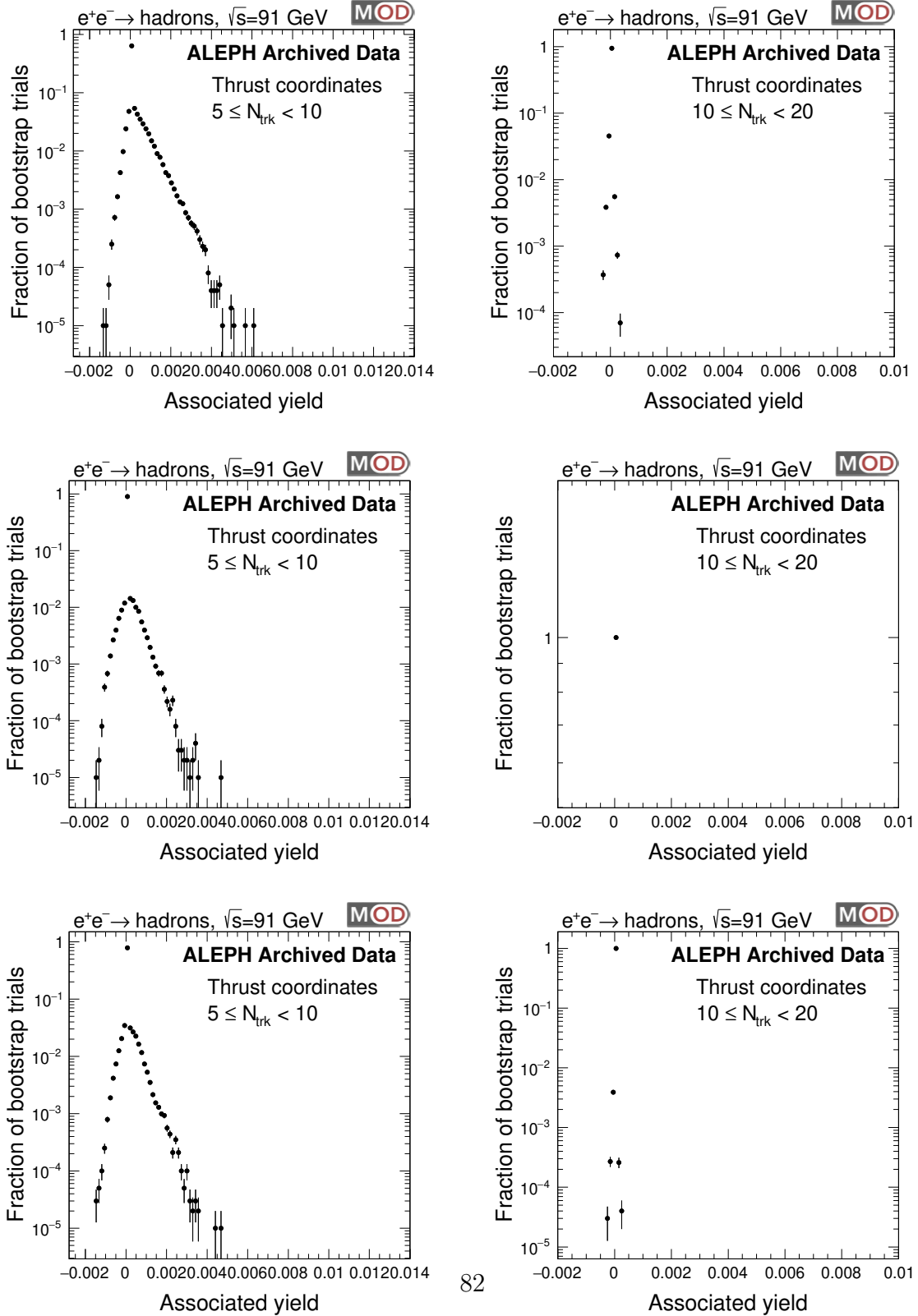
81
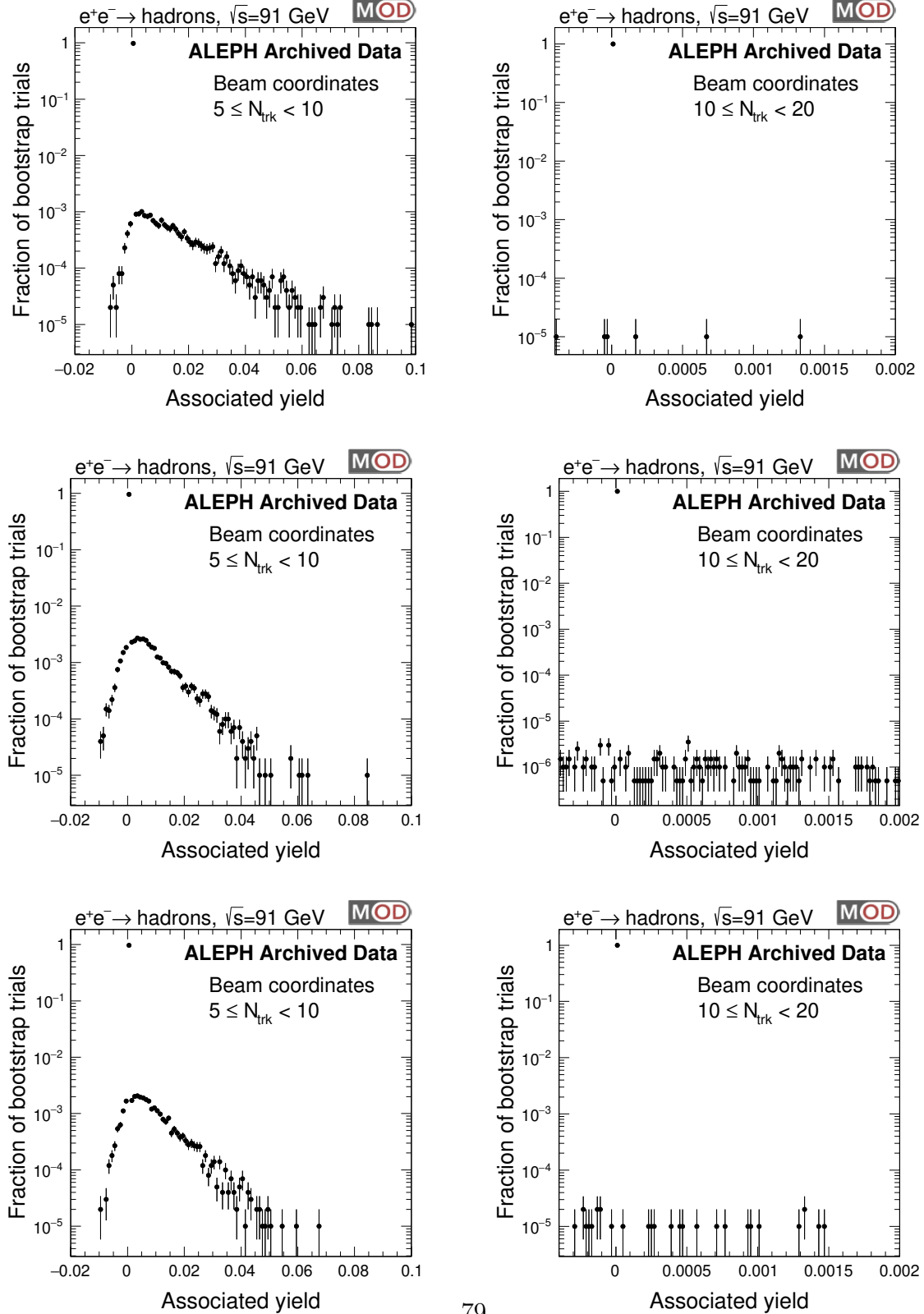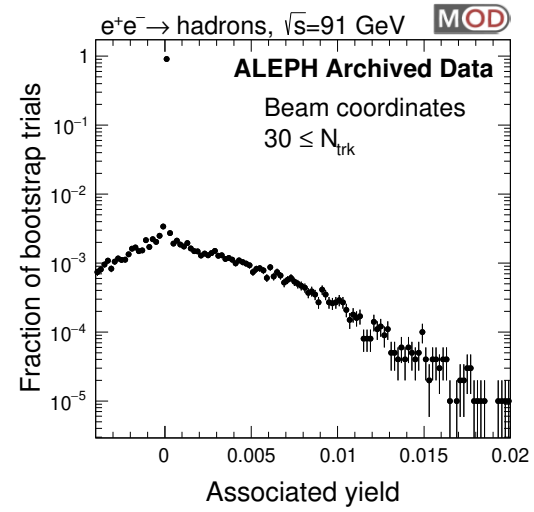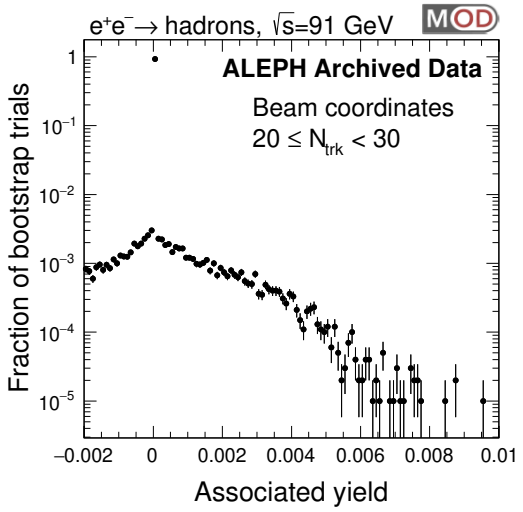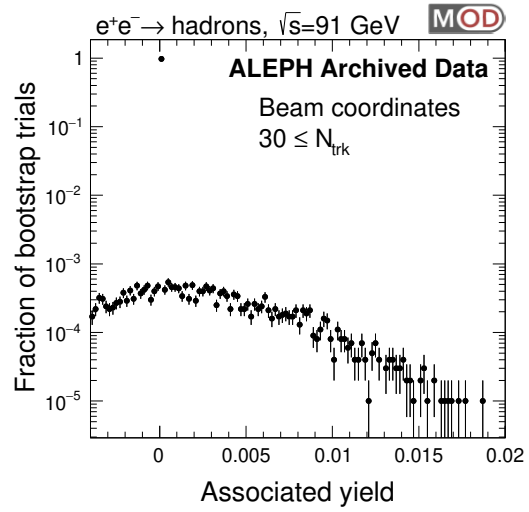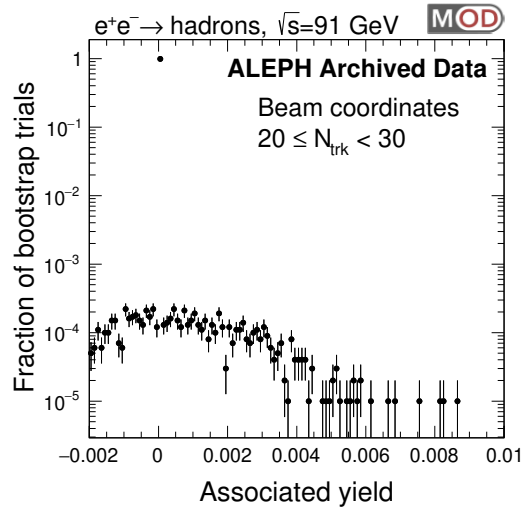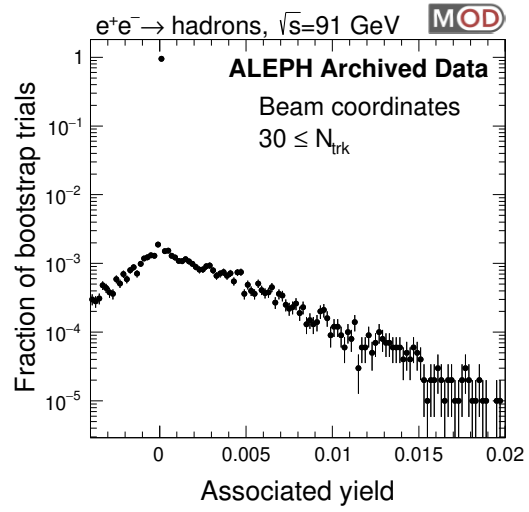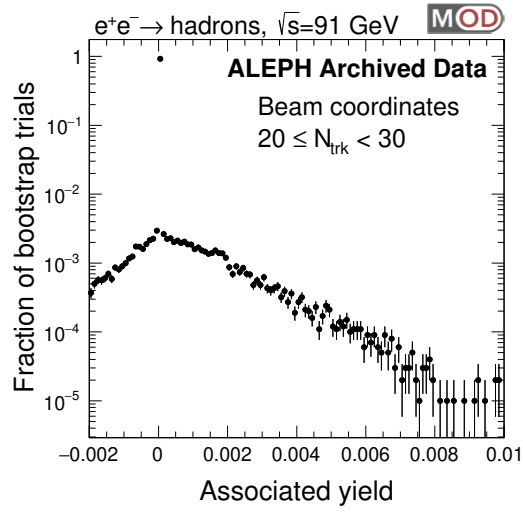
Figure 6-5: Associated yield found with pseudo-data sets in the thrust frame. Multiplicity classes are positioned along the columns and the fit functional forms, as described in Sec. 6.5.2, along the rows: (top) third order polynomial, (middle) second order polynomial plus a second degree cosine term, (bottom) third order Fourier series.
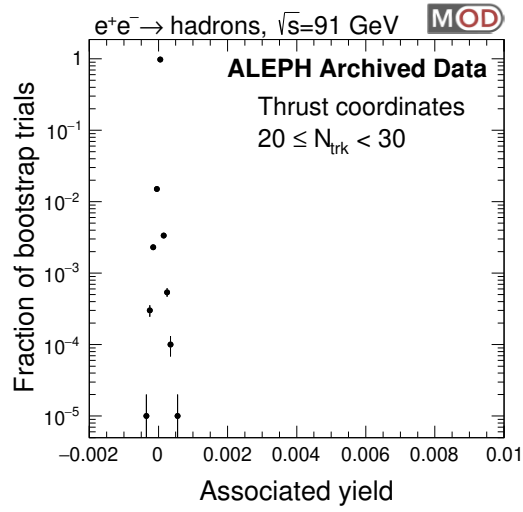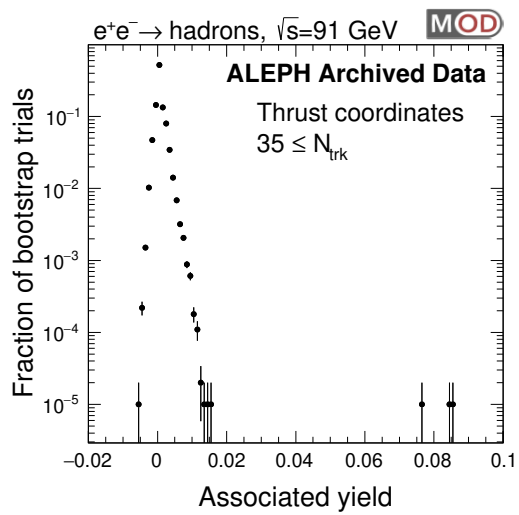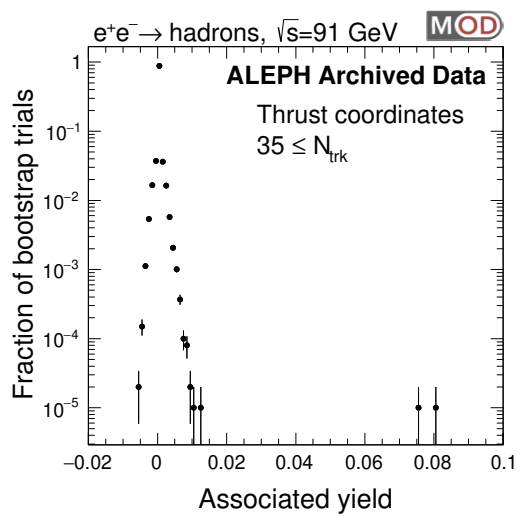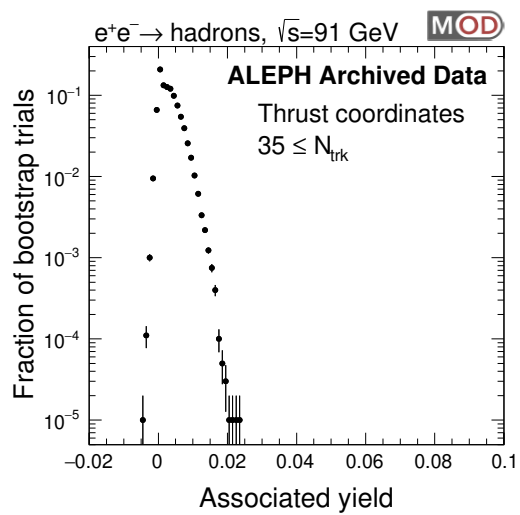
84
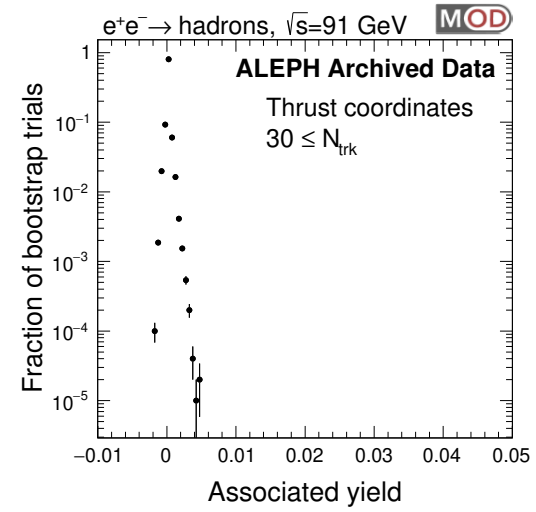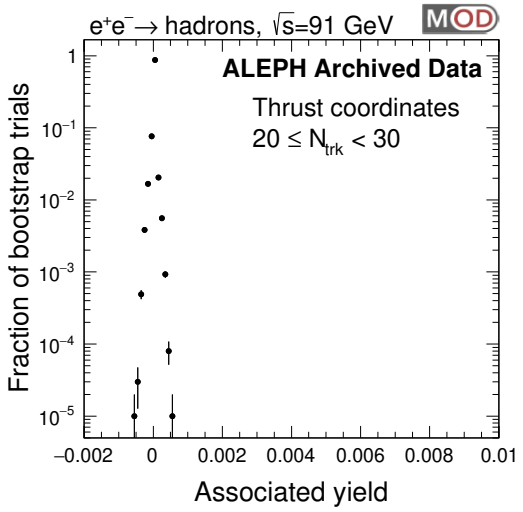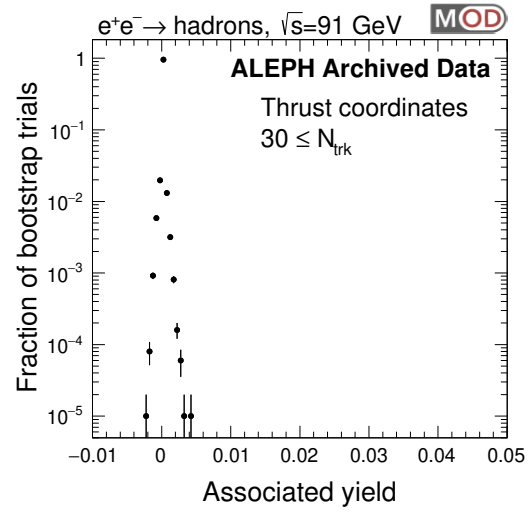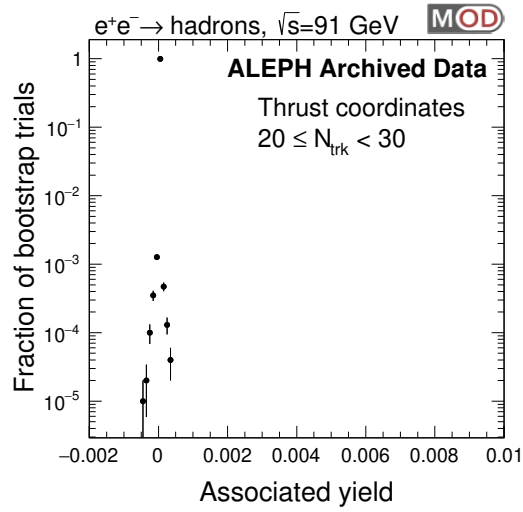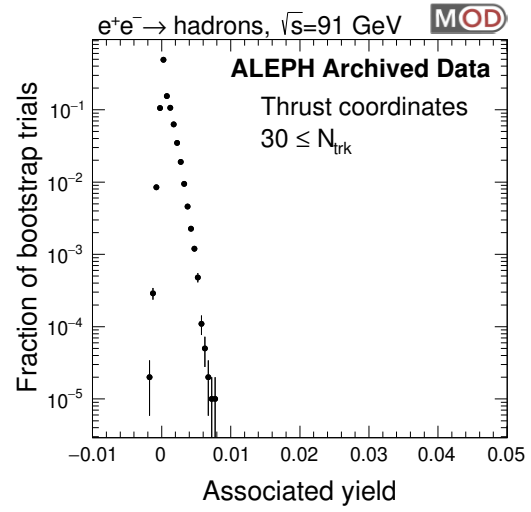
Chapter 7

Analysis Results (Self Contained)

Measurements of two-particle angular correlation functions in high multiplicity proton-proton (pp), proton-nucleus (pA), and nucleus-nucleus (AA) collisions have revealed a ridge-like structure for particle pairs having large differences in pseudorapidity ($\Delta\eta$, where $\eta = -\ln\tan\theta/2$ and the polar angle θ are defined relative to the counterclockwise beam), but small differences in azimuthal angle ($\Delta\phi$) [114, 115, 111, 116, 117, 118, 119]. In AA collisions, this long-range correlation is interpreted as a consequence of hydrodynamical expansion of the Quark-Gluon Plasma (QGP) with initial state fluctuations [120, 121]. However, the physical origin of the ridge signal in pp and pA collisions is not yet understood (see Refs. [122, 123] for recent reviews). Due to the complexity of hadron structure, possible initial state parton correlations could complicate the interpretation of pp and pA measurements. As a result, a large variety of theoretical models with underlying mechanisms ranging from initial state correlations [124], final-state interactions [125] and hydrodynamic effects [126] in the high-density system formed in those collisions have been proposed.

Unlike hadron-hadron collisions, electron-position (e^+e^-) annihilations do not have beam remnants, gluonic initial state radiations, or the complications of a parton distribution function. Therefore, e^+e^- collisions provide a cleaner environment than the larger hadron systems previously used. Furthermore, the initial momenta of the two quarks originating from Z boson decays are fixed. The measurement of events with large final-state particles originating from the two-quark system could

offer significant insights into the origin of the ridge-like signal [127].

This study uses archived data collected by the ALEPH detector at LEP [128] between 1992 and 1995. To analyze the data, an MIT Open Data format was created [129], as discussed in Section 4.1. Hadronic events were selected by requiring the sphericity axis to have a polar angle in the laboratory reference frame (θ_{lab}) between $7\pi/36$ and $29\pi/36$. At least five tracks, having a total energy of at least 15 GeV are also required [108] in order to suppress electromagnetic interactions. The residual contamination from processes such as the $e^+e^- \to \tau^+\tau^-$ is found to be negligible. Approximately 2.4 million e^+e^- collisions resulting in the decay of a Z boson to quarks are analyzed; see Section 4.4 for more details on the event selection.

Event thrust distributions published by the ALEPH Collaboration using a similar data set [109] were successfully reproduced within uncertainties, affirming that the archived data is analyzed properly; see Section 5.2 for the relevant discussion. High-quality tracks from charged particles are selected using requirements identical to those in previous ALEPH analyses [108] and are required to have transverse momentum with respect to the beam axis (p_{T}) above 0.2 GeV, and θ_{lab} between $\pi/9$ and $8\pi/9$ in the lab frame; see Section 4.3 for more details on the track selection. Archived PYTHIA 6.1 [130] Monte Carlo simulation samples are used to derive efficiency correction factors for charged particles and for correction of the detector effects of the correlation functions; see Section 6.4.

The analysis is performed with a procedure similar to previous studies of two-particle correlation functions [111]; see Section 6.2 for a more detailed discussion of the procedure. For each event, the differential yield of the number of charged-particle pairs ($\frac{\text{d}^2\text{N}^{\text{same}}}{\text{d}\Delta\eta\text{d}\Delta\phi}$) is calculated. This quantity is scaled by the number of trigger particles in the event (N_{trig}) and averaged over all events of interest for the per-trigger-particle yield of particle pairs from the same event:

$$S(\Delta\eta, \Delta\phi) = \frac{1}{\text{N}_{\text{trig}}}\frac{\text{d}^2\text{N}^{\text{same}}}{\text{d}\Delta\eta\text{d}\Delta\phi}. \tag{7.1}$$

A mixed-event background correlation function pairing the trigger particles in one event with associated particles in 12 random events (5 in Monte Carlo simulation studies) with similar event multiplicity is also calculated:

$$B(\Delta\eta, \Delta\phi) = \frac{1}{N_{\mathrm{trig}}} \frac{\mathrm{d}^2 N^{\mathrm{mix}}}{\mathrm{d}\Delta\eta \mathrm{d}\Delta\phi}. \tag{7.2}$$

where N^{mix} denotes the number of pairs taken from the mixed event. This mixed-event background correlation function, when scaled by $B(0,0)$, represents the pair acceptance of the detector when particles in the pair are uncorrelated. Thus, the acceptance-corrected differential yield of particle pairs is given by

$$\frac{1}{N_{\mathrm{trig}}} \frac{\mathrm{d}^2 N^{\mathrm{pair}}}{d\Delta\eta \mathrm{d}\Delta\phi} = B(0,0) \times \frac{S(\Delta\eta, \Delta\phi)}{B(\Delta\eta, \Delta\phi)}. \tag{7.3}$$

To study the event multiplicity dependence of the correlation function, the analysis is performed with events in 5 multiplicity intervals classified by the number of reconstructed charged tracks (N_{trk}). The multiplicity ranges used, the corresponding fraction of the total sample, and the average number of tracks for each multiplicity class before ($\langle N_{\mathrm{trk}} \rangle$) and after detection efficiency correction ($\langle N_{\mathrm{trk}}^{\mathrm{corr}} \rangle$) are summarized in Table 6.1.

The analysis is first performed with lab coordinates, similar to previous analyses at hadron colliders. In the hydrodynamics picture, the lab coordinate analysis is sensitive to QCD medium expanding transverse to the beam axis. However, this coordinate system, although identical to that was used in the studies of heavy ion collisions, may not be the most sensible for the analysis of e^+e^- collisions. Instead, using a coordinate system with the z axis defined by the outgoing $q\bar{q}$ from the Z decay enables a search for signal associated with QCD medium expanding transverse to the $q\bar{q}$ color-string. The thrust axis is closely related to the direction of the outgoing $q\bar{q}$ pair and is used to define the coordinate system for this second type of analysis; see Section 6.3 for a more detailed discussion of the lab and thrust coordinates.

For the purposes of calculating the thrust direction, an extra particle correspond-
ing to the missing momentum of the event is included; see Section 5.1 for a discussion
of the thrust axis calculation. This reduces the effects of detector inefficiencies on the
final correlation function. Each particle's kinematics (p_{T}, η, ϕ) are then recalculated
using this thrust axis to replace the role of the beam axis. The variation of the thrust
axis direction causes the ALEPH detector acceptance in the thrust coordinates to
vary on an event-by-event basis. This is accounted for by recalculating the kinemat-
ics for particles in mixed event with respect to the thrust axis in the signal event. The
η and ϕ distributions of the charged tracks in the mixed events is then re-weighted
to match that of signal events; see Section 6.4.2 for the details of the thrust mixing
correction.

The systematic uncertainty of the result is evaluated following a procedure similar
to previous ALEPH studies [108]. The required number of hits a track leaves in
the ALEPH time projection chamber was varied from 4 to 7. From this variation,
the tracking uncertainty is estimated to be 0.7% in the lab coordinate analysis and
0.3% in the thrust coordinate analysis. The hadronic event selection was studied
by changing the required charged energy in an event to be 10 GeV instead of 15
GeV. This only affects the lowest multiplicity bin, where an uncertainty of 0.6%
(3.4%) is quoted for the lab (thrust) coordinate analysis for the lowest N_{Trk} bin. A
small correlated uncertainty of 0–0.1% (0.05–0.9%) on the value of $B(0,0)$ in the lab
(thrust) coordinate analysis arising from statistical fluctuations is also included as a
component of the systematic uncertainties; refer to Section 6.2 for a more detailed
account of the systematic uncertainties.

The lab and thrust coordinates two-particle correlation functions for events from
the archived ALEPH data are shown in Fig. 7-1 and Fig. 7-2. The dominant feature
is the jet peak near $(\Delta\eta, \Delta\phi) = (0,0)$ arising from particle pairs within the same jet.
The away-side structure at $\Delta\phi \sim \pi$ arises from pairs of particles contained in back-to-
back jets. Because many charged particles are approximately aligned with the thrust
axis, i.e., at very large η in the thrust coordinate, particle pairs in back-to-back jets
frequently have a $\Delta\eta$ larger than the $\Delta\eta$ range examined here, and do not contribute

to the correlation function in the analyzed $\Delta\eta$ window. This reduces the absolute magnitude of the correlation function in thrust coordinate analysis with respect to that in lab coordinate analysis. Unlike previous results from hadron collisions, no significant "ridge" structure is found around $\Delta\phi = 0$ in both lab and thrust coordinate analysis.

Figure 7-1: Two-particle correlation functions measured using beam coordinates.
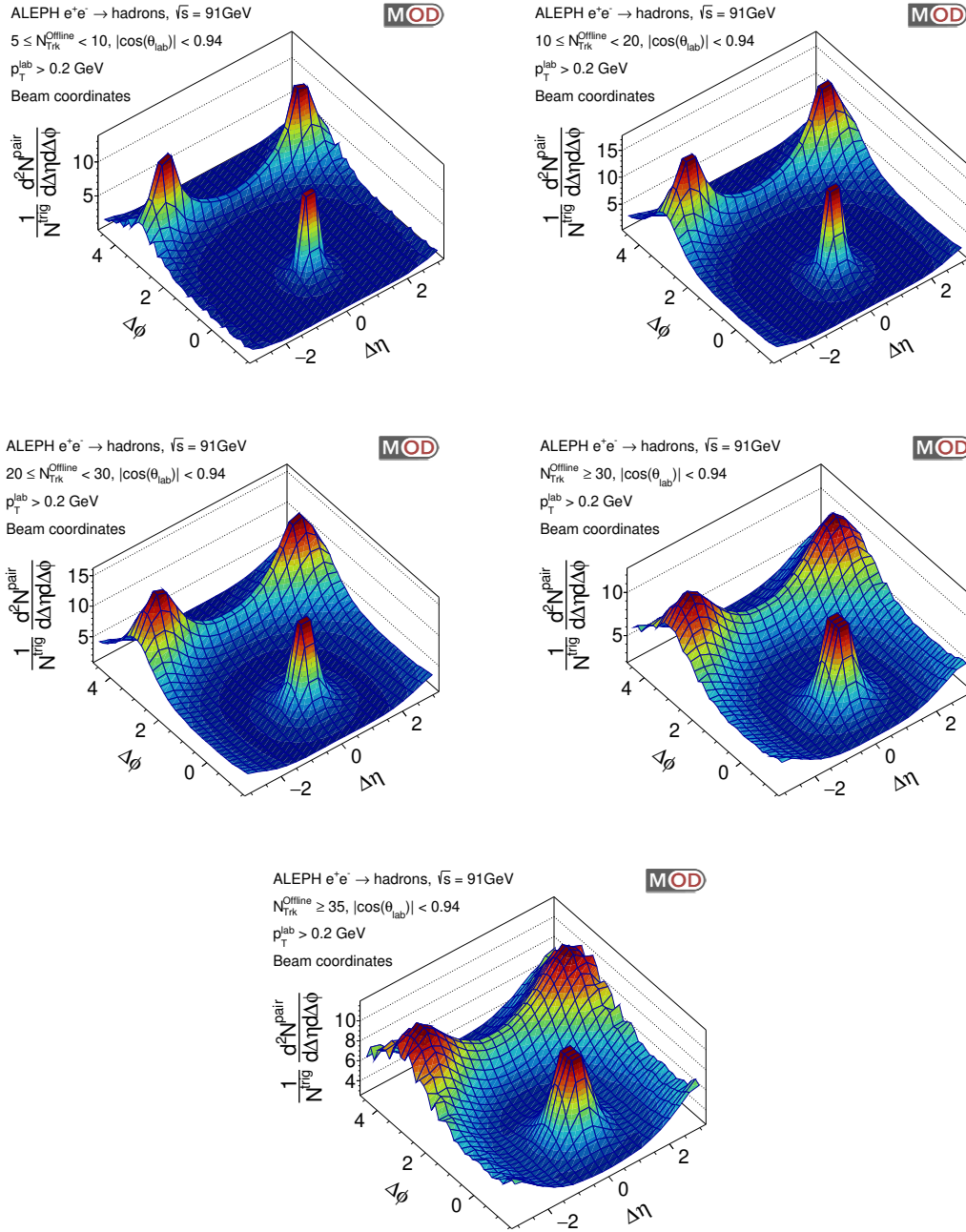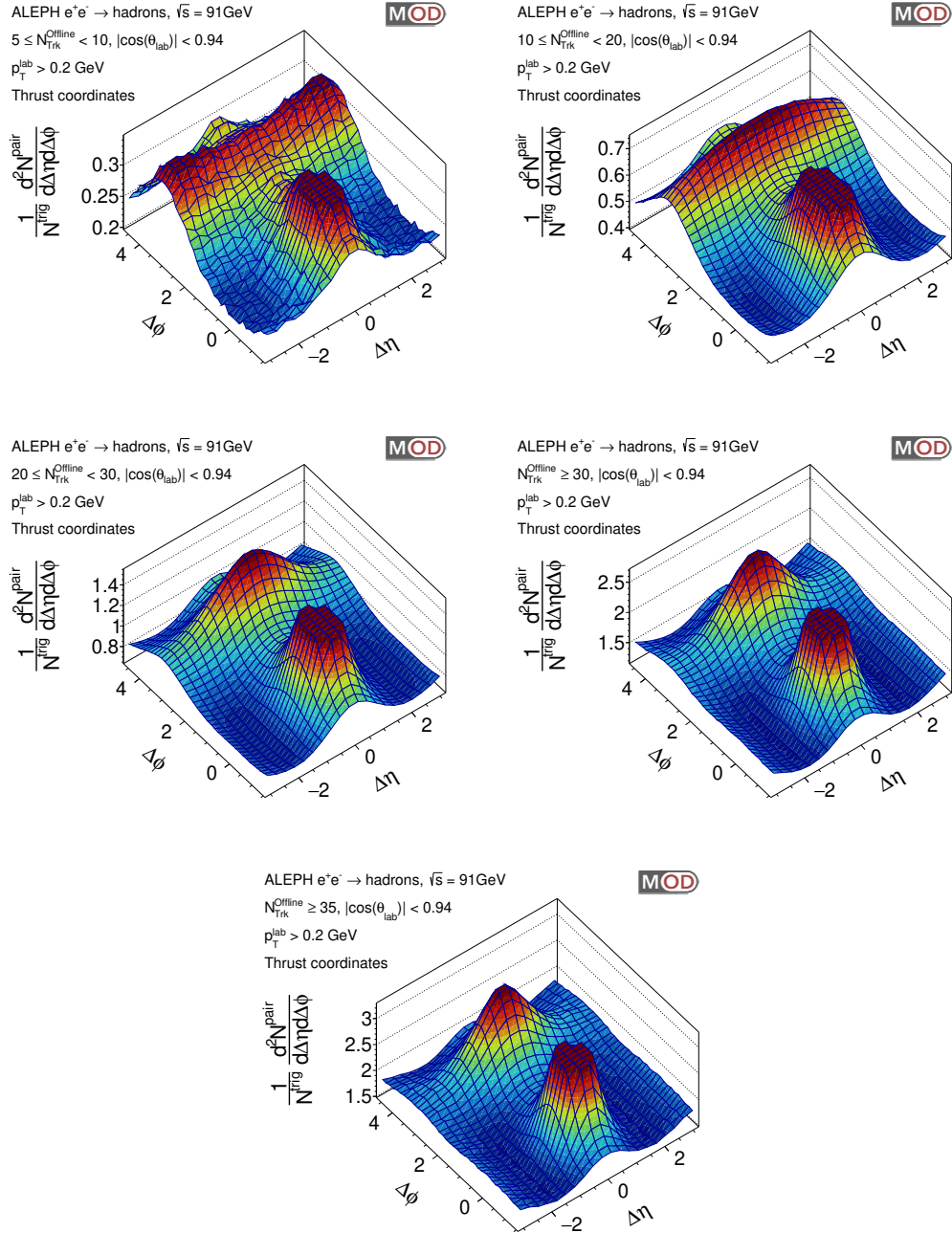
Figure 7-2: Two-particle correlation functions measured using thrust coordinates.

To investigate the long-range correlation in finer detail, one-dimensional (1-D) distributions in $\Delta\phi$ are found by averaging two-particle correlation functions over the region between $1.6 < |\Delta\eta| < 3.2$. The size of any potential enhancement around $\Delta\phi = 0$ is calculated by fitting this distribution from $0 < \Delta\phi < \pi/2$ and then performing a zero yield at minimum (ZYAM) subtraction procedure using the fit minimum, c_{ZYAM} [131]. A constant plus a three term Fourier series was used as the nominal fit function, but a fourth degree polynomial fit and third degree polynomial plus a $\cos 2\Delta\phi$ term were also attempted. Discrepancies resulting from these different choices of fit function were found to be small and are included in the systematic uncertainties of the total near-side yield calculation; see Section 6.4.3 for an more detailed explanation of this uncertainty. The results after this subtraction are shown for all multiplicity bin studies in Fig. 7-3. The red points show the 1D correlation function for the analysis using lab coordinates. The red error bars show the statistical uncertainties, while the light red boxes show systematic uncertainties. The red points have been scaled by a constant factor of 0.05. The thin red line between $0 < \Delta\phi < \pi/2$ shows the fit used to calculate c_{ZYAM}. A sharp peak is seen at $\Delta\phi = \pi$, but the distribution decreases to values consistent with zero at $\Delta\phi = 0$. The results for the thrust coordinate analysis are shown by the black points which have similar structures as the lab coordinate analysis.

Figure 7-3: The differential yield of charged particle pairs in the pseudorapidity range $1.6 < |\Delta\eta| < 3.2$ after ZYAM subtraction for both the lab (red) and thrust (black) coordinates. Lab points are scaled by 0.05 for presentation purposes. No enhancement is seen in the "ridge" region, at $\Delta\phi \sim 0$ and large $\Delta\eta$.
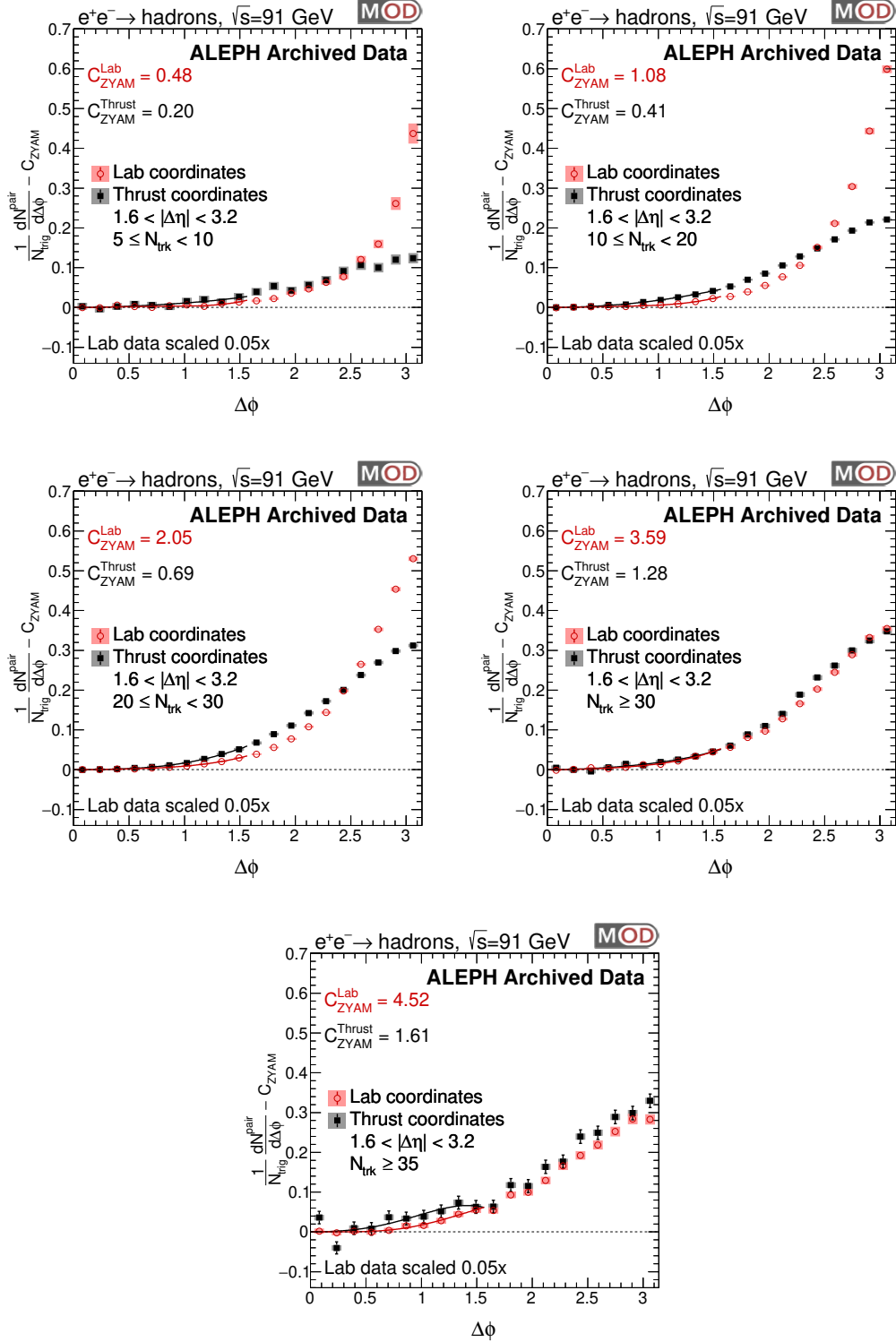
The results are also compared to predictions from PYTHIA v6.1, PYTHIA v8.230 and HERWIG v7.1.5 generators as shown in Fig. 7-5, 7-6,7-7, 7-8, 7-9, 7-10, 7-11, and 7-12, respectively. A better agreement between data and both versions of PYTHIA predictions is observed. The differential yield at large $\Delta\phi$ is slightly under-predicted by both versions of PYTHIA generators and over-predicted by HERWIG.

The total size of any excess yield of particle pairs around $\Delta\phi = 0$ is quantified by integrating the data from $\Delta\phi = 0$ to the position in $\Delta\phi$ of the ZYAM fit's minimum. In general, no significant enhancement of particle pairs is observed in any of the multiplicity bins examined for both the lab and thrust coordinate analyses. Therefore, a confidence limit on the near-side excess of particle pairs is calculated using a bootstrap procedure [112]. This method calculates the distribution of the associated yield after allowing the one-dimensional correlation function data points to vary according to their uncertainties. Most of these variations result in a correlation function that has a minimum as $\Delta\phi = 0$ and therefore zero associated yield. If more than 5% of the data variations have a yield above 1×10^{-5}, a 95% confidence limit is quoted. Otherwise if 1% of the variations are $> 1 \times 10^{-5}$, a 99% confidence limit is reported. The 10–20 multiplicity selection in the lab coordinate analysis has a 99.99% confidence limit reported because the data have relatively small uncertainties, making it extremely unlikely that a bootstrap variation produces any nonzero associated yield. These confidence limits are shown as a function of $N_{\mathrm{trk}}^{\mathrm{corr}}$ in Fig. 7-4 (left) by the red arrows for the lab coordinate analysis and black arrows for the thrust coordinate analysis. The lab coordinate data have been shifted to the right by three units for visual clarity. In general, the constraining power of data is driven by statistical uncertainties, with multiplicity bins having more events also having lower confidence limits.

In summary, the first measurements of two-particle angular correlations for charged particles emitted in e^+e^- collisions at a center-of-mass energy of 91 GeV are presented using archived data collected with the ALEPH detector at LEP. The correlation functions are measured over a broad range of pseudorapidity and azimuthal angle of the charged particles. Those results using either lab coordinates or the event thrust coor-
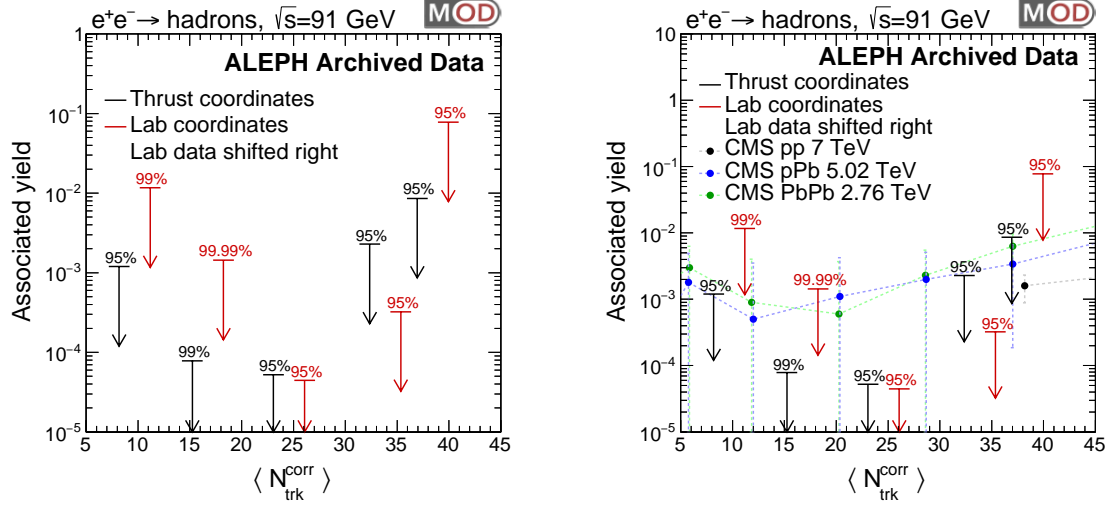
Figure 7-4: (left) Upper limits on the differential yield of charged particle pairs in the pseudorapidity range $1.6 < |\Delta\eta| < 3.2$ after ZYAM subtraction for both the lab (red) and thrust (black) coordinates. The number above the data point indicates the confidence interval percentage used. (right) Comparison between the upper limits and pp, pA, and AA associated yields scaled by the η detector acceptance ratio and the average minimum bias tracking efficiency.

dinates are compared to predictions from the PYTHIA and HERWIG event generators. In contrast to the results from high charged particle multiplicity pp, pA and AA collisions, where long-range correlations with large pseudorapidity gap are observed, no significant enhancement of long-range correlations is observed. See Fig. 7-4 (right) for a comparison of the associated yields for e^+e^-, pp (7 TeV), pA (5.02 TeV), and AA (2.76 TeV). The CMS results are scaled by the η detector acceptance ratio, $1.74/2.4$, and the average minimum bias tracking efficiency 1.15. The results are better described by PYTHIA generators than HERWIG, which in both generators do not include additional final-state interactions of the outgoing partons. Those results provide new insights to the hadronization modeling and serve as an important reference to the observed long-range correlation in high multiplicity pp, pA and AA collisions.

7.1 Event Generator Correlation Functions

Figure 7-5: Two-particle correlation functions measured using lab (beam) coordinates for reconstructed PYTHIA 6.1.
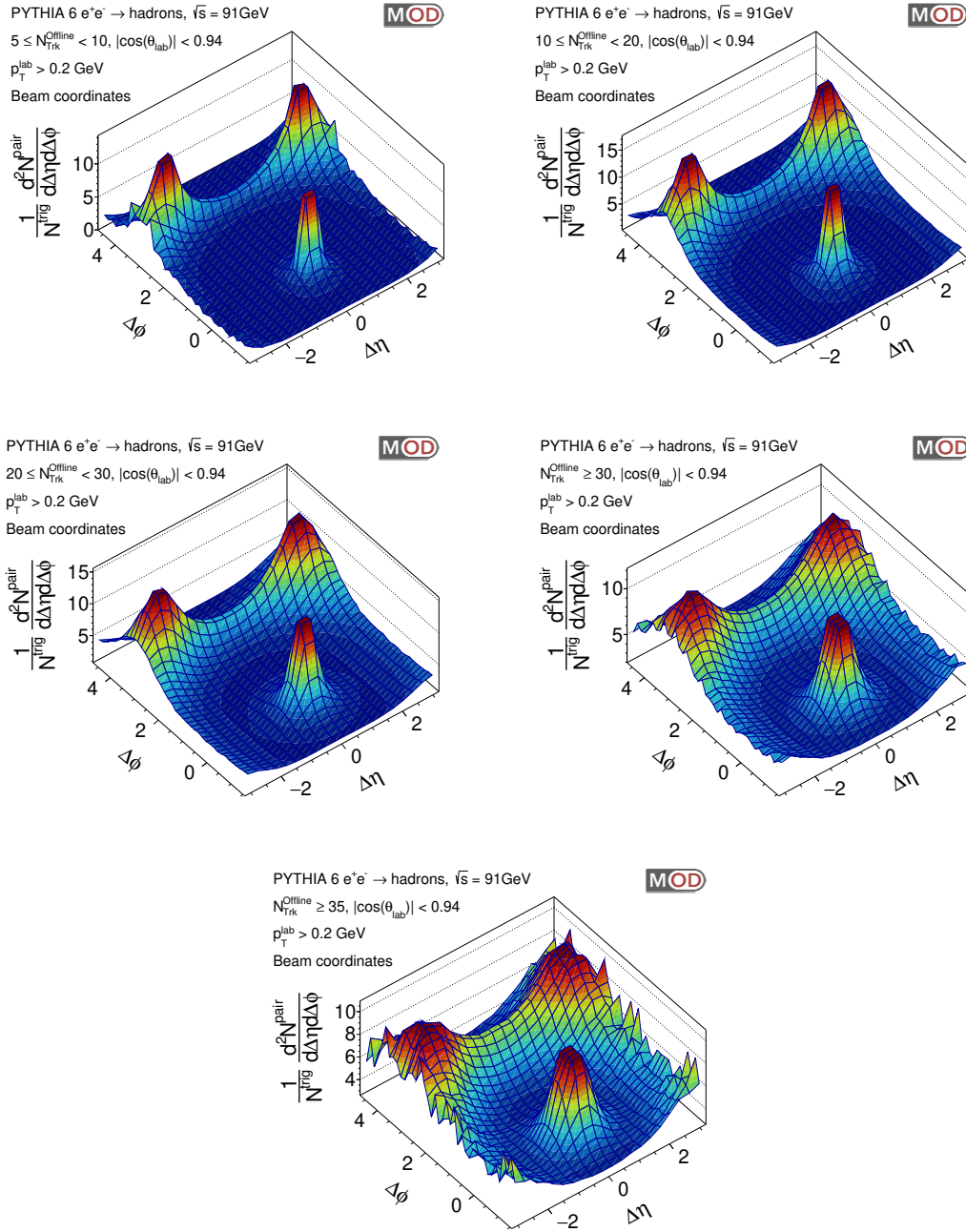
Figure 7-6: Two-particle correlation functions measured using thrust coordinates for reconstructed PYTHIA 6.1.
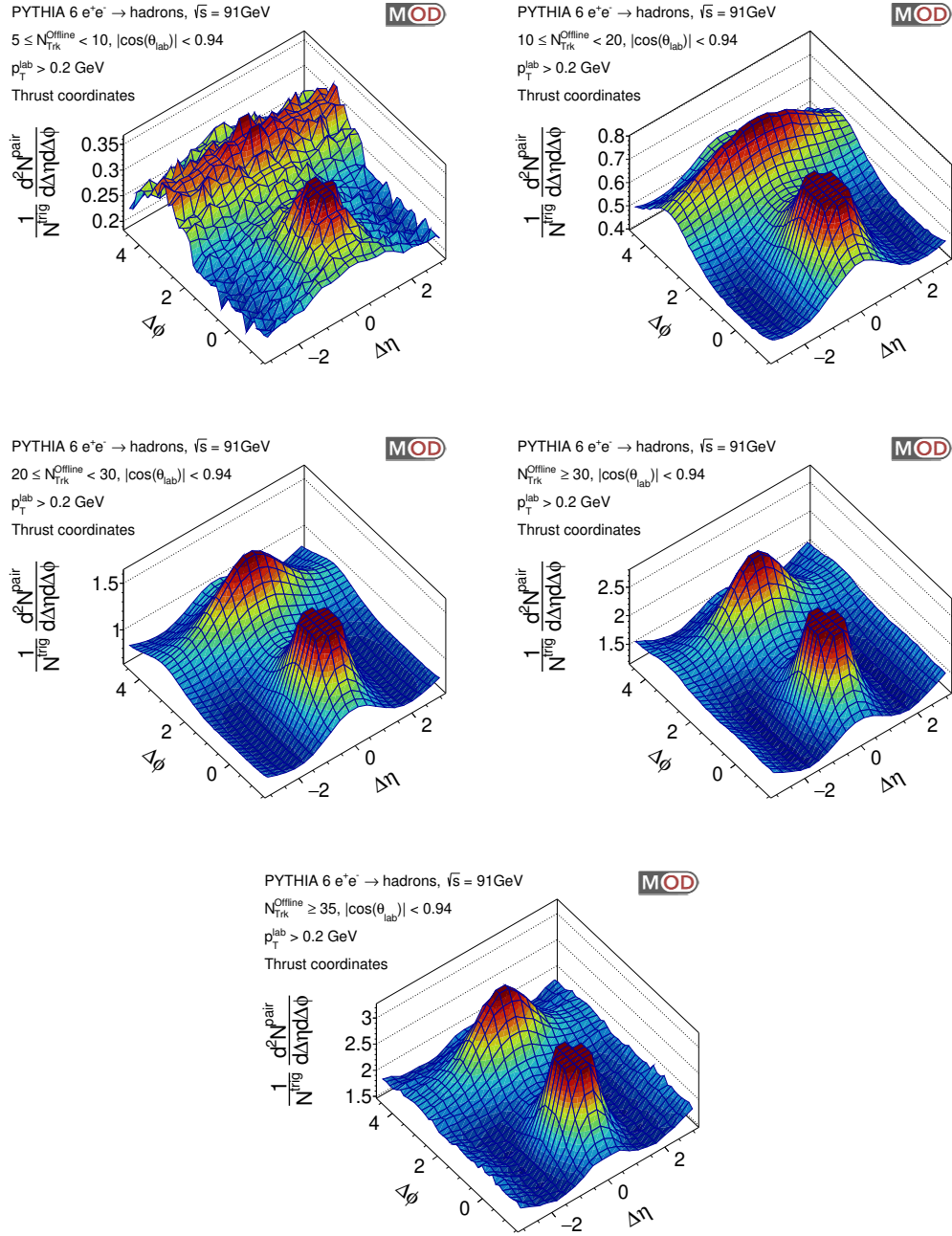
Figure 7-7: Two-particle correlation functions measured using lab (beam) coordinates for generator level PYTHIA 6.1.
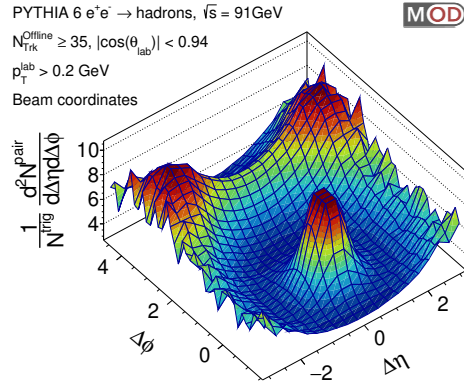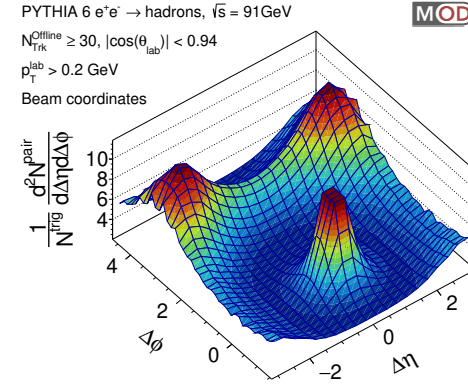
Figure 7-8: Two-particle correlation functions measured using thrust coordinates for generator level PYTHIA 6.1.

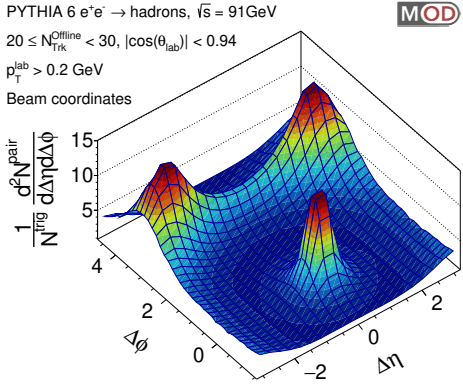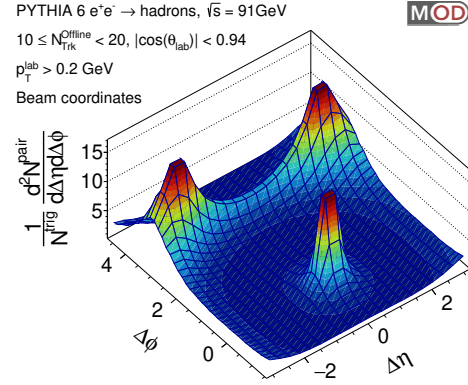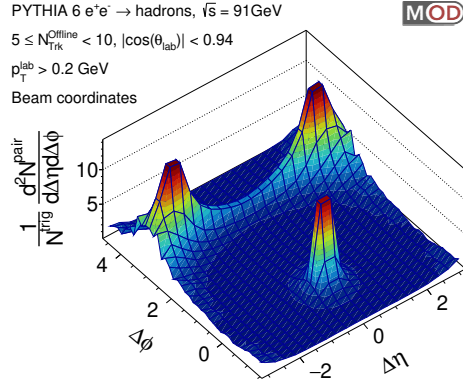Figure 7-9: Two-particle correlation functions measured using lab (beam) coordinates for generator level PYTHIA 8.230.
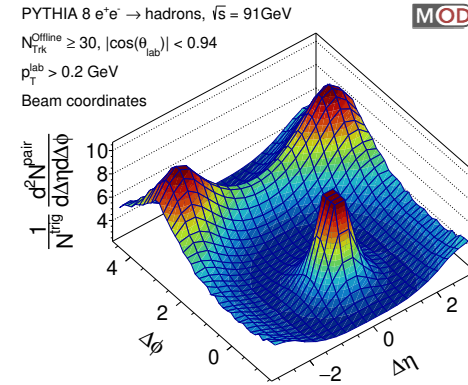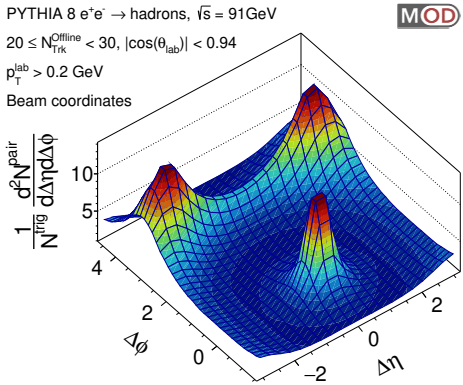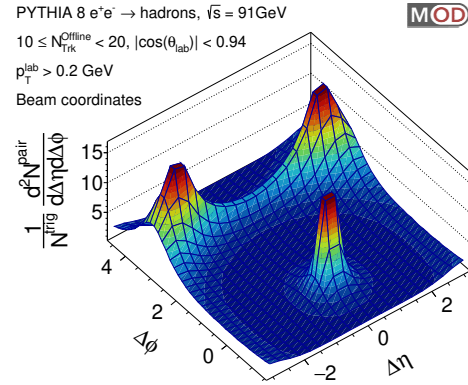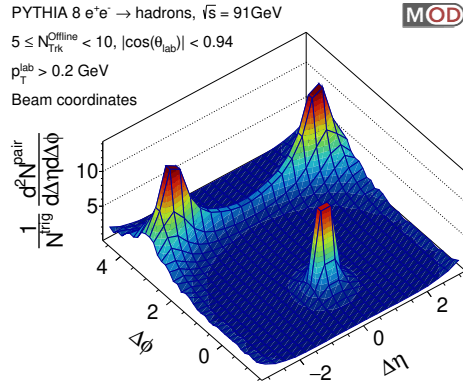
Figure 7-10: Two-particle correlation functions measured using thrust coordinates for generator level PYTHIA 8.230.
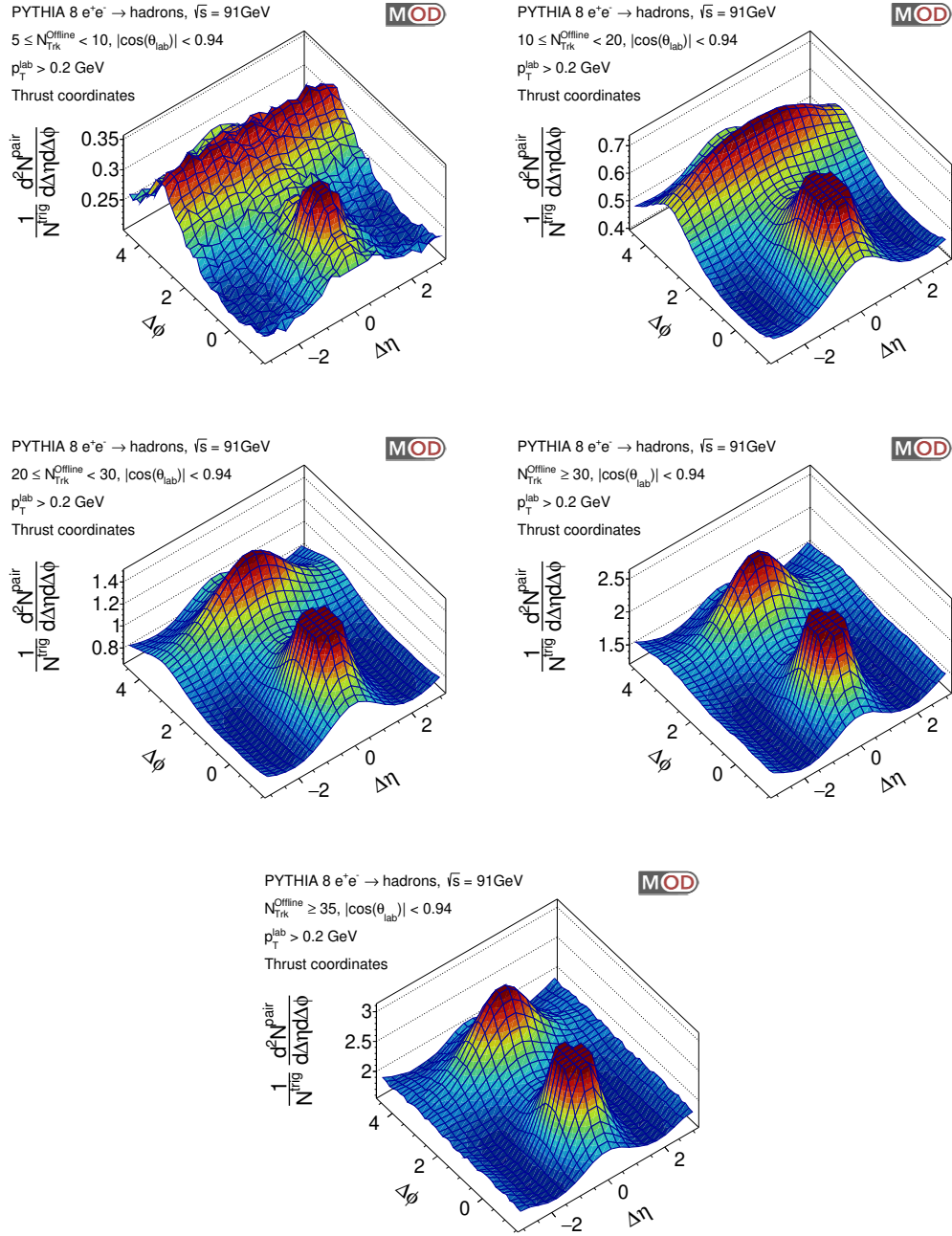
Figure 7-11: Two-particle correlation functions measured using lab (beam) coordinates for generator level HERWIG 7.1.5.

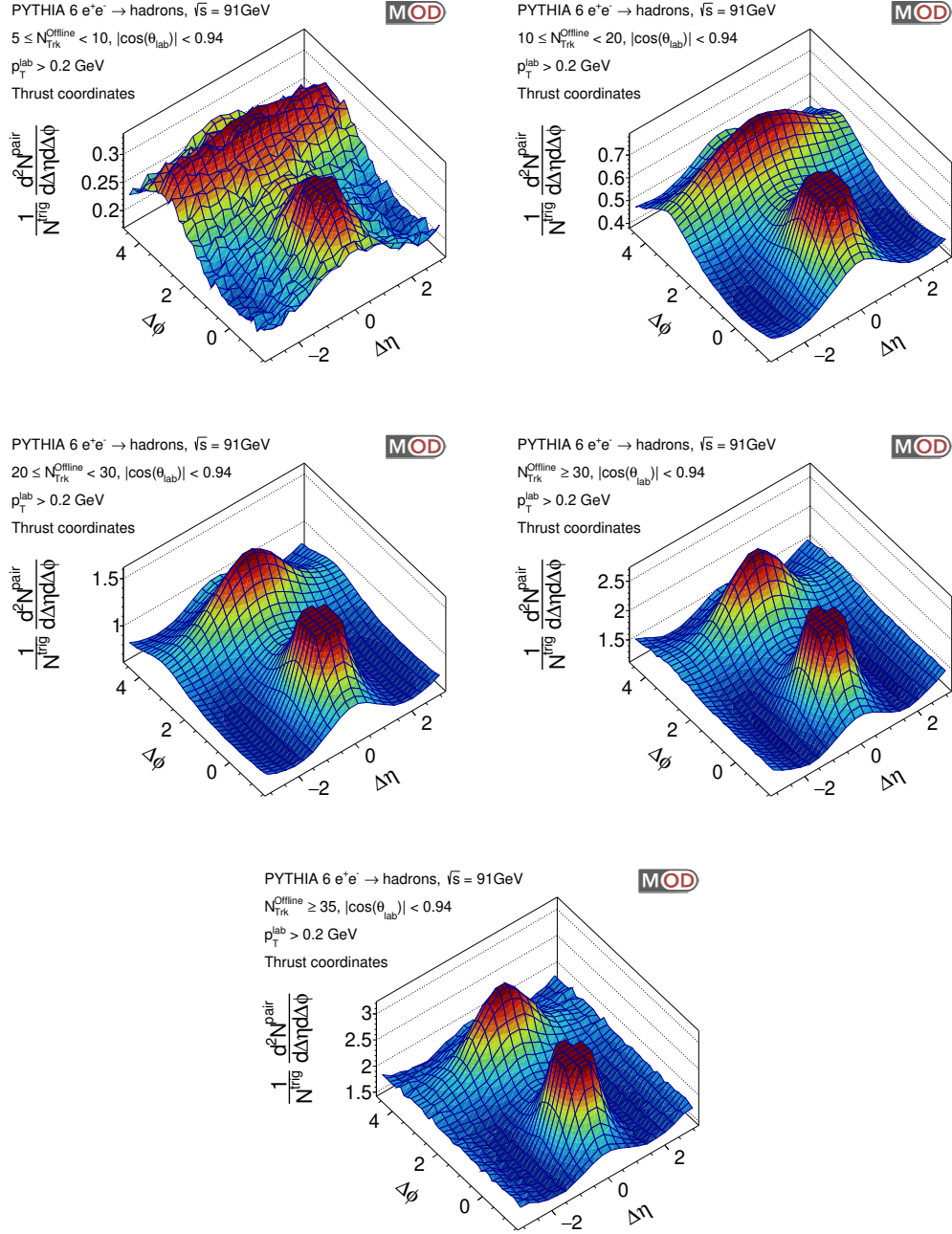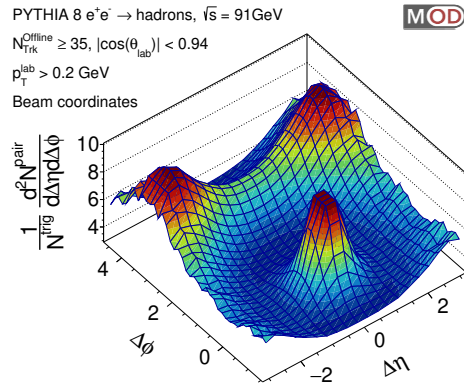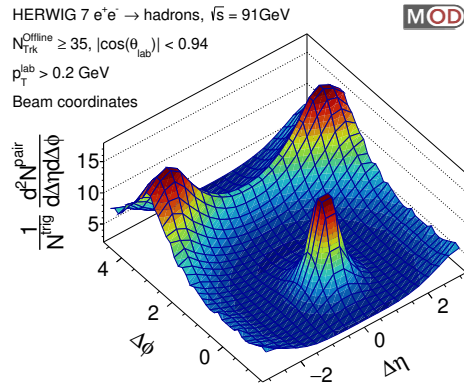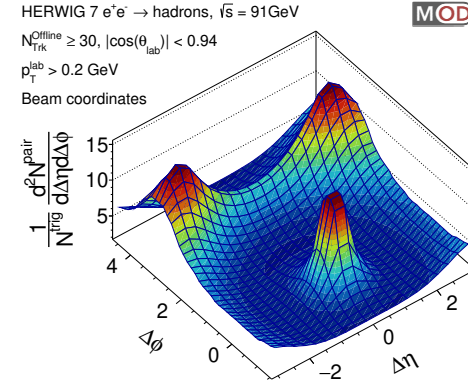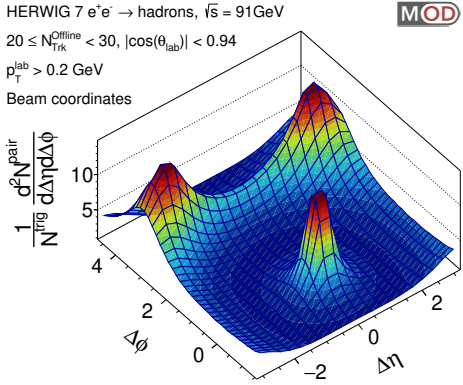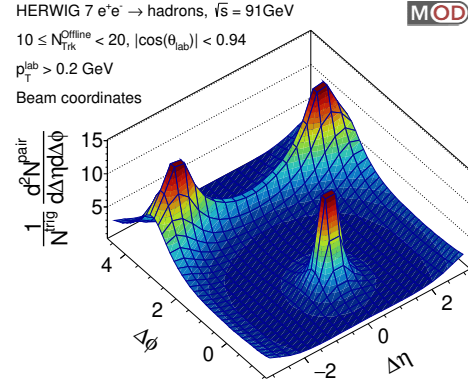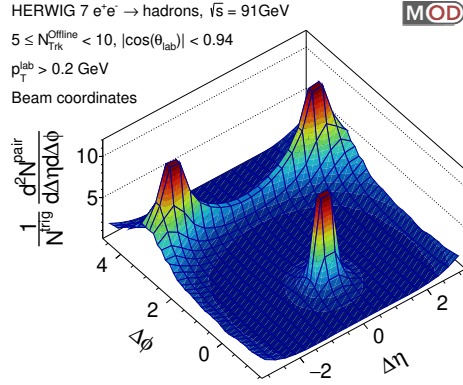Figure 7-12: Two-particle correlation functions measured using thrust coordinates for generator level HERWIG 7.1.5.
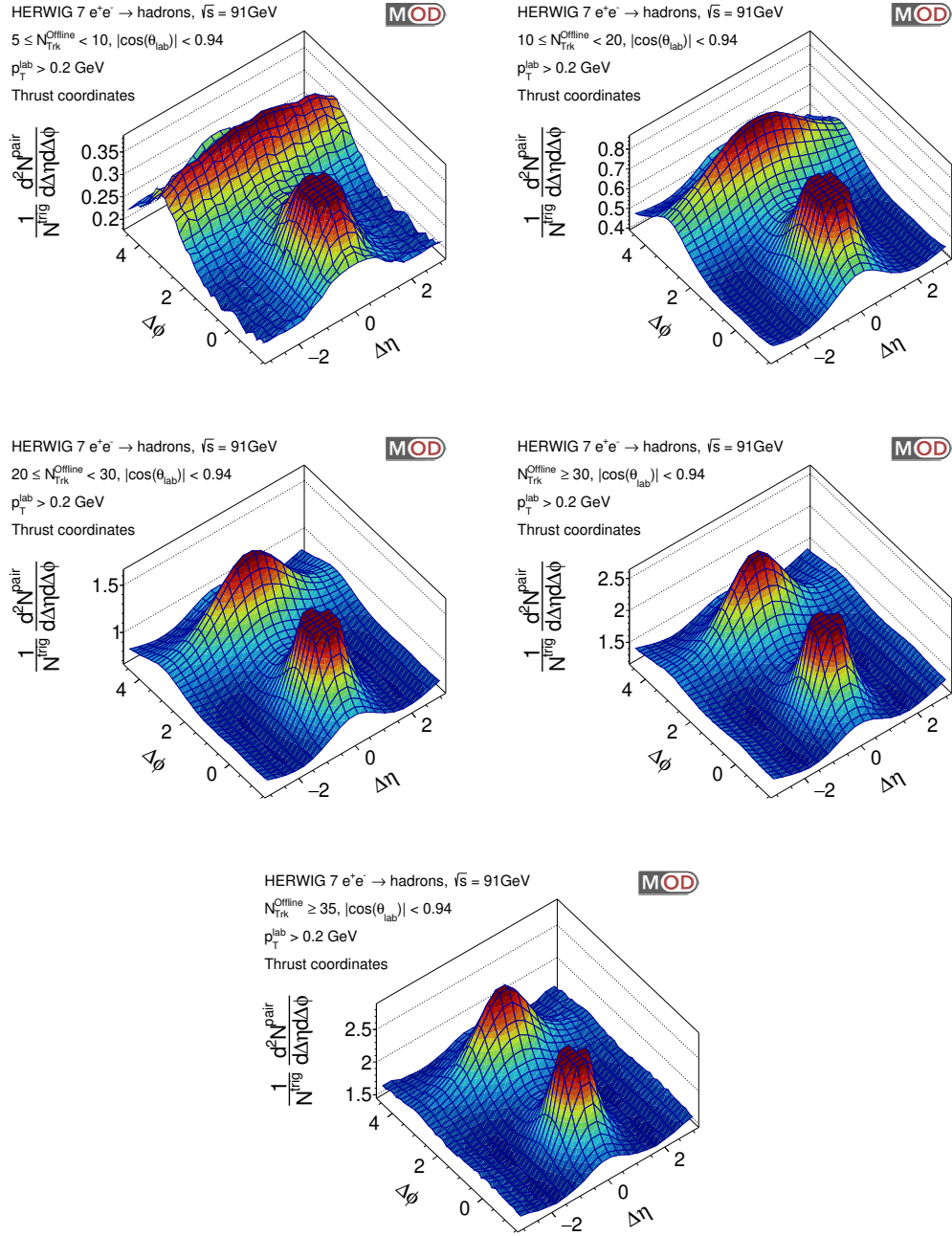
7.2 Event Generator Differential Yields

Figure 7-13: The differential yield of charged particle pairs in the pseudorapidity range $1.6 < |\Delta\eta| < 3.2$ after ZYAM subtraction using lab coordinates for both data (red) and Monte Carlo (black) for $5 \leq N_{trk} < 10$ (left) and $10 \leq N_{trk} < 20$ (right). The rows are ordered by generator level PYTHIA 6.1, PYTHIA 8.230, HERWIG 7.1.5.
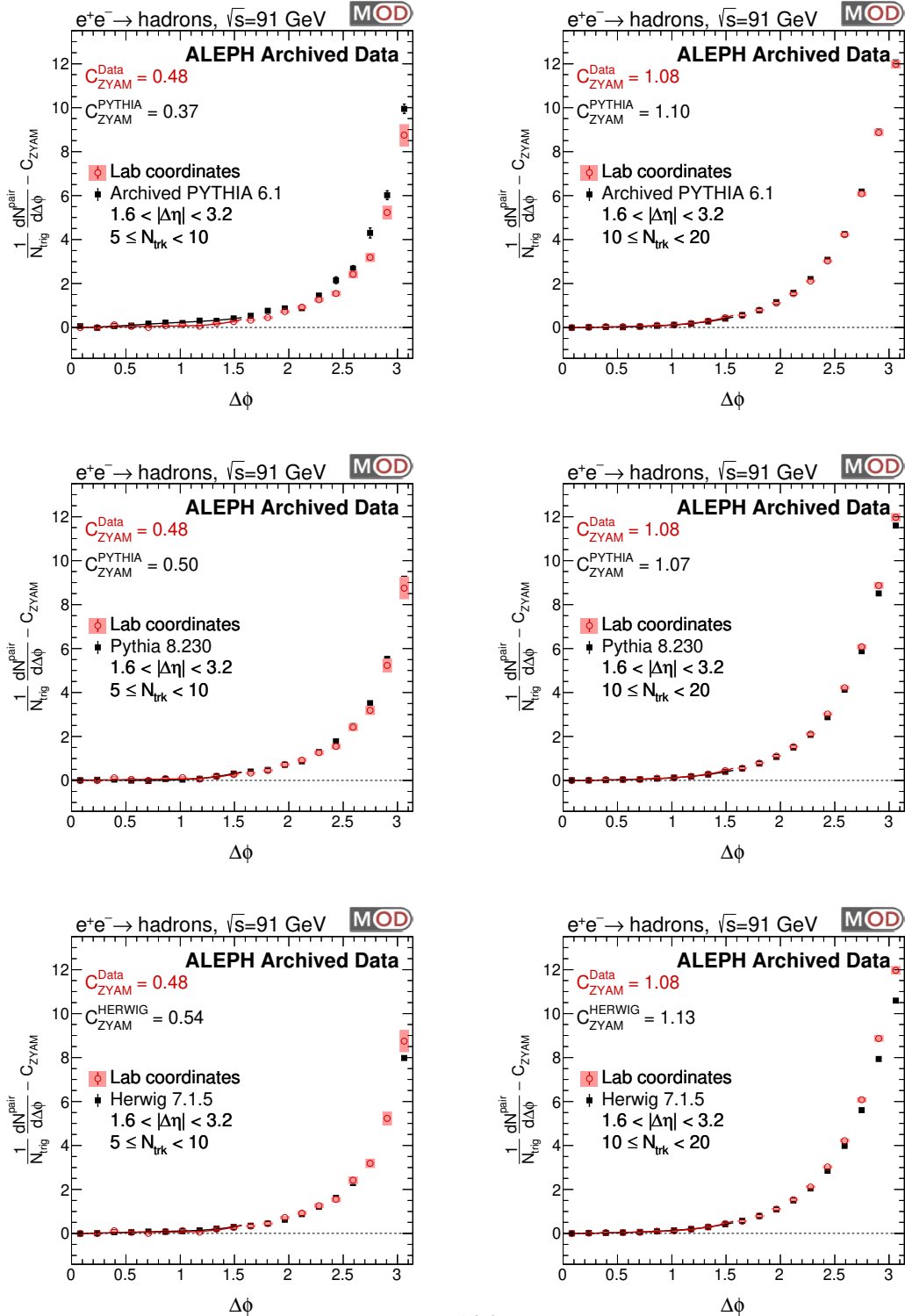
Figure 7-14: The differential yield of charged particle pairs in the pseudorapidity range $1.6 < |\Delta\eta| < 3.2$ after ZYAM subtraction using lab coordinates for both data (red) and Monte Carlo (black) for $20 \leq N_{trk} < 30$ (left) and $N_{trk} \geq 30$ (right). The rows are ordered by generator level PYTHIA 6.1, PYTHIA 8.230, HERWIG 7.1.5.
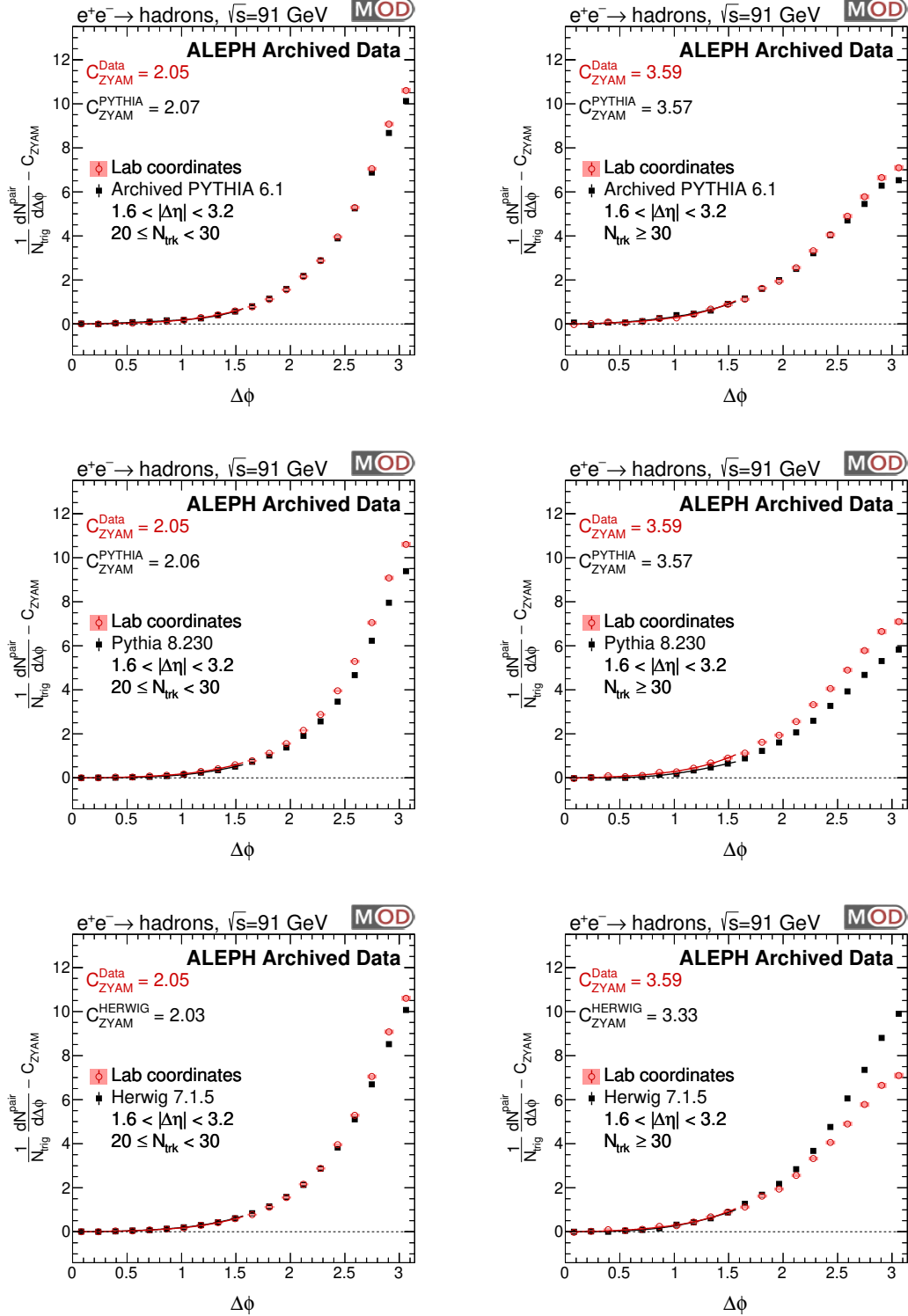
Figure 7-15: The differential yield of charged particle pairs in the pseudorapidity range $1.6 < |\Delta\eta| < 3.2$ after ZYAM subtraction using lab coordinates for both data (red) and Monte Carlo (black) for $N_{trk} \geq 35$. The figures are ordered by generator level PYTHIA 6.1 (top left), PYTHIA 8.230 (top right), HERWIG 7.1.5 (bottom).
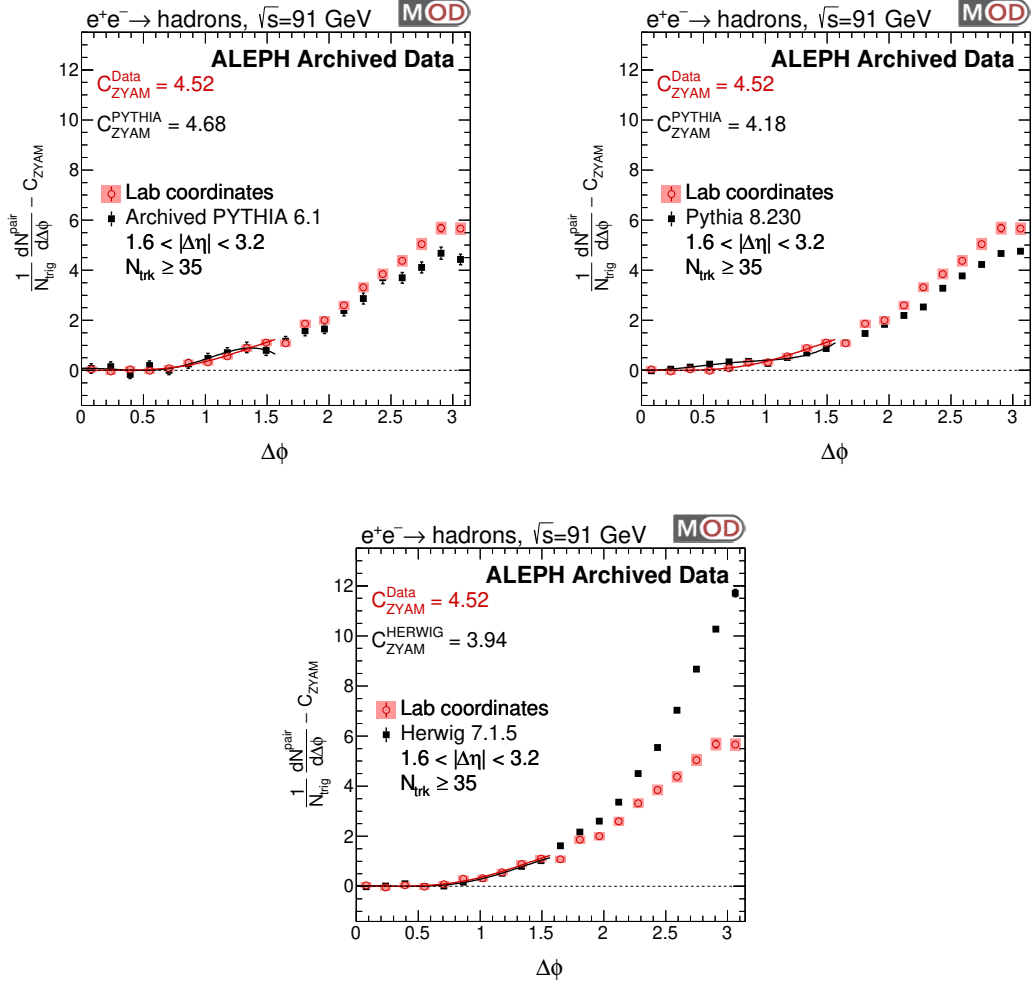
Figure 7-16: The differential yield of charged particle pairs in the pseudorapidity range $1.6 < |\Delta\eta| < 3.2$ after ZYAM subtraction using thrust coordinates for both data (red) and Monte Carlo (black) for $5 \leq N_{trk} < 10$ (left) and $10 \leq N_{trk} < 20$ (right). The rows are ordered by generator level PYTHIA 6.1, PYTHIA 8.230, HERWIG 7.1.5.
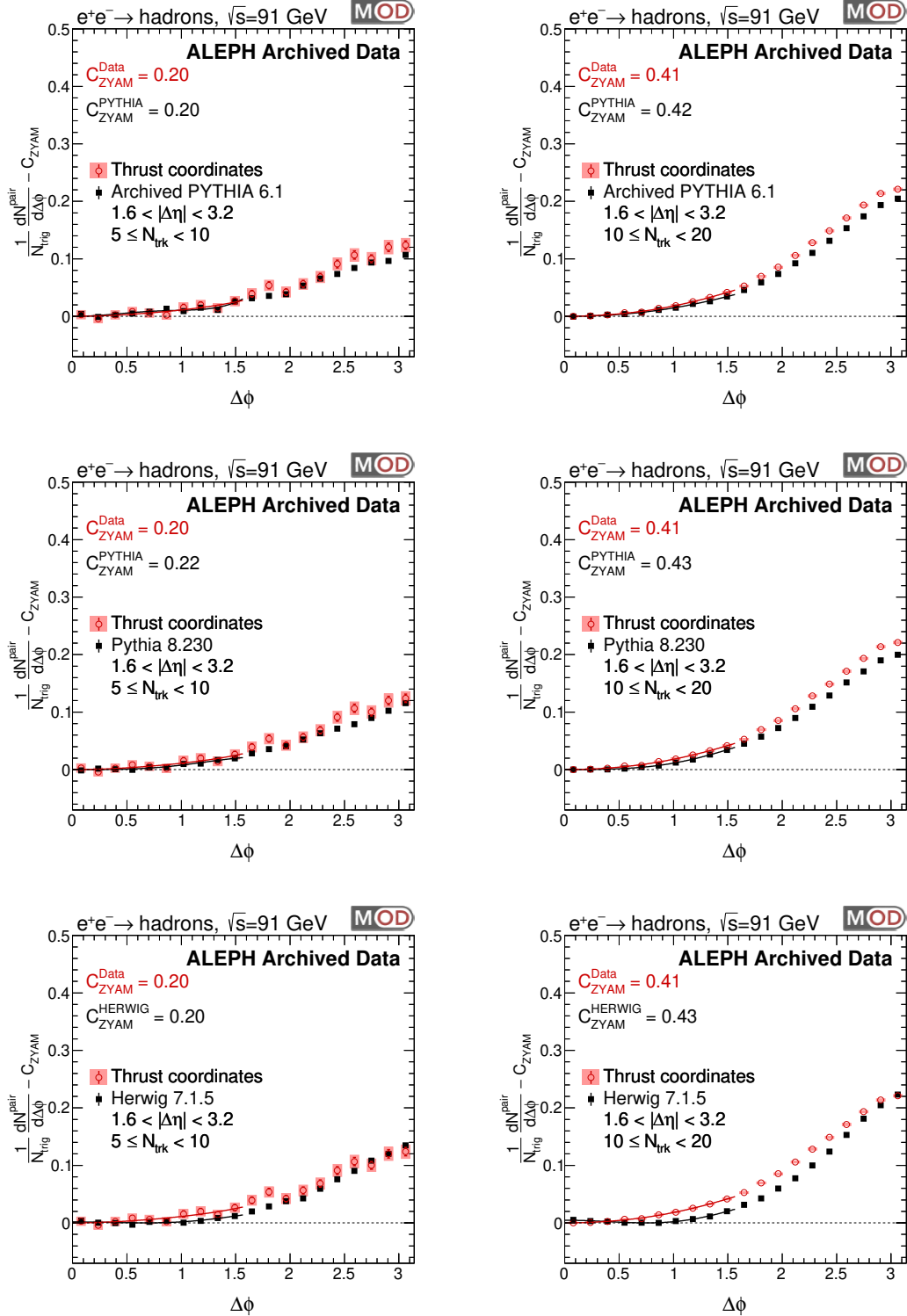
Figure 7-17: The differential yield of charged particle pairs in the pseudorapidity range $1.6 < |\Delta\eta| < 3.2$ after ZYAM subtraction using thrust coordinates for both data (red) and Monte Carlo (black) for $20 \leq N_{trk} < 30$ (left) and $N_{trk} \geq 30$ (right). The rows are ordered by generator level PYTHIA 6.1, PYTHIA 8.230, HERWIG 7.1.5.
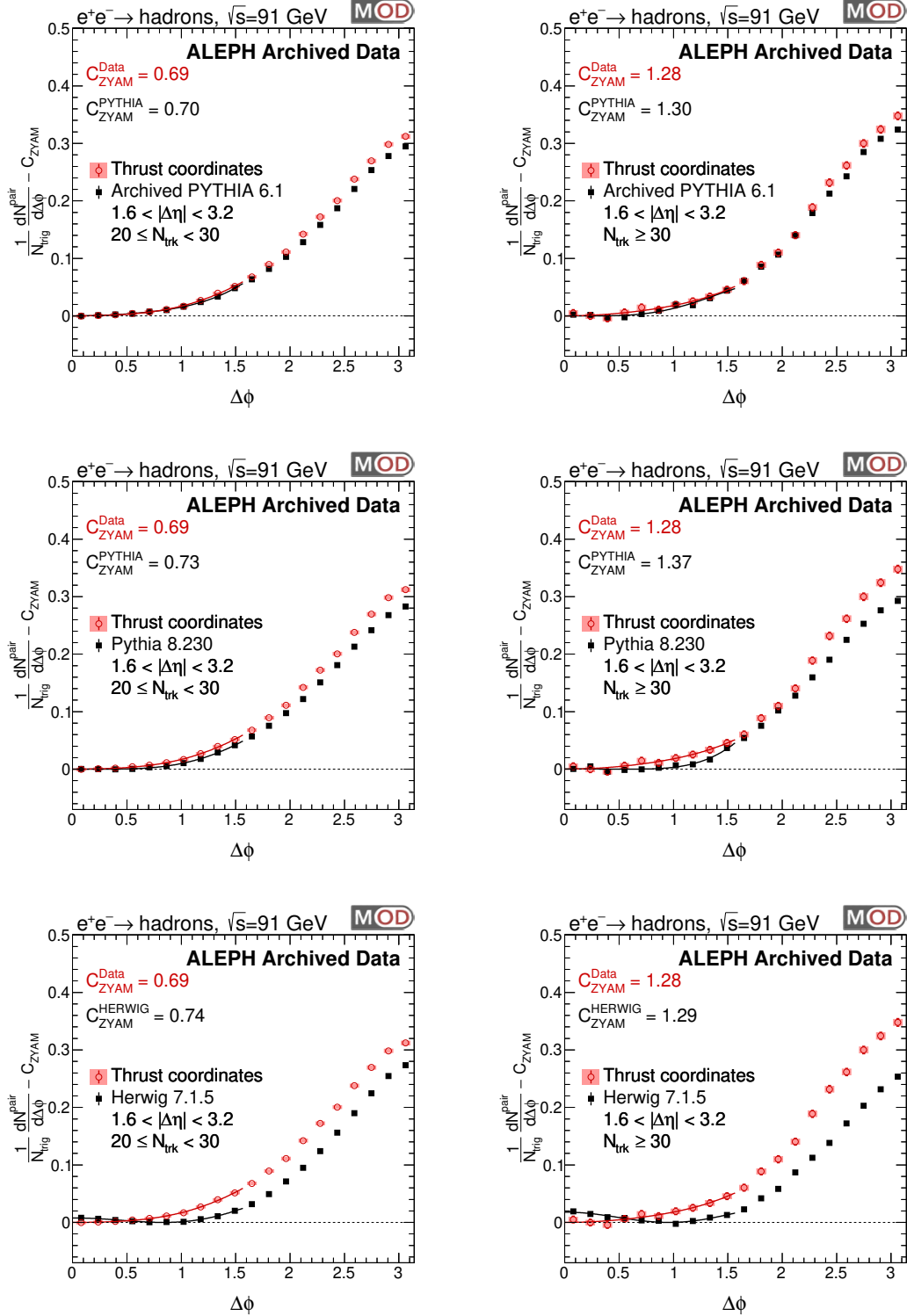
Figure 7-18: The differential yield of charged particle pairs in the pseudorapidity range $1.6 < |\Delta\eta| < 3.2$ after ZYAM subtraction using thrust coordinates for both data (red) and Monte Carlo (black) for $N_{trk} \geq 35$. The figures are ordered by generator level PYTHIA 6.1 (top left), PYTHIA 8.230 (top right), HERWIG 7.1.5 (bottom).
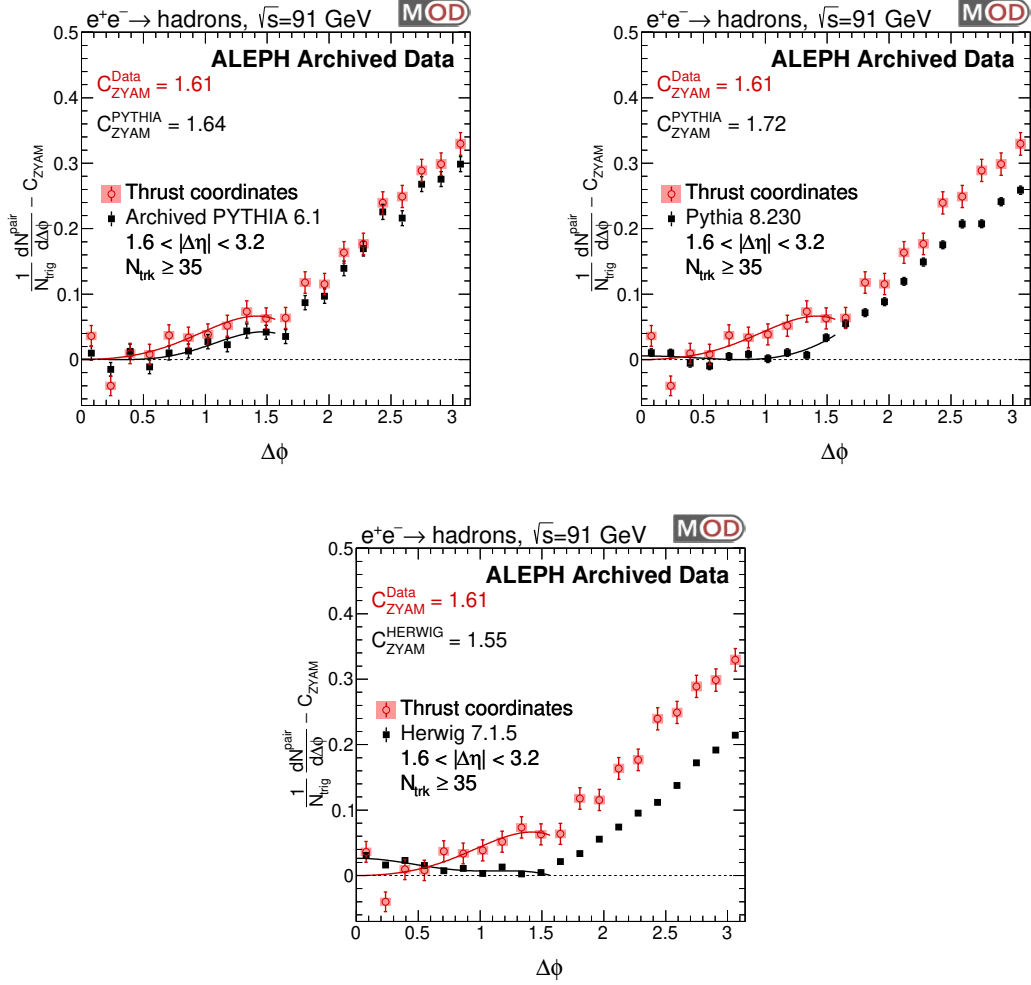
Chapter 8

Study of Geometric Correlations

The intuition that one has for understanding the topology of the correlation function from pp, pA, and AA collisions is misleading for understanding the thrust frame e^+e^- correlation function. Since the coordinate frame is different for each event and is depended on the energy-momentum distribution of the event, one cannot think in terms of defined spatial coordinates. Instead, the correlation functions should be understood in terms of the relationships between the jets. The leading jet in a pencil-like event, for example, will be nearly aligned with the thrust axis and thus its particles can take on any azimuthal value. On the other hand, the azimuthal distribution of an off-axis jet in a three jet event is squeezed into a narrow window. As a result, the correlations that arise between jets is not obvious.

Furthermore, a thorough study of how different final state geometries contribute to the correlation function is critical to discriminating between trivial and non-trivial correlations and understanding how different QCD processes manifest in the topology. For e^+e^- collisions, the two dominant final state geometries are a dijet formed from a $q\bar{q}$ pair and a trijet formed from a $q\bar{q}g$.

To isolate the contribution from these geometries, analysis level cuts on the p_T of the leading, subleading, and sub-subleading jets were applied to generator level PYTHIA 6.1. Jets were clustered using the Cambridge/Aachen algorithm with a cone radius of 0.4 [132]. Dijet event were required to have the ratio of the second to third jet p_T to be at most 0.05. Two cuts that were attempted to isolate three jet events
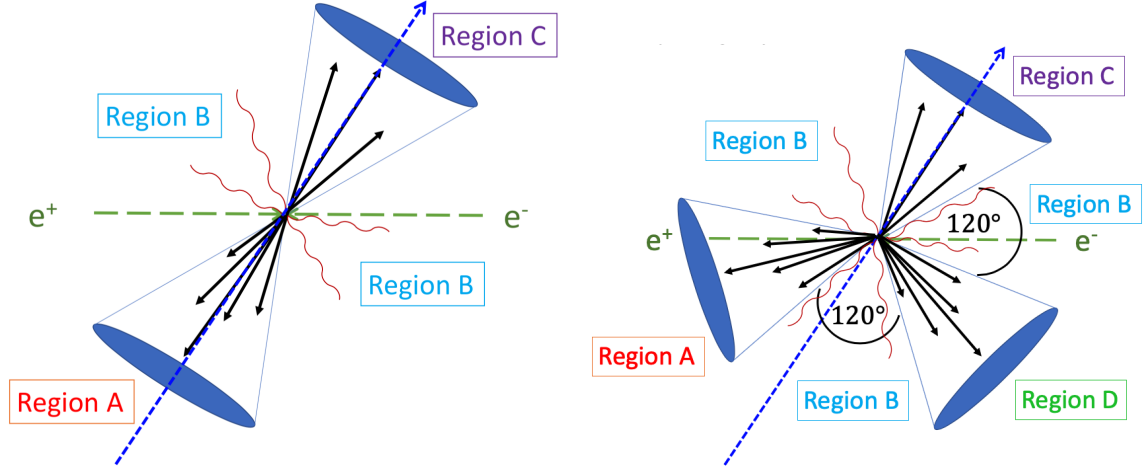
Figure 8-1: The dominant dijet and trijet event shapes for e^+e^- collisions. The geometries are decomposed into regions and two-particle correlations are computed. Observed correlations are solely related to the final state topologies, independent of medium production. This study is crucial to distinguishing trivial from non-trivial correlations.

were that the ratio of the second to third jet p_T be at least 0.5 and the ratio of the third to fourth jet p_T be at most 0.05. The second condition resulted in too small of a sample from the relatively low statistics archived Monte Carlo so only the first one was required, creating a sample of multi-jet events which was largely dominated by three jet events. The effects of higher jet events result in additional understood structure in the correlation function.

Using this construction, dijet events were separated into three regions: inside of the first cone (Region A), inside of neither cone (Region B), and inside of the second cone (Region C). Three jet events were similarly decomposed into four regions by labeling the third jet cone (Region D); see Figure 8-1 for an illustration of the dijet (left) and trijet (right) geometries. The selected events were decomposed into sub-events that contained combinations of the event regions using analysis level ΔR cuts between the selected signal particle and the desired jet axis. Pairs in the signal distribution were formed only between particles in the sub-event. The background distribution of the full event was used for each sub-event so that the normalization was constant and the sub-events could be summed to reconstruct the total event.

8.1 The Dijet Event Shape

8.1.1 Lab Frame

The full dijet correlation function using lab coordinates is shown in Figure 8-2 for events with between ten and twenty tracks post selection. The dominant features are the near side single peak ($\Delta\phi \sim 0$) and the away side double peak ($\Delta\phi \sim \pi$).
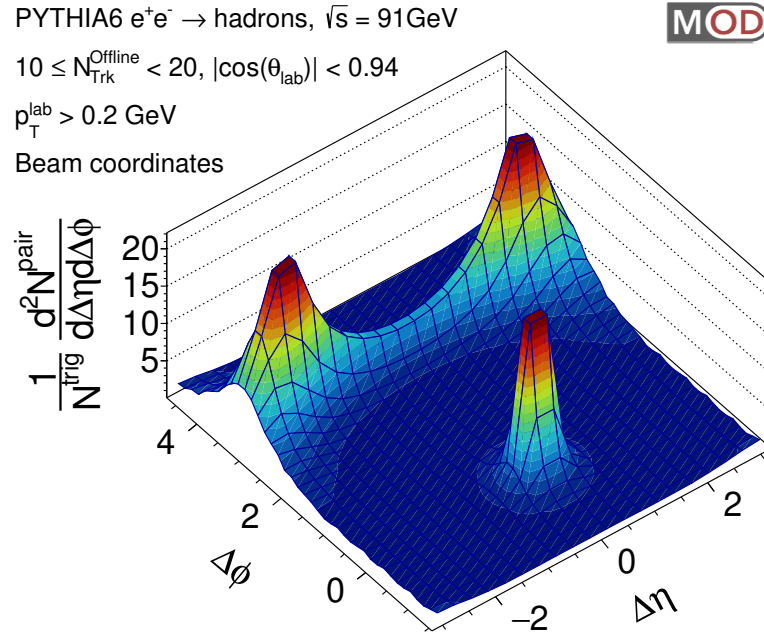
Figure 8-2: The full two-particle correlation function using lab coordinates for dijet events selected using relative jet p_T cuts from PYTHIA 6.1 generated events. Events were selected by requiring that the ratio of the second jet p_T to the third jet p_T be at most 0.05.

The peak at $(0,0)$ arises from particle pairs within the same jet cone (Region A/C with A/C, top). Since the jet cone is not aligned with the beam axis, its azimuthal distribution is squeezed into a narrow window. Particles within the same jet are close in η, thus creating the peak at $(0,0)$. The double peak at $\Delta\phi = \pi$ is created by pairings formed between particles in different jet cones (Region A with C, bottom). The back-to-back jets are required by momentum conservation to be separated by π in azimuth and widely gaped in η. Thus, creating two peaks in the away side.

Figure 8-3: The two-particle correlation function using lab coordinates for dijet events selected using relative jet p_T cuts from PYTHIA 6.1 generated events. Pairings formed between particles in the same jet cone create a localized peak at the origin (top), while pairings formed between particles in different jet cones create a double peak at $\Delta\phi = \pi$ (bottom).

Pairings between particles that are not in either jet cone have a large $\Delta\eta$ gap since they are on opposite sides of the event and $\Delta\phi \sim \pi$ by momentum conservation (Region B with B, top). Similarly, pairings between a particle in the background region and one inside of a jet cone are widely gaped in η since nearby particles are in the same jet cone and therefore cannot be paired up (Region A/C with B). An additional structure around $(0,0)$ comes from background particles that are just outside of the jet cone, which may have been cluster if a large jet cone had been chosen.

Figure 8-4: The two-particle correlation function using lab coordinates for dijet events selected using relative jet p_T cuts from PYTHIA 6.1 generated events. Pairings formed between particles that are in neither jet cone creates a double peak at $\Delta\phi \sim \pi$ (top), while pairings formed between a background particle and a jet cone particle creates a double peak at $\Delta\phi \sim \pi$ and a localized peak with a hole at the origin (bottom).

8.1.2 Thrust Frame

The full dijet correlation function using thrust coordinates is shown in Figure 8-2 for events with between ten and twenty tracks post selection (top). The dominant features are the broad peaks along $\Delta\eta \sim 0$ and $\Delta\phi \sim \pi$. The correlation function looks similar to the inclusive pp correlation function (bottom), but the features arise for very different reasons.
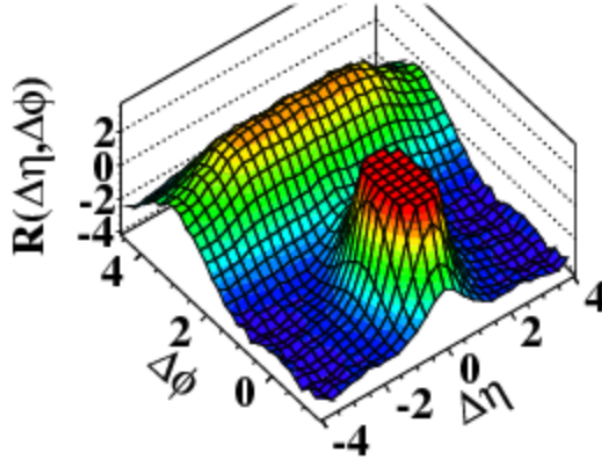
Figure 8-5: The full correlation function using thrust coordinates for dijet events (top). Events were selected from PYTHIA 6.1 generated events by requiring that the ratio of the second jet p_T to the third jet p_T be at most 0.05. The structure is similar to the inclusive pp two particle correlation function [114].

Unlike in the beam analysis, pairings formed between particles from the same jet create an elongated azimuthal peak centered at $\Delta\eta \sim 0$ (Region A/C with A/C, top). Since the cones are approximately aligned with the thrust axis, their particle distributions are roughly uniform in ϕ without rather than squeezed into a narrow region. Pairings formed between particles from different jet cones have a large $\Delta\eta$ and therefore will be mostly not shown in the correlation function (Region A with C, bottom). Some particles that are close to the edges of the cones create a small enhancement, however.
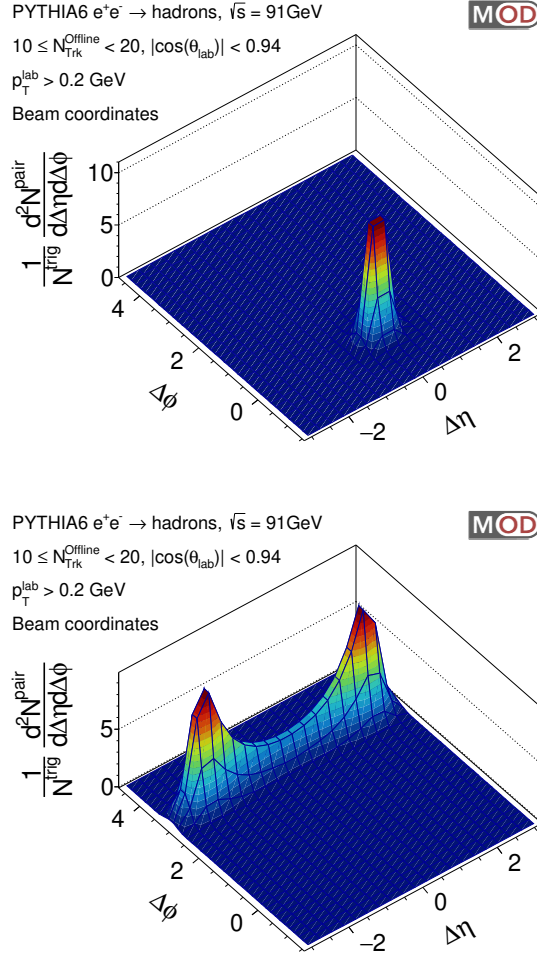

Figure 8-6: The two-particle correlation function using thrust coordinates for dijet events selected using relative jet p_T cuts from PYTHIA 6.1 generated events. Pairings formed between particles in the same jet cone create a localized uniform azimuthal peak centered at $\Delta\eta \sim 0$ (top), while pairings formed between particles in different jet cones are largely outside the $\Delta\eta$ region plotted (bottom).

Pairings between particles that are in the background region create a roughly uniform enhancement in $\Delta\eta$ since soft transverse particles are not preferentially made in η. An additional elongated peak across $\Delta\phi$ that sits atop the pedestal comes from particles that are on the edges of the jet cones and therefore may have been clustered if a larger cone size was used (Region B with B, top). Conversely, pairings formed between a particle in the background and one inside of a jet cone contribute only at large $\Delta\eta$ by construction (Region A/C with B, bottom).
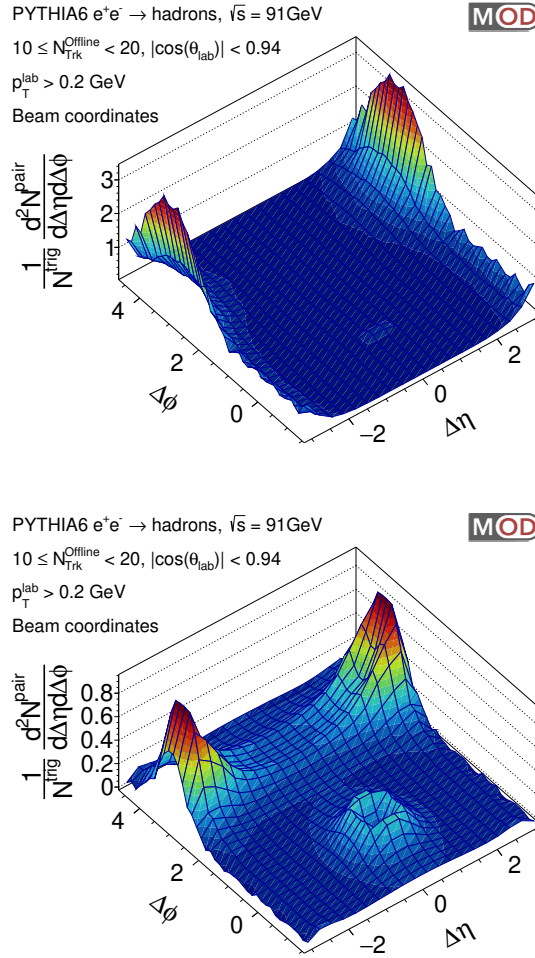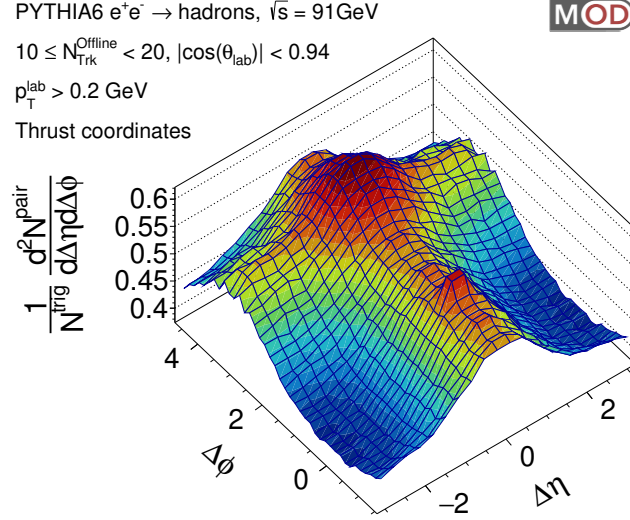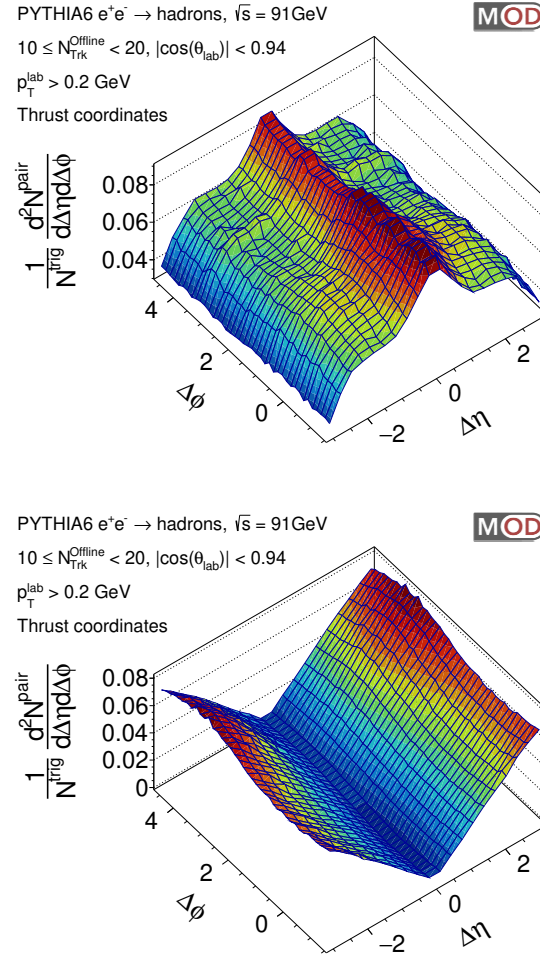

Figure 8-7: The two-particle correlation function using thrust coordinates for dijet events selected using relative jet p_T cuts from PYTHIA 6.1 generated events. Pairings formed between particles that are in neither jet cone creates a broad peak in $\Delta\phi$ above a uniform pedestal (top), while pairings formed between one particle in the background and one that inside of a jet cone create peaks at large $\Delta\eta$ (bottom).

8.2 The Trijet Event Shape

8.2.1 Lab Frame

The full trijet correlation function using lab coordinates is shown in Figure 8-8 for events with between twenty and thirty tracks post selection. The dominant features are the near side single peak ($\Delta\phi \sim 0$) and the away side double peak ($\Delta\phi \sim \pi$). The only structural difference from the corresponding dijet distribution is the relative broadening at small $\Delta\eta$ and $\Delta\phi \sim \pi$. For the sub-event decomposition, the leading and subleading jets are considered independently and then summed.

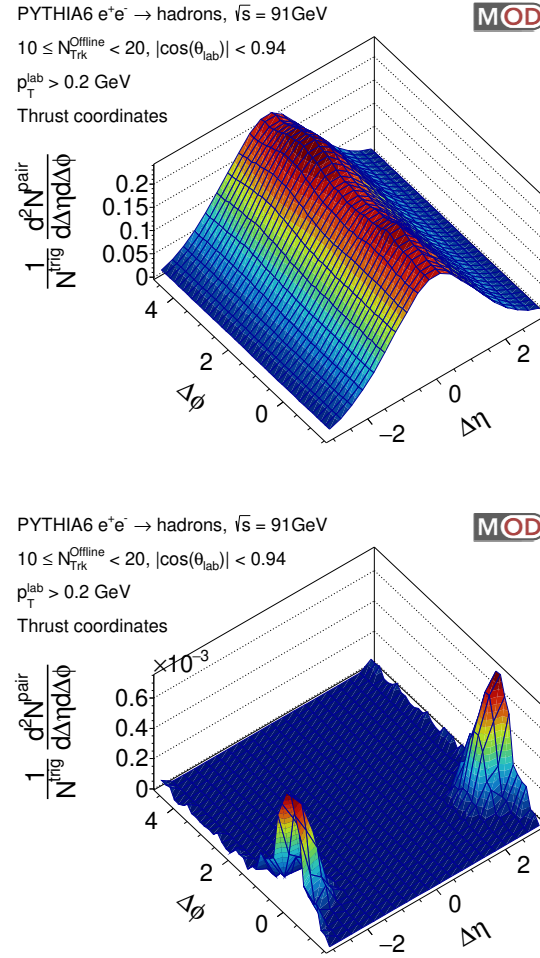Figure 8-8: The full two-particle correlation function using lab coordinates for trijet events selected using relative jet p_T cuts from PYTHIA 6.1 generated events. Events were selected by requiring that the ratio of the second jet p_T to the third jet p_T be at least 0.5 and the ratio of the third to fourth jet p_T to be at most 0.05.

Pairings between leading jet particles and subleading jet particles create the dominate double peak since these jets are required by momentum conservation to be separated by roughly π in azimuth and widely gaped in η (Region A with C/D, top left). A broad structure is also formed in the vicinity of small $\Delta\eta$ since the subleading jets can be largely kinked off axis. Pairings between particles in the subleading jets create an additional structure in the near side with a hole at $(0,0)$ because their ϕ distributions are narrow with respect the beam pipe (Region C with D, top right).

Figure 8-9: Between jet cone sub-events created from trijet events using particle pairings between leading and subleading jet particles (top left) and two subleading jet particles (top right). The sum of the sub-events is also shown (bottom).

Pairings between background particles have a large $\Delta\eta$ gap since they are on opposite sides of the event and a relative peak near $\Delta\phi \sim \pi$ because of momentum conservation (Region B with B).
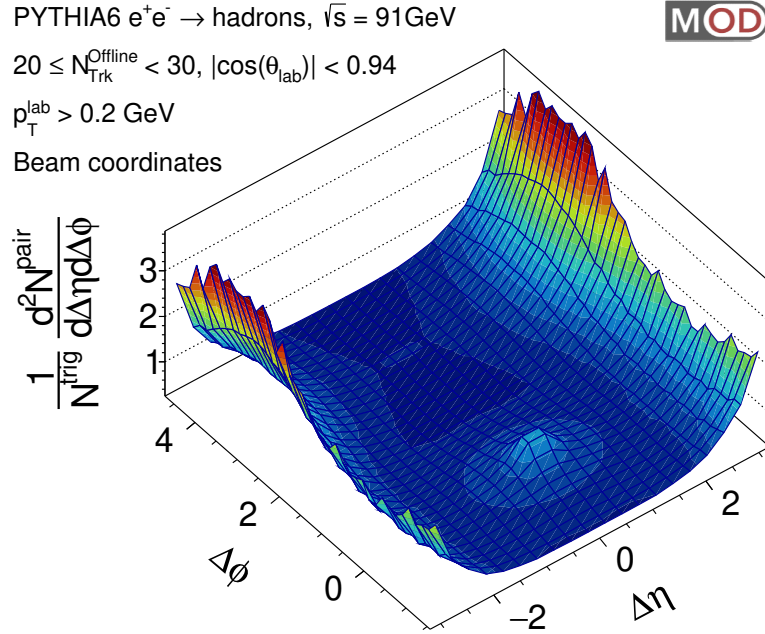
Figure 8-10: Background trijet sub-events created using background particle pairings. Events were selected using relative jet p_T cuts from from PYTHIA 6.1 generated events. The dominant feature is the presence of broad peaks at large $\Delta\eta$.

Pairings between the background region and a single jet cone have large $\Delta\eta$ because nearby particles by construction (Region A/C with B). An additional structure around $(0,0)$ comes from background particles that are just outside of the jet cone, which may have been clustered if a large jet cone was used. Pairings created from leading jet particles (top left) also have a small $\Delta\eta$ structure in the away side, while those created from subleading jet particles do not (top right).
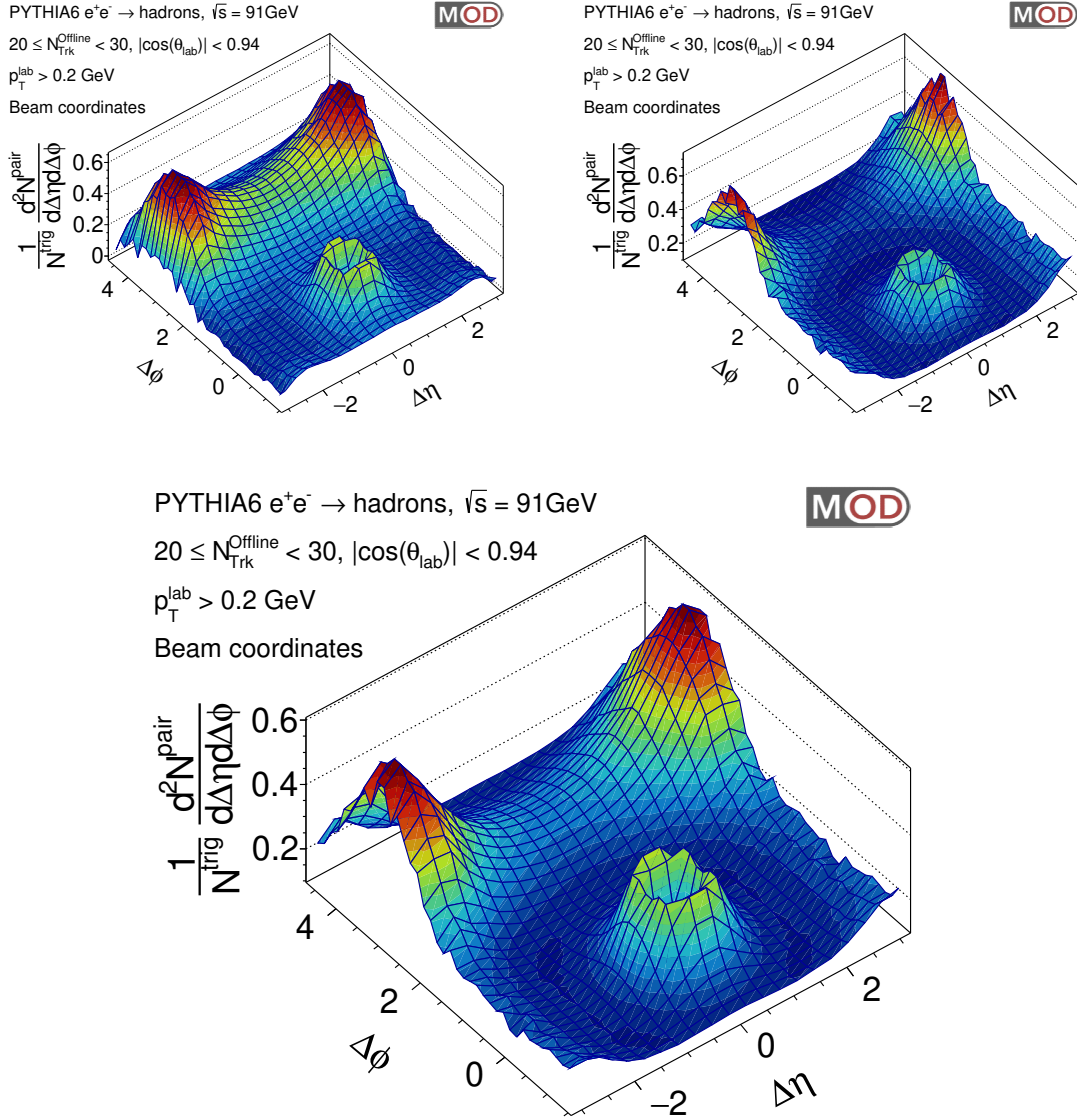
Figure 8-11: Trijet sub-events created using pairings between background and jet particles. Events were selected using relative jet p_T cuts from from PYTHIA 6.1 generated events. The sum of the sub-events is also shown (bottom).

The peak at $(0,0)$ arises from particle pairs within the same jet cone (Region A/C/D with A/C/D). Since none of the jet cones are aligned with the beam axis, their azimuthal distributions are squeezed into a narrow window. Particles within the same jet are close in η, thus creating the peak at $(0,0)$.
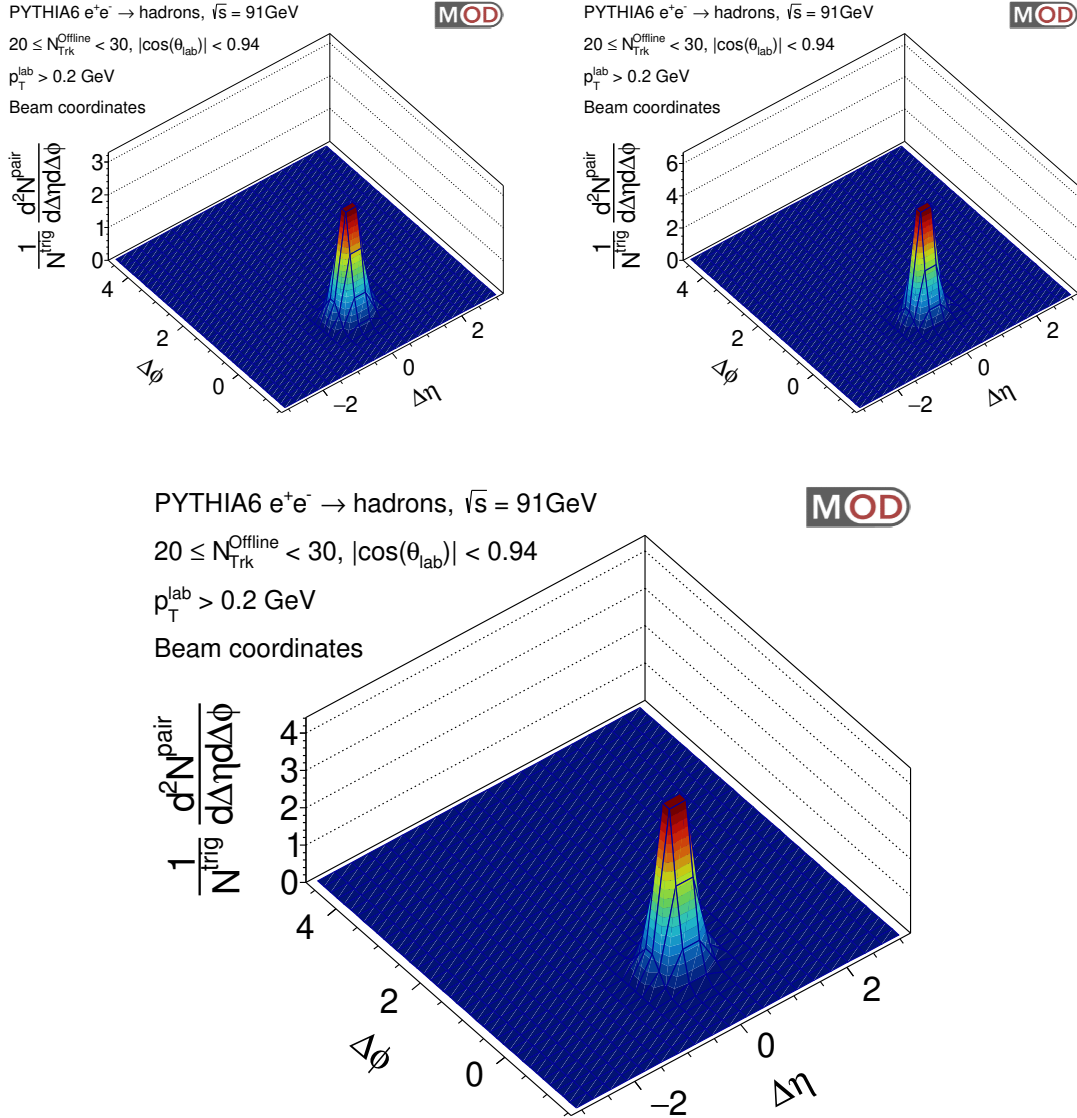
Figure 8-12: Background trijet sub-events created using particle pairings from within the same jet. Events were selected using relative jet p_T cuts from from PYTHIA 6.1 generated events. The contributions from leading (top left) and subleading (top right) are roughly the same. The sum of the sub-events is also shown (bottom).

8.2.2 Thrust Frame

The full trijet correlation function using thrust coordinates is shown in Figure 8-2 for events with between twenty and thirty tracks post selection. This multiplicity range was used so that events to ensure that the thrust value was still relatively high. The dominant features are the two peaks at $\Delta\eta \sim 0$ and the fins at large $\Delta\eta$.
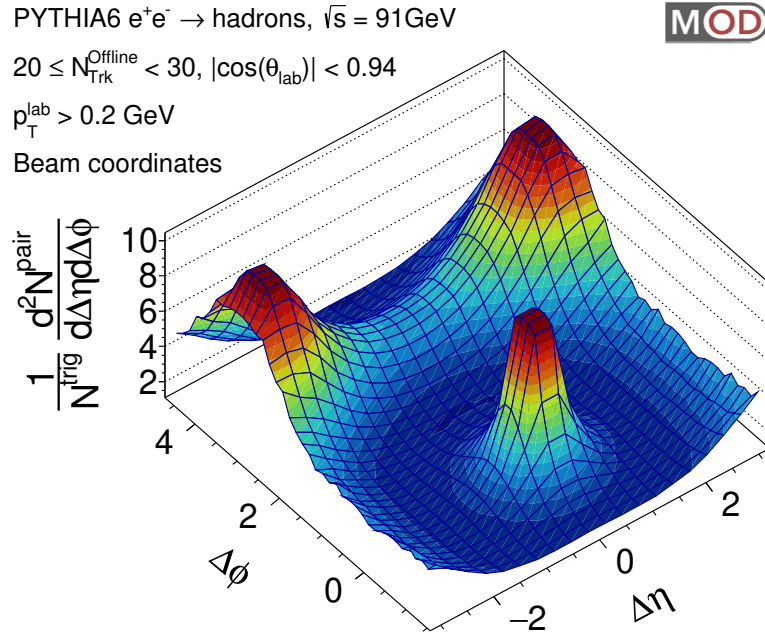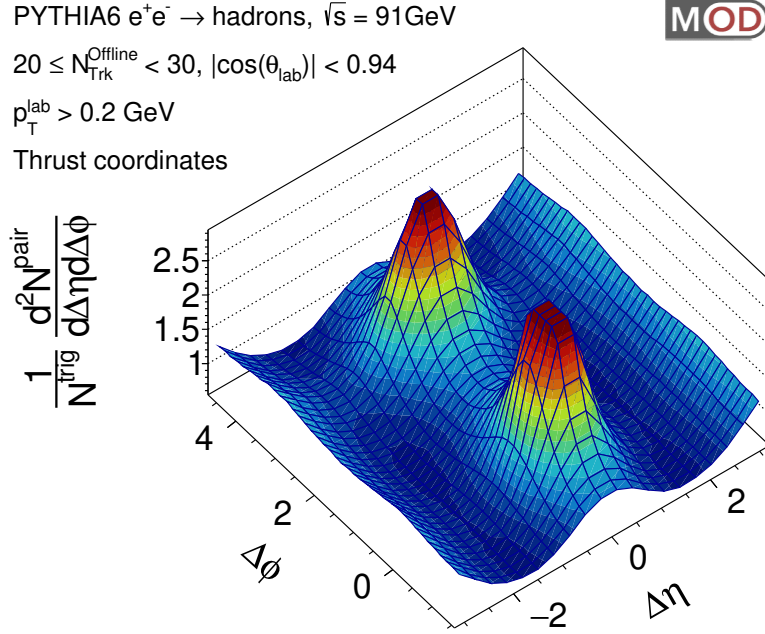

Figure 8-13: The full two-particle correlation function using thrust coordinates for trijet events that were selected using relative jet p_T cuts from PYTHIA 6.1 generated events. Events were selected by requiring that the ratio of the second jet p_T to the third jet p_T be at least 0.5 and the ratio of the third to fourth jet p_T to be at most 0.05.

In a configuration of three jets with high thrust, the leading jet is typically centered on the thrust axis while the subleading jets are split along η and ϕ. The case of particles within the on axis leading jet is therefore different from the case of particles within the subleading jets.
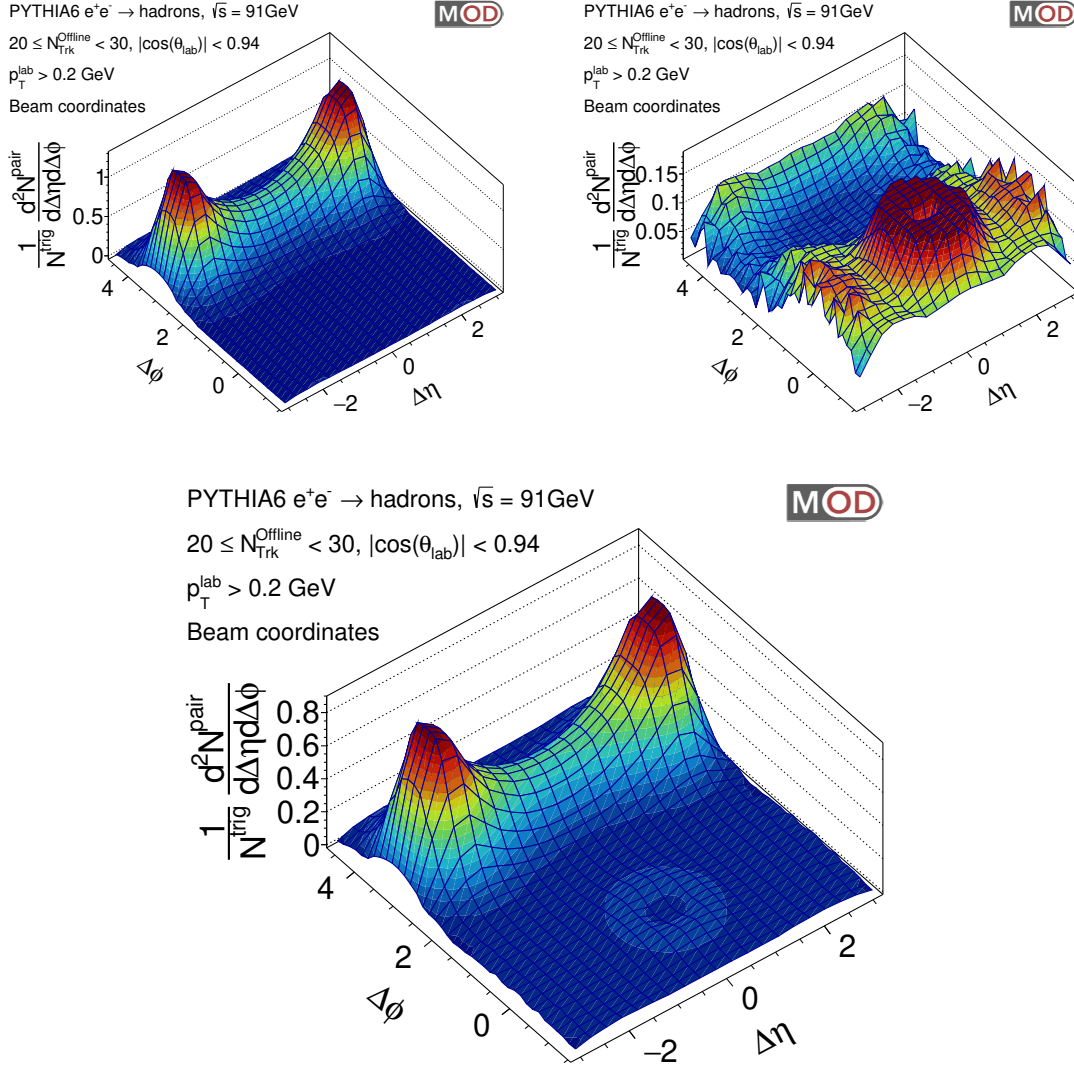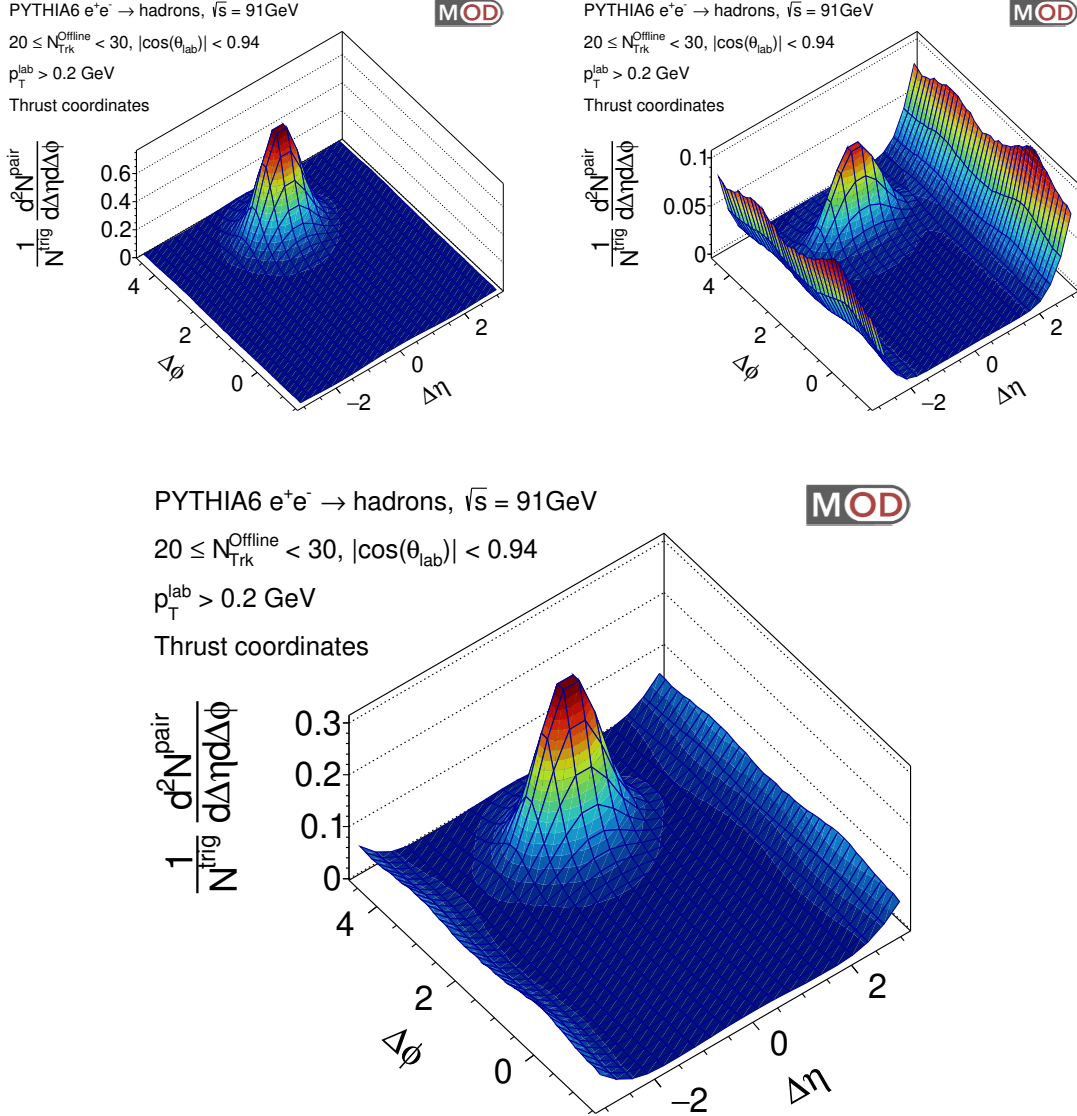

Figure 8-14: Between jet cone sub-events created from trijet events using particle pairings between leading and subleading jet particles (top left) and two subleading jet particles (top right). Events were selected using jet p_T cuts from PYTHIA 6.1 events. The sum of the sub-events is also shown (bottom).

Since the subleading jets must be split along $\Delta\phi$ by momentum conservation,

particle pairs between the jet cones will be separated in azimuth by roughly π. If the subleading jets are not split along η, then particle pairs will have $\Delta\eta \sim 0$. Any splitting between the subleading jets along θ will be removed by the use of η. Therefore, correlations arising from particle pairs formed between the subleading jets are localized around $\Delta\eta \sim 0$ and $\Delta\phi \sim \pi$ (top left).

When one of the subleading jets is replaced by the leading jet (top right), which in most cases is roughly aligned with the z (thrust) axis, particle pairs become widely separated in η and uniformly separated in ϕ (since particle production in a single cone with respect to another cone is uniform in azimuth). If the leading jet is not aligned with the thrust axis, however, then both jets are considered off axis with respect to the z axis, thus a peak at $\Delta\phi \sim \pi$ and $\Delta\eta \sim 0$ will arise for the same reason as in the previous case.

Since there are typically many more particles in the second and third jet combined than in the leading jet alone, the off-off axis contribution to the full correlation function is larger than the on-off axis contribution.

Removing particles from the three leading jet cones defines three background regions between the cones that can be studied. Within one of the regions, many particle pairs arising from soft radiation near the jet cones will be close η and ϕ, creating a localized enhancement in the signal distribution. Pairs constructed within a region from particles originating from different jets, on the other hand, are more widely separated in η, thus creating a uniform-like $\Delta\eta$ distribution. At a particular $\Delta\eta$, the azimuthal distribution of particles from different regions is uniform. Thus, the background regions contribute a uniform-like distribution with a peak at $(\Delta\eta, \Delta\phi) \sim (0,0)$ to the overall correlation function.
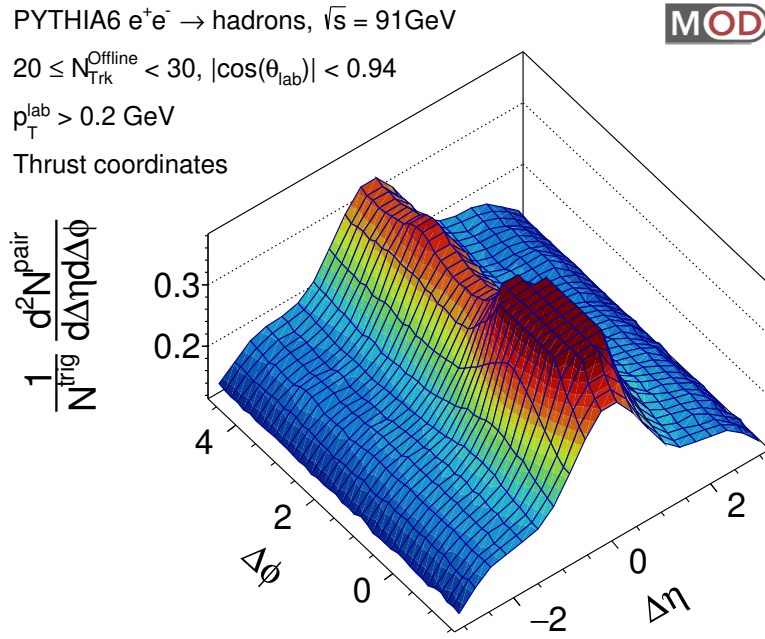
Figure 8-15: Background trijet sub-events created using pairings created from background particles. Events were selected using relative jet p_T cuts from from PYTHIA 6.1 generated events.

The regions outside of the jet cones contain particles arising from soft radiation transverse to the original color string in addition to particles just outside of the defined jet cone. Correlations between background particles and particles within a jet cone therefore measure two primary effects: QCD induced radiation and experimental choice of jet cone size. Since all three jets are partially excluded in each calculation of the signal distribution, the constructed correlations exhibit holes in ϕ and η.
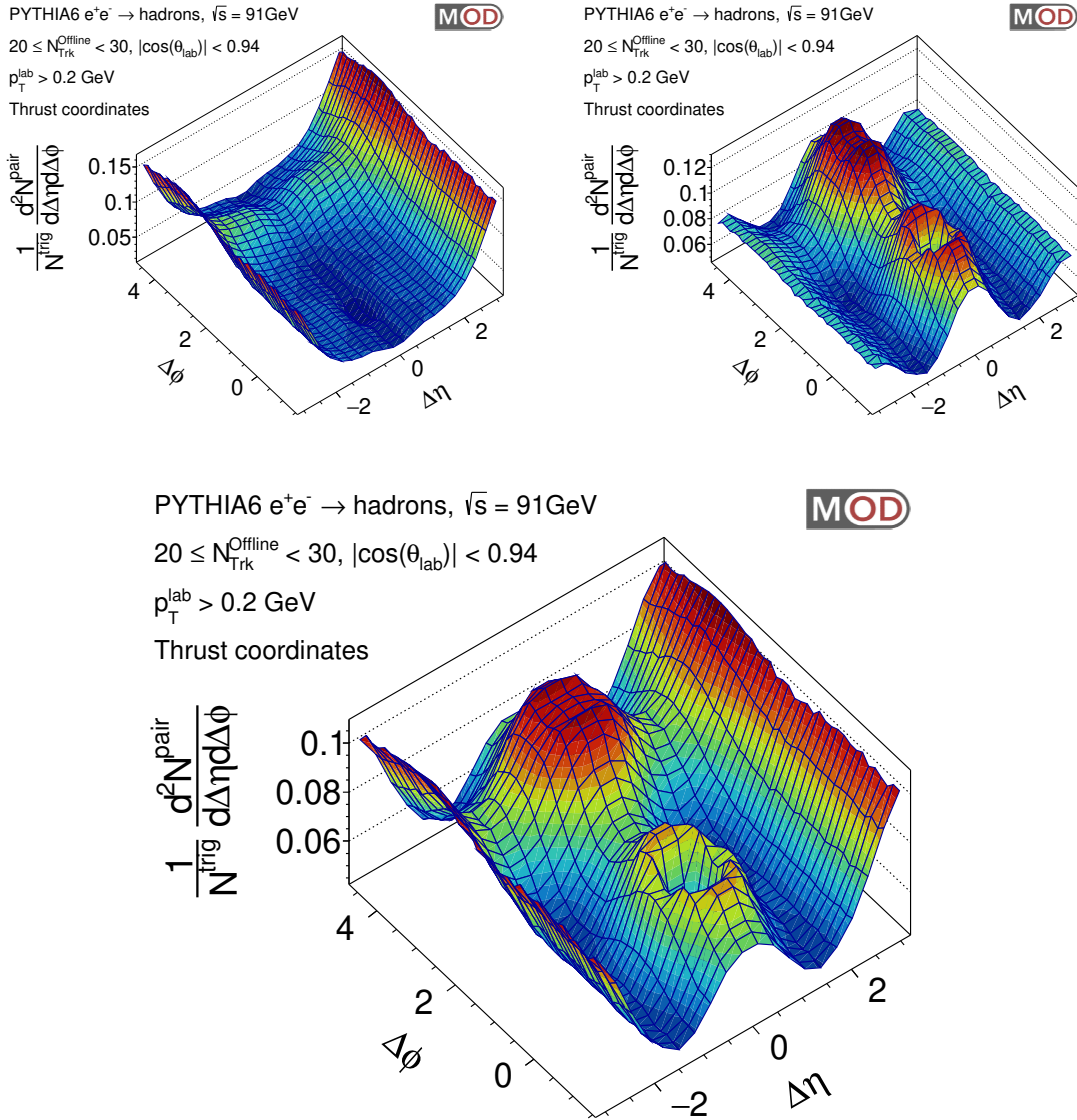
Figure 8-16: Trijet sub-events created using pairings between background and off-axis (top left) and on-axis (top right) jet particles. The sum of the sub-events is also shown (bottom).

Moreover, the leading and subleading jets need to be considered independently because particles in the leading jet have access to all values of ϕ while those in the subleading jets are contained in relatively narrow regions. In either case, the azimuthal production of particles widely separated in η is isotropic because those particles necessarily originate from different partons. For pairings with the on axis jet (top left), an additional normally distributed enhancement arises at $\Delta\phi \sim \pi$ from background particles originating in either of the subleading jets. An azimuthally extended hole at $\Delta\eta \sim 0$ arises because both particles cannot be selected from the on axis jet.

Conversely, pairings with off axis jet particles (top right) give rise to an azimuthally extended enhancement at $\Delta\eta \sim 0$ with a tight hole localized at $\Delta\phi \sim 0$ since pairings are not formed within the cones but at momentum conservation dictates that soft particles be created from the subleading jets roughly separated uniformly in azimuth. An additional enhancement arises in the away side for the same reason that soft radiation not contained in the jet cone must be balanced in azimuth which happens if many are separated by π. For pairings with the on axis jet, an additional normally distributed enhancement arises at $\Delta\phi \sim \pi$ from background particles originating in either of the subleading jets. An azimuthally extended hole at $\Delta\eta \sim 0$ arises because both particles cannot be selected from the on axis jet.

Within a jet cone, particles are narrowly separated in η. Particles in the off axis jets are narrowly separated in ϕ because the azimuthal production region is squeezed (top left). Particles in the on axis jet are not since the z axis runs roughly through their jet core (top right). An additional enhancement is localized at $\Delta\eta \sim 0$ because many particles within the leading cone are close in η.
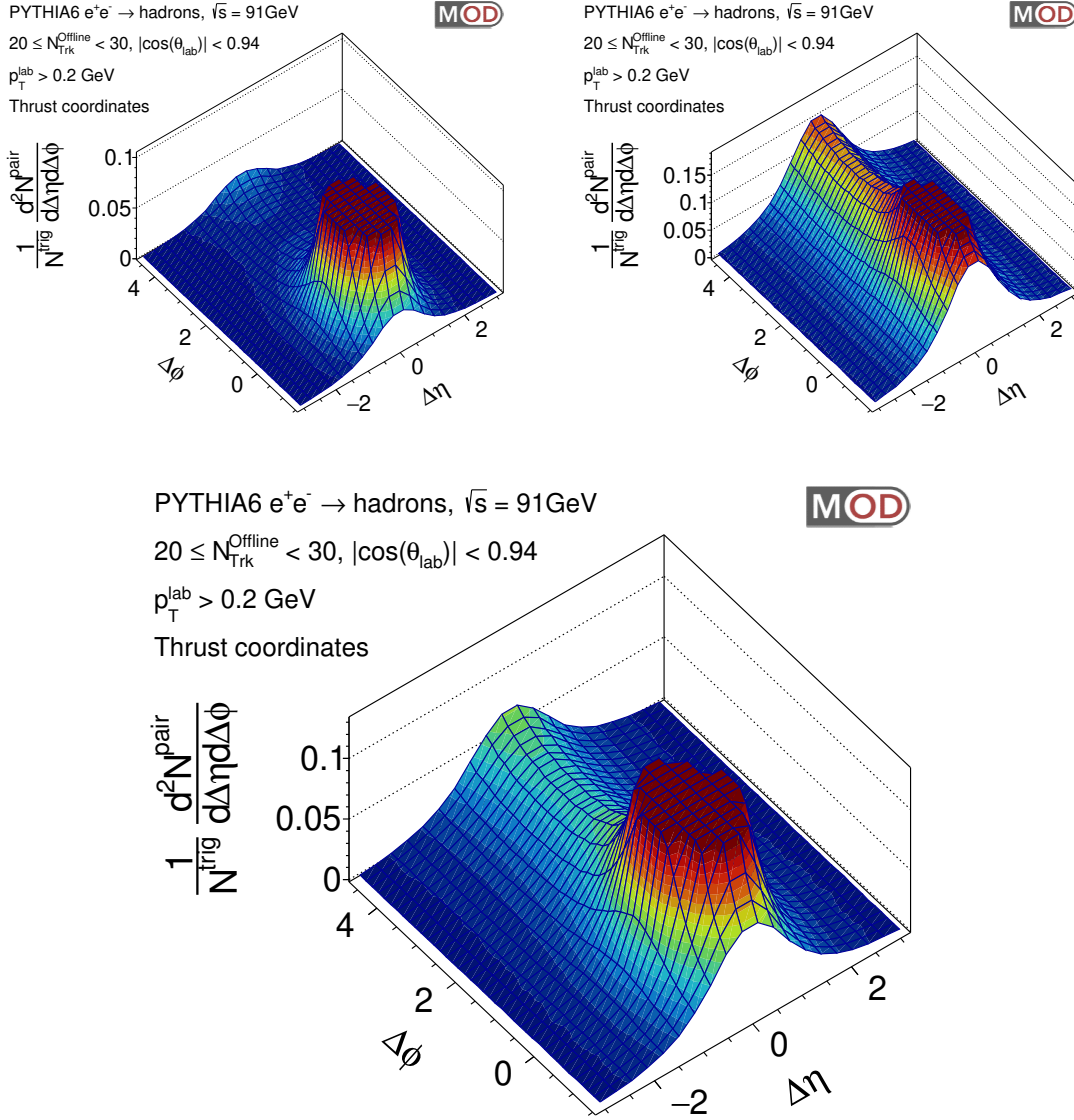
Figure 8-17: Trijet sub-events created from pairings of particles from within the same jet cone; off-axis (top left) and on-axis (top right) correlations are different because of the contraction of the ϕ distribution. The sum of the sub-events is also shown (bottom).

8.3 Summary

The decomposition shown is just one possible way to study the topology of the correlation function. A more detailed study could be done that varies the clustering algorithm, jet cone size, p_T cuts, and event generator. Nevertheless, the decomposition shown was sufficient for understanding the qualitative structure of the two-particle correlation functions shown in Chapter 7. The most important take away should be that the thrust axis correlations are non-trivial and that the intuition that one has from previous correlation analysis should not be directly applied. Instead, one should think in terms of the relationship between the jet cones and the thrust axis.

Chapter 9

Conclusion

As stated in Section 2.5, this thesis aimed to answer two fundamental questions: is flow observed in e^+e^- collisions and should e^+e^- collisions be used as the reference for larger systems? The measurements presented showed that long-range angular correlations were not observed in e^+e^- collisions from the viewpoint of either the lab frame or the thrust frame. The deployed coordinates were sensitive to expansive effects transverse to the beam axis and the color string connecting the $q\bar{q}$ pair, respectively. Upper limits on the associated yield for five multiplicity bins were found using a bootstrapping procedure to be in agreement with this conclusion. Therefore, flow is not observed in e^+e^- collisions for the probed kinematic range of $\sqrt{s} = 91$ GeV. Flow may, however, still exist in higher energy collisions, in which greater multiplicities are accessible.

Nevertheless, e^+e^- is the first system to absent any signal of QGP. Measurements that need a reference, such as jet quenching, should utilize a system in which no flow is observed rather than one in which some flow is observed, such as pp. A true reference should, however, also match the energy scale accessible by modern colliders. Therefore, a new program for high energy e^+e^- (or more likely $\mu^+\mu^-$) collisions is necessary. There is already work being done towards this goal by the organizing committees of the Electron-Ion, International Linear, and Future Circular Colliders, which will enable searches for flow at higher energy scales as well as other new physics. By changing the reference to e^+e^-, new and more detailed studies of the signals seen

in pp collisions will be possible, providing new insight for the development of a unified picture of QGP production in systems of all sizes.

Parallel to this work, the archived e^+e^- open data can also be used for new studies in jet structure observables such as jet shape, splitting functions, and jet fragmentation functions. Such measurements can not only be used as a reference for pp, pA, and AA collisions using modern jet reconstruction algorithms, but also to constrain theoretical models by extending those measurements vs. event multiplicity or number of reconstructed jets. Ultimately, this thesis serves as a stepping stone to future analysis using the archived e^+e^- data, which will deepen our understanding of the fundamental properties of QCD, and a bridge between the fields of heavy ion physics and fundamental particle physics.

Bibliography

[1] G. Roland, K. Safarik, and P. Steinberg, "Heavy-ion collisions at the LHC", *Prog. Part. Nucl. Phys.* **77** (2014) 70–127, `doi:10.1016/j.ppnp.2014.05.001`.

[2] S. Ozaki, "The Relativistic heavy ion collider at Brookhaven", *Nucl. Phys.* **A525** (1991) 125C–132C, `doi:10.1016/0375-9474(91)90320-6`. [Conf. Proc.C900802V2,C900802V2:1106(1990)].

[3] CMS Collaboration, "Measurement of long-range near-side two-particle angular correlations in pp collisions at $\sqrt{s}$ =13 TeV", *Phys. Rev. Lett.* **116** (2016), no. 17, 172302, `doi:10.1103/PhysRevLett.116.172302`, `arXiv:1510.03068`.

[4] G. Cowan, "Review of particle physics", *Phys. Rev. D* **86** (2012), no. 010001, 390.

[5] P. W. Higgs, "Broken symmetries and the masses of gauge bosons", *Phys. Rev. Lett.* **13** (Oct, 1964) 508–509, `doi:10.1103/PhysRevLett.13.508`.

[6] S. Weinberg, "Implications of Dynamical Symmetry Breaking", *Phys. Rev.* **D13** (1976) 974–996, `doi:10.1103/PhysRevD.19.1277,10.1103/PhysRevD.13.974`. [Addendum: Phys. Rev.D19,1277(1979)].

[7] A. Pich, "The Standard model of electroweak interactions", in *2004 European School of High-Energy Physics, Sant Feliu de Guixols, Spain, 30 May - 12 June 2004*, pp. 1–48. 2005. `arXiv:hep-ph/0502010`.

[8] S. Weinberg, "A model of leptons", *Phys. Rev. Lett.* **19** (Nov, 1967) 1264–1266, `doi:10.1103/PhysRevLett.19.1264`.

[9] E. Fermi, "Versuch einer Theorie der β-Strahlen. I", *Zeitschrift fur Physik* **88** (March, 1934) 161–177, `doi:10.1007/BF01351864`.

[10] UA1 Collaboration, "Experimental Observation of Isolated Large Transverse Energy Electrons with Associated Missing Energy at s**(1/2) = 540-GeV", *Phys. Lett.* **B122** (1983) 103–116, `doi:10.1016/0370-2693(83)91177-2`. [,611(1983)].

[11] UA2 Collaboration, "Evidence for Z0 —> e+ e- at the CERN anti-p p Collider", *Phys. Lett.* **B129** (1983) 130–140, `doi:10.1016/0370-2693(83)90744-X`. [,7.69(1983)].

[12] K. Kumericki, "Feynman Diagrams for Beginners", 2016. `arXiv:1602.04182`.

[13] F. Wilczek, "QCD made simple", *Phys. Today* **53N8** (2000) 22–28, `doi:10.1063/1.1310117`.

[14] Institute for Theoretical Physics and Astrophysics WÃijrzburg University Collaboration, "Feynman Diagrams For Pedestrians",.

[15] Particle Data Group Collaboration, "Review of Particle Physics", *Chin. Phys.* **C40** (2016), no. 10, 100001, `doi:10.1088/1674-1137/40/10/100001`.

[16] L3 Collaboration, "Measurement of the running of the electromagnetic coupling at large momentum-transfer at LEP", *Phys. Lett.* **B623** (2005) 26–36, `doi:10.1016/j.physletb.2005.07.052`, `arXiv:hep-ex/0507078`.

[17] F. Wilczek, "Nobel lecture: Asymptotic freedom: From paradox to paradigm", *Rev. Mod. Phys.* **77** (Sep, 2005) 857–870, `doi:10.1103/RevModPhys.77.857`.

[18] B. Andersson, G. Gustafson, G. Ingelman, and T. Sjostrand, "Parton Fragmentation and String Dynamics", *Phys. Rept.* **97** (1983) 31–145, `doi:10.1016/0370-1573(83)90080-7`.

[19] user154997, "Quark jet color". Physics Stack Exchange. `https://physics.stackexchange.com/q/359936`.

[20] Z. Nagy, "Next-to-leading order calculation of three jet observables in hadron hadron collision", *Phys. Rev.* **D68** (2003) 094002, `doi:10.1103/PhysRevD.68.094002`, `arXiv:hep-ph/0307268`.

[21] W. Busza, K. Rajagopal, and W. van der Schee, "Heavy Ion Collisions: The Big Picture, and the Big Questions", *Ann. Rev. Nucl. Part. Sci.* **68** (2018) 339–376, `doi:10.1146/annurev-nucl-101917-020852`, `arXiv:1802.04801`.

[22] M. G. Alford, A. Schmitt, K. Rajagopal, and T. SchÃďfer, "Color superconductivity in dense quark matter", *Rev. Mod. Phys.* **80** (2008) 1455–1515, `doi:10.1103/RevModPhys.80.1455`, `arXiv:0709.4635`.

[23] J. Benecke, T. T. Chou, C.-N. Yang, and E. Yen, "Hypothesis of Limiting Fragmentation in High-Energy Collisions", *Phys. Rev.* **188** (1969) 2159–2169, `doi:10.1103/PhysRev.188.2159`.

[24] PHOBOS Collaboration, "Centrality and energy dependence of charged-particle multiplicities in heavy ion collisions in the context of elementary reactions", *Phys. Rev.* **C74** (2006) 021902, `doi:10.1103/PhysRevC.74.021902`.

[25] M. Batista and R. J. M. Covolan, "Leading particle effect, inelasticity and the connection between average multiplicities in e+ e- and p p processes", *Phys. Rev.* **D59** (1999) 054006, `doi:10.1103/PhysRevD.59.054006`, `arXiv:hep-ph/9811425`.

[26] W. Busza, "Extended Longitudinal Scaling: Direct evidence of saturation", *Nucl. Phys.* **A854** (2011) 57–63, `doi:10.1016/j.nuclphysa.2010.12.015`, `arXiv:1102.3921`.

[27] F. Gelis, "Color Glass Condensate and Glasma", *Int. J. Mod. Phys.* **A28** (2013) 1330001, `doi:10.1142/S0217751X13300019`, `arXiv:1211.3327`.

[28] P. Steinberg, "Bulk dynamics in heavy ion collisions", *Nucl. Phys.* **A752** (2005) 423–432, `doi:10.1016/j.nuclphysa.2005.02.139`, `arXiv:nucl-ex/0412009`.

[29] BRAHMS Collaboration, "Quark gluon plasma and color glass condensate at RHIC? The Perspective from the BRAHMS experiment", *Nucl. Phys.* **A757** (2005) 1–27, `doi:10.1016/j.nuclphysa.2005.02.130`, `arXiv:nucl-ex/0410020`.

[30] W. Cassing and E. L. Bratkovskaya, "Hadronic and electromagnetic probes of hot and dense nuclear matter", *Phys. Rept.* **308** (1999) 65–233, `doi:10.1016/S0370-1573(98)00028-3`.

[31] H. Stoecker, "Collective flow signals the quark gluon plasma", *Nucl. Phys.* **A750** (2005) 121–147, `doi:10.1016/j.nuclphysa.2004.12.074`, `arXiv:nucl-th/0406018`.

[32] H. van Hees, V. Greco, and R. Rapp, "Heavy-quark probes of the quark-gluon plasma at RHIC", *Phys. Rev.* **C73** (2006) 034913, `doi:10.1103/PhysRevC.73.034913`, `arXiv:nucl-th/0508055`.

[33] E. V. Shuryak, "Quantum Chromodynamics and the Theory of Superdense Matter", *Phys. Rept.* **61** (1980) 71–158, `doi:10.1016/0370-1573(80)90105-2`.

[34] B. B. Back et al., "The PHOBOS perspective on discoveries at RHIC", *Nucl. Phys.* **A757** (2005) 28–101, `doi:10.1016/j.nuclphysa.2005.03.084`, `arXiv:nucl-ex/0410022`.

[35] PHENIX Collaboration, "Formation of dense partonic matter in relativistic nucleus-nucleus collisions at RHIC: Experimental evaluation by the PHENIX collaboration", *Nucl. Phys.* **A757** (2005) 184–283, `doi:10.1016/j.nuclphysa.2005.03.086`, `arXiv:nucl-ex/0410003`.

[36] STAR Collaboration, "Experimental and theoretical challenges in the search for the quark gluon plasma: The STAR Collaboration's critical assessment of

the evidence from RHIC collisions", *Nucl. Phys.* **A757** (2005) 102–183,
`doi:10.1016/j.nuclphysa.2005.03.085`, `arXiv:nucl-ex/0501009`.

[37] L. Evans and P. Bryant, "LHC Machine", *JINST* **3** (2008) S08001,
`doi:10.1088/1748-0221/3/08/S08001`.

[38] J. Pumplin et al., "New generation of parton distributions with uncertainties
from global QCD analysis", *JHEP* **07** (2002) 012,
`doi:10.1088/1126-6708/2002/07/012`, `arXiv:hep-ph/0201195`.

[39] R. P. Feynman, "Very high-energy collisions of hadrons", *Phys. Rev. Lett.* **23**
(1969) 1415–1417, `doi:10.1103/PhysRevLett.23.1415`. [,494(1969)].

[40] T. Matsui and H. Satz, "J/ÏĹ suppression by quark-gluon plasma formation",
Physics Letters B **178** (1986), no. 4, 416 – 422,
`doi:https://doi.org/10.1016/0370-2693(86)91404-8`.

[41] PHENIX Collaboration, "J/ψ suppression at forward rapidity in Au+Au
collisions at $\sqrt{s_{NN}} = 200$ GeV", *Phys. Rev.* **C84** (2011) 054912,
`doi:10.1103/PhysRevC.84.054912`, `arXiv:1103.6269`.

[42] PHENIX Collaboration, "J/ψ Production vs Centrality, Transverse
Momentum, and Rapidity in Au+Au Collisions at $\sqrt{s_{NN}} = 200$ GeV", *Phys.
Rev. Lett.* **98** (2007) 232301, `doi:10.1103/PhysRevLett.98.232301`,
`arXiv:nucl-ex/0611020`.

[43] CMS Collaboration, "Suppression of non-prompt J/ψ, prompt J/ψ, and
Y(1S) in PbPb collisions at $\sqrt{s_{NN}} = 2.76$ TeV", *JHEP* **05** (2012) 063,
`doi:10.1007/JHEP05(2012)063`, `arXiv:1201.5069`.

[44] ALICE Collaboration, "Centrality, rapidity and transverse momentum
dependence of J/ψ suppression in Pb-Pb collisions at $\sqrt{s_{NN}}$=2.76 TeV", *Phys.
Lett.* **B734** (2014) 314–327, `doi:10.1016/j.physletb.2014.05.064`,
`arXiv:1311.0214`.

[45] ALICE Collaboration, "J/ψ production and nuclear effects in p-Pb collisions
at $\sqrt{S_{NN}} = 5.02$ TeV", *JHEP* **02** (2014) 073,
`doi:10.1007/JHEP02(2014)073`, `arXiv:1308.6726`.

[46] ATLAS Collaboration, "Measurement of the centrality dependence of J/ÏĹ
yields and observation of Z production in leadâĂŞlead collisions with the
ATLAS detector at the LHC", *Phys. Lett.* **B697** (2011) 294–312,
`doi:10.1016/j.physletb.2011.02.006`, `arXiv:1012.5419`.

[47] ALICE Collaboration, "Enhanced production of multi-strange hadrons in
high-multiplicity proton-proton collisions", *Nature Phys.* **13** (2017) 535–539,
`doi:10.1038/nphys4111`, `arXiv:1606.07424`.

[48] P. Koch, J. Rafelski, and W. Greiner, "Strange hadron in hot nuclear matter", *Phys. Lett.* **123B** (1983) 151–154, `doi:10.1016/0370-2693(83)90411-2`.

[49] P. Koch, B. Muller, and J. Rafelski, "Strangeness in Relativistic Heavy Ion Collisions", *Phys. Rept.* **142** (1986) 167–262, `doi:10.1016/0370-1573(86)90096-7`.

[50] WA97 Collaboration, "Strangeness enhancement at mid-rapidity in Pb Pb collisions at 158-A-GeV/c", *Phys. Lett.* **B449** (1999) 401–406, `doi:10.1016/S0370-2693(99)00140-9`.

[51] G.-Y. Qin and X.-N. Wang, "Jet quenching in high-energy heavy-ion collisions", *Int. J. Mod. Phys.* **E24** (2015), no. 11, 1530014, `doi:10.1142/S0218301315300143,10.1142/9789814663717_0007`, `arXiv:1511.00790`. [,309(2016)].

[52] J. D. Bjorken, "Energy Loss of Energetic Partons in Quark - Gluon Plasma: Possible Extinction of High p(t) Jets in Hadron - Hadron Collisions",.

[53] D. d'Enterria, "Jet quenching", *Landolt-Bornstein* **23** (2010) 471, `doi:10.1007/978-3-642-01539-7_16`, `arXiv:0902.2011`.

[54] M. L. Miller, K. Reygers, S. J. Sanders, and P. Steinberg, "Glauber modeling in high energy nuclear collisions", *Ann. Rev. Nucl. Part. Sci.* **57** (2007) 205–243, `doi:10.1146/annurev.nucl.57.090506.123020`, `arXiv:nucl-ex/0701025`.

[55] CMS Collaboration, "Charged-particle nuclear modification factors in PbPb and pPb collisions at $\sqrt{s_{NN}} = 5.02$ TeV", *JHEP* **04** (2017) 039, `doi:10.1007/JHEP04(2017)039`, `arXiv:1611.01664`.

[56] CMS Collaboration, "Observation and studies of jet quenching in PbPb collisions at nucleon-nucleon center-of-mass energy = 2.76 TeV", *Phys. Rev.* **C84** (2011) 024906, `doi:10.1103/PhysRevC.84.024906`, `arXiv:1102.1957`.

[57] D. A. Appel, "Jets as a probe of quark-gluon plasmas", *Phys. Rev. D* **33** (Feb, 1986) 717–722, `doi:10.1103/PhysRevD.33.717`.

[58] J. P. Blaizot and L. D. McLerran, "Jets in expanding quark-gluon plasmas", *Phys. Rev. D* **34** (Nov, 1986) 2739–2745, `doi:10.1103/PhysRevD.34.2739`.

[59] J. Casalderrey-Solana and C. A. Salgado, "Introductory lectures on jet quenching in heavy ion collisions", *Acta Phys. Polon.* **B38** (2007) 3731–3794, `arXiv:0712.3443`.

[60] Z. Citron et al., "Future physics opportunities for high-density QCD at the LHC with heavy-ion and proton beams", in *HL/HE-LHC Workshop: Workshop on the Physics of HL-LHC, and Perspectives at HE-LHC Geneva, Switzerland, June 18-20, 2018.* 2018. `arXiv:1812.06772`.

[61] ALEPH Collaboration, "Performance of the ALEPH detector at LEP", *Nucl. Instrum. Meth.* **A360** (1995) 481–506, `doi:10.1016/0168-9002(95)00138-7`.

[62] T. Adye, "The lep machine", 2002. `http://hepunx.rl.ac.uk/~adye/thesis/html/node9.html`.

[63] S. Myers and E. Picasso, "The Design, construction and commissioning of the CERN Large Electron Positron collider", *Contemp. Phys.* **31** (1990) 387–403, `doi:10.1080/00107519008213789`.

[64] H. Videau, "The aleph pictorial electromagnetic calorimeter - a high granularity gaseous calorimeter operated in a high magnetic field", *Nuclear Instruments and Methods in Physics Research* **225** (1984), no. 3, 481 – 492, `doi:https://doi.org/10.1016/0167-5087(84)90090-5`.

[65] G. Bagliesi et al., "The Combined Response of the Aleph Electromagnetic and Hadronic Calorimeter to Pions", *Nucl. Instrum. Meth.* **A286** (1990) 61, `doi:10.1016/0168-9002(90)90207-M`.

[66] J. Yeomans, "Archiving of particle physics data and results for long-term access and use", pp. 1201–1204. `arXiv:https://www.worldscientific.com/doi/pdf/10.1142/9789812790873_0260`. `doi:10.1142/9789812790873_0260`.

[67] A. Buckley et al., "HepData and JetWeb: HEP data archiving and model validation", in *15th International Conference on Computing in High Energy and Nuclear Physics (CHEP 2006) Mumbai, Maharashtra, India, February 13-17, 2006*. 2006. `arXiv:hep-ph/0605048`.

[68] R. Kaselis et al., "CMS data transfer operations after the first years of LHC collisions", *Journal of Physics: Conference Series* **396** (dec, 2012) 042033, `doi:10.1088/1742-6596/396/4/042033`.

[69] J. Leduc et al., "Data Center Environmental Sensor for safeguarding the CERN data archive", *J. Phys. Conf. Ser.* **898** (2017), no. 6, 062053, `doi:10.1088/1742-6596/898/6/062053`.

[70] J. Kile and J. von Wimmersperg-Toeller, "Simulation of $e^+e^- \rightarrow$ Hadrons and Comparison to ALEPH Data at Full Detector Simulation with an Emphasis on Four-Jet States", `arXiv:1706.02269`.

[71] J. Kile and J. von Wimmersperg-Toeller, "Localized 4σ and 5σ Dijet Mass Excesses in ALEPH LEP2 Four-Jet Events", *JHEP* **10** (2018) 116, `doi:10.1007/JHEP10(2018)116`, `arXiv:1706.02255`.

[72] A. Heister, "Observation of an excess at 30 GeV in the opposite sign di-muon spectra of Z $\rightarrow b\bar{b} + $ X events recorded by the ALEPH experiment at LEP", `arXiv:1610.06536`.

140

[73] G. Marchesini et al., "HERWIG: A Monte Carlo event generator for simulating hadron emission reactions with interfering gluons. Version 5.1 - April 1991", *Comput. Phys. Commun.* **67** (1992) 465–508, `doi:10.1016/0010-4655(92)90055-4`.

[74] M. Bahr et al., "Herwig++ Physics and Manual", *Eur. Phys. J.* **C58** (2008) 639–707, `doi:10.1140/epjc/s10052-008-0798-9`, `arXiv:0803.0883`.

[75] M. A. Shifman, A. I. Vainshtein, and V. I. Zakharov, "QCD and Resonance Physics. Theoretical Foundations", *Nucl. Phys.* **B147** (1979) 385–447, `doi:10.1016/0550-3213(79)90022-1`.

[76] J. Gasser and H. Leutwyler, "Chiral Perturbation Theory to One Loop", *Annals Phys.* **158** (1984) 142, `doi:10.1016/0003-4916(84)90242-2`.

[77] J. Gasser and H. Leutwyler, "Chiral Perturbation Theory: Expansions in the Mass of the Strange Quark", *Nucl. Phys.* **B250** (1985) 465–516, `doi:10.1016/0550-3213(85)90492-4`.

[78] Y. L. Dokshitzer, "Calculation of the Structure Functions for Deep Inelastic Scattering and e+ e- Annihilation by Perturbation Theory in Quantum Chromodynamics.", *Sov. Phys. JETP* **46** (1977) 641–653. [Zh. Eksp. Teor. Fiz.73,1216(1977)].

[79] M. A. Shifman, A. I. Vainshtein, and V. I. Zakharov, "QCD and Resonance Physics: Applications", *Nucl. Phys.* **B147** (1979) 448–518, `doi:10.1016/0550-3213(79)90023-3`.

[80] T. Sjostrand, S. Mrenna, and P. Z. Skands, "PYTHIA 6.4 Physics and Manual", *JHEP* **05** (2006) 026, `doi:10.1088/1126-6708/2006/05/026`, `arXiv:hep-ph/0603175`.

[81] T. Sjostrand, S. Mrenna, and P. Z. Skands, "A Brief Introduction to PYTHIA 8.1", *Comput. Phys. Commun.* **178** (2008) 852–867, `doi:10.1016/j.cpc.2008.01.036`, `arXiv:0710.3820`.

[82] T. Sjãűstrand et al., "An Introduction to PYTHIA 8.2", *Comput. Phys. Commun.* **191** (2015) 159–177, `doi:10.1016/j.cpc.2015.01.024`, `arXiv:1410.3012`.

[83] J. R. Ellis, M. K. Gaillard, and G. G. Ross, "Search for Gluons in e+ e- Annihilation", *Nucl. Phys.* **B111** (1976) 253, `doi:10.1016/0550-3213(76)90542-3,10.1016/0550-3213(77)90253-X`. [Erratum: Nucl. Phys.B130,516(1977)].

[84] E. Farhi, "A QCD Test for Jets", *Phys. Rev. Lett.* **39** (1977) 1587–1588, `doi:10.1103/PhysRevLett.39.1587`.

141

[85] H. Georgi and M. Machacek, "A Simple QCD Prediction of Jet Structure in e+ e- Annihilation", *Phys. Rev. Lett.* **39** (1977) 1237, `doi:10.1103/PhysRevLett.39.1237`.

[86] G. C. Fox and S. Wolfram, "Observables for the Analysis of Event Shapes in e+ e- Annihilation and Other Processes", *Phys. Rev. Lett.* **41** (1978) 1581, `doi:10.1103/PhysRevLett.41.1581`.

[87] G. C. Fox and S. Wolfram, "Event Shapes in e+ e- Annihilation", *Nucl. Phys.* **B149** (1979) 413, `doi:10.1016/0550-3213(79)90120-2,10.1016/0550-3213(79)90003-8`. [Erratum: Nucl. Phys.B157,543(1979)].

[88] C. L. Basham, L. S. Brown, S. D. Ellis, and S. T. Love, "Energy Correlations in electron - Positron Annihilation: Testing QCD", *Phys. Rev. Lett.* **41** (1978) 1585, `doi:10.1103/PhysRevLett.41.1585`.

[89] S. Catani, F. Krauss, R. Kuhn, and B. R. Webber, "QCD matrix elements + parton showers", *JHEP* **11** (2001) 063, `doi:10.1088/1126-6708/2001/11/063`, `arXiv:hep-ph/0109231`.

[90] D. P. Barber et al., "Discovery of Three Jet Events and a Test of Quantum Chromodynamics at PETRA Energies", *Phys. Rev. Lett.* **43** (1979) 830, `doi:10.1103/PhysRevLett.43.830`.

[91] CDF Collaboration, "The Topology of three jet events in $\bar{p}p$ collisions at $\sqrt{s} = 1.8$ TeV", *Phys. Rev.* **D45** (1992) 1448–1458, `doi:10.1103/PhysRevD.45.1448`.

[92] S. Catani, L. Trentadue, G. Turnock, and B. R. Webber, "Resummation of large logarithms in e+ e- event shape distributions", *Nucl. Phys.* **B407** (1993) 3–42, `doi:10.1016/0550-3213(93)90271-P`.

[93] P. Hoyer et al., "Quantum Chromodynamics and Jets in e+ e-", *Nucl. Phys.* **B161** (1979) 349–372, `doi:10.1016/0550-3213(79)90217-7`.

[94] A. De Rujula, J. R. Ellis, E. G. Floratos, and M. K. Gaillard, "QCD Predictions for Hadronic Final States in e+ e- Annihilation", *Nucl. Phys.* **B138** (1978) 387–429, `doi:10.1016/0550-3213(78)90388-7`.

[95] S. Frixione, "A General approach to jet cross-sections in QCD", *Nucl. Phys.* **B507** (1997) 295–314, `doi:10.1016/S0550-3213(97)00574-9`, `arXiv:hep-ph/9706545`.

[96] M. Cacciari, G. P. Salam, and G. Soyez, "The anti-k_t jet clustering algorithm", *JHEP* **04** (2008) 063, `doi:10.1088/1126-6708/2008/04/063`, `arXiv:0802.1189`.

[97] T. Sjostrand and M. Bengtsson, "The Lund Monte Carlo for Jet Fragmentation and e+ e- Physics. Jetset Version 6.3: An Update", *Comput. Phys. Commun.* **43** (1987) 367, `doi:10.1016/0010-4655(87)90054-3`.

[98] M. Cacciari and G. P. Salam, "Dispelling the N^3 myth for the k_t jet-finder", *Phys. Lett.* **B641** (2006) 57–61, `doi:10.1016/j.physletb.2006.08.037`, `arXiv:hep-ph/0512210`.

[99] S. Catani, Y. L. Dokshitzer, M. H. Seymour, and B. R. Webber, "Longitudinally invariant K_t clustering algorithms for hadron hadron collisions", *Nucl. Phys.* **B406** (1993) 187–224, `doi:10.1016/0550-3213(93)90166-M`.

[100] S. Catani et al., "New clustering algorithm for multi - jet cross-sections in e+ e- annihilation", *Phys. Lett.* **B269** (1991) 432–438, `doi:10.1016/0370-2693(91)90196-W`.

[101] B. R. Webber, "Hadronization", in *Proceedings: Summer School on Hadronic Aspects of Collider Physics, Zuoz, Switzerland, Aug 23-31, 1994*, pp. 49–77. 1994. `arXiv:hep-ph/9411384`.

[102] D. J. Miller and M. H. Seymour, "Secondary heavy quark pair production in e+ e- annihilation", *Phys. Lett.* **B435** (1998) 213–220, `doi:10.1016/S0370-2693(98)00773-4`, `arXiv:hep-ph/9805414`.

[103] D. J. Miller and M. H. Seymour, "The Jet multiplicity as a function of thrust", *Phys. Lett.* **B435** (1998) 199–212, `doi:10.1016/S0370-2693(98)00774-6`, `arXiv:hep-ph/9805413`.

[104] C. L. Basham, L. S. Brown, S. D. Ellis, and S. T. Love, "Energy Correlations in electron-Positron Annihilation in Quantum Chromodynamics: Asymptotically Free Perturbation Theory", *Phys. Rev.* **D19** (1979) 2018, `doi:10.1103/PhysRevD.19.2018`.

[105] Y. L. Dokshitzer and B. R. Webber, "Calculation of power corrections to hadronic event shapes", *Phys. Lett.* **B352** (1995) 451–455, `doi:10.1016/0370-2693(95)00548-Y`, `arXiv:hep-ph/9504219`.

[106] Y. L. Dokshitzer and B. R. Webber, "Power corrections to event shape distributions", *Phys. Lett.* **B404** (1997) 321–327, `doi:10.1016/S0370-2693(97)00573-X`, `arXiv:hep-ph/9704298`.

[107] G. P. Korchemsky and G. F. Sterman, "Power corrections to event shapes and factorization", *Nucl. Phys.* **B555** (1999) 335–351, `doi:10.1016/S0550-3213(99)00308-9`, `arXiv:hep-ph/9902341`.

[108] ALEPH Collaboration, "Studies of quantum chromodynamics with the ALEPH detector", *Phys. Rept.* **294** (1998) 1–165, `doi:10.1016/S0370-1573(97)00045-8`.

[109] ALEPH Collaboration, "Studies of QCD at e+ e- centre-of-mass energies between 91-GeV and 209-GeV", *Eur. Phys. J.* **C35** (2004) 457–486, `doi:10.1140/epjc/s2004-01891-4`.

[110] B. Alver and G. Roland, "Collision-geometry fluctuations and triangular flow in heavy-ion collisions", *Phys. Rev. C* **81** (May, 2010) 054905, `doi:10.1103/PhysRevC.81.054905`.

[111] CMS Collaboration, "Observation of long-range near-side angular correlations in proton-lead collisions at the LHC", *Phys. Lett.* **B718** (2013) 795–814, `doi:10.1016/j.physletb.2012.11.025`, `arXiv:1210.5482`.

[112] B. Efron, "Bootstrap methods: Another look at the jackknife", *Ann. Statist.* **7** (01, 1979) 1–26, `doi:10.1214/aos/1176344552`.

[113] T. A. Trainor, "Zero yield at minimum (zyam) method and v_2: Underestimating jet yields from dihadron azimuth correlations", *Phys. Rev. C* **81** (Jan, 2010) 014905, `doi:10.1103/PhysRevC.81.014905`.

[114] CMS Collaboration, "Observation of Long-Range Near-Side Angular Correlations in Proton-Proton Collisions at the LHC", *JHEP* **09** (2010) 091, `doi:10.1007/JHEP09(2010)091`, `arXiv:1009.4122`.

[115] ATLAS Collaboration, "Observation of Long-Range Elliptic Azimuthal Anisotropies in $\sqrt{s} =$13 and 2.76 TeV pp Collisions with the ATLAS Detector", *Phys. Rev. Lett.* **116** (2016), no. 17, 172301, `doi:10.1103/PhysRevLett.116.172301`, `arXiv:1509.04776`.

[116] ALICE Collaboration, "Long-range angular correlations on the near and away side in p-Pb collisions at $\sqrt{s_{NN}} = 5.02$ TeV", *Phys. Lett.* **B719** (2013) 29–41, `doi:10.1016/j.physletb.2013.01.012`, `arXiv:1212.2001`.

[117] ATLAS Collaboration, "Observation of Associated Near-Side and Away-Side Long-Range Correlations in $\sqrt{s_{NN}}=$5.02??TeV Proton-Lead Collisions with the ATLAS Detector", *Phys. Rev. Lett.* **110** (2013), no. 18, 182302, `doi:10.1103/PhysRevLett.110.182302`, `arXiv:1212.5198`.

[118] PHENIX Collaboration, "Quadrupole Anisotropy in Dihadron Azimuthal Correlations in Central d+Au Collisions at $\sqrt{s_{NN}}=$200 GeV", *Phys. Rev. Lett.* **111** (2013), no. 21, 212301, `doi:10.1103/PhysRevLett.111.212301`, `arXiv:1303.1794`.

[119] CMS Collaboration, "Centrality dependence of dihadron correlations and azimuthal anisotropy harmonics in PbPb collisions at $\sqrt{s_{NN}} = 2.76$ TeV", *Eur. Phys. J.* **C72** (2012) 2012, `doi:10.1140/epjc/s10052-012-2012-3`, `arXiv:1201.3158`.

[120] J.-Y. Ollitrault, "Anisotropy as a signature of transverse collective flow", *Phys. Rev.* **D46** (1992) 229–245, `doi:10.1103/PhysRevD.46.229`.

[121] B. Alver and G. Roland, "Collision geometry fluctuations and triangular flow in heavy-ion collisions", *Phys. Rev.* **C81** (2010) 054905, `doi:10.1103/PhysRevC.82.039903,10.1103/PhysRevC.81.054905`, `arXiv:1003.0194`. [Erratum: Phys. Rev.C82,039903(2010)].

[122] K. Dusling, W. Li, and B. Schenke, "Novel collective phenomena in high-energy proton?proton and proton?nucleus collisions", *Int. J. Mod. Phys.* **E25** (2016), no. 01, 1630002, `doi:10.1142/S0218301316300022`, `arXiv:1509.07939`.

[123] J. L. Nagle and W. A. Zajc, "Small System Collectivity in Relativistic Hadronic and Nuclear Collisions", *Ann. Rev. Nucl. Part. Sci.* **68** (2018) 211–235, `doi:10.1146/annurev-nucl-101916-123209`, `arXiv:1801.03477`.

[124] K. Dusling and R. Venugopalan, "Comparison of the color glass condensate to dihadron correlations in proton-proton and proton-nucleus collisions", *Phys. Rev.* **D87** (2013), no. 9, 094034, `doi:10.1103/PhysRevD.87.094034`, `arXiv:1302.7018`.

[125] L. He et al., "Anisotropic parton escape is the dominant source of azimuthal anisotropy in transport models", *Phys. Lett.* **B753** (2016) 506–510, `doi:10.1016/j.physletb.2015.12.051`, `arXiv:1502.05572`.

[126] P. Bozek, "Collective flow in p-Pb and d-Pd collisions at TeV energies", *Phys. Rev.* **C85** (2012) 014911, `doi:10.1103/PhysRevC.85.014911`, `arXiv:1112.0915`.

[127] J. L. Nagle et al., "Minimal conditions for collectivity in e^+e^- and $p+p$ collisions", *Phys. Rev.* **C97** (2018), no. 2, 024909, `doi:10.1103/PhysRevC.97.024909`, `arXiv:1707.02307`.

[128] ALEPH Collaboration, "ALEPH: A detector for electron-positron annnihilations at LEP", *Nucl. Instrum. Meth.* **A294** (1990) 121–178, `doi:10.1016/0168-9002(90)91831-U`. [Erratum: Nucl. Instrum. Meth.A303,393(1991)].

[129] A. Tripathee et al., "Jet Substructure Studies with CMS Open Data", *Phys. Rev.* **D96** (2017), no. 7, 074003, `doi:10.1103/PhysRevD.96.074003`, `arXiv:1704.05842`.

[130] T. Sjostrand et al., "High-energy physics event generation with PYTHIA 6.1", *Comput. Phys. Commun.* **135** (2001) 238–259, `doi:10.1016/S0010-4655(00)00236-8`, `arXiv:hep-ph/0010017`.

[131] N. N. Ajitanand et al., "Decomposition of harmonic and jet contributions to particle-pair correlations at ultra-relativistic energies", *Phys. Rev.* **C72** (2005) 011902, `doi:10.1103/PhysRevC.72.011902`, `arXiv:nucl-ex/0501025`.

[132] Y. L. Dokshitzer, G. D. Leder, S. Moretti, and B. R. Webber, "Better jet clustering algorithms", *JHEP* **08** (1997) 001, `doi:10.1088/1126-6708/1997/08/001`, `arXiv:hep-ph/9707323`.